

Phase separation and structure formation in gadolinium based liquid and glassy metallic alloys

**Von der Fakultät Maschinenwesen der Technischen Universität Dresden
zur Erlangung des akademischen Grades
Doktoringenieur (Dr.-Ing.)
angenommene**

DISSERTATION

**von
Junhee Han
geboren am 23. 05. 1981
in Busan, Republik Korea (Südkorea)**

1. Gutachter: Prof. Dr. Jürgen Eckert (TU Dresden)

2. Gutachter: Prof. Dr. Do-Hyang Kim (Yonsei University)

Tag der Einreichung: 22. 11. 2013

Tag der Verteidigung: 14. 04. 2014

Abstract

In this PhD research the liquid-liquid phase separation phenomena in Gd-based alloys was investigated in terms of phase equilibria, microstructure formation upon quenching the melt and corresponding magnetic properties of phase-separated metallic glasses. The phase diagrams of the binary subsystems Gd-Zr and Gd-Ti were experimentally reassessed. Especially the phase equilibria with the liquid phase could be determined directly by combining *in situ* high energy synchrotron X-ray diffraction with electrostatic levitation of the melt. The Gd-Zr system is of eutectic type with a metastable miscibility gap. The eutectic composition at 18 ± 2 at.% Zr, the liquidus line and the coexistence of *bcc*-Zr and *bcc*-Gd at elevated temperature could be determined. The Gd-Ti system is a monotectic system. The experimental observations in this work led to improved new Gd-Zr and Gd-Ti phase diagrams.

The phase equilibria of the ternary Gd-Ti-Co system were analyzed for two alloy compositions. The XRD patterns for molten $\text{Gd}_{35}\text{Ti}_{35}\text{Co}_{30}$ gave direct evidence for the coexistence of two liquid phases formed by liquid-liquid phase separation. The first experimental and thermodynamic assessment of the ternary Gd-Ti-Co system revealed that the stable miscibility gap of binary Gd-Ti extends into the ternary Gd-Ti-Co system (up to about 30 at.% Co).

New phase-separated metallic glasses were synthesized in Gd-TM-Co-Al (TM = Hf, Ti or Zr) alloys. The microstructure was characterized in terms of composition and cooling rate dependence of phase separation. Due to large positive enthalpy of mixing between Gd on the one side and Hf, Ti or Zr on the other side, the alloys undergo liquid-liquid phase separation during rapid quenching the melt. The parameters determining the microstructure development during phase separation are the thermodynamic properties of the liquid phase, kinetic parameters and quenching conditions. By controlling these parameters and conditions the microstructure can be tailored both at microscopic and macroscopic length scales. This includes either droplet-like or interconnected microstructures at the microscopic level and glass-glass or glass-crystalline composites at the macroscopic level.

Essential parameter for the quenched in microstructure is the temperature dependence of liquid-liquid phase separation, which is determined by the chemical

composition of the alloy: on the one hand, earlier and/or later stages of spinodal decomposition or almost homogeneous glassy states are obtained if the critical temperature of miscibility gap T_c is close to the glass transition temperature T_g ; and on the one hand, coarsening and secondary precipitations of the liquids are obtained if T_c is much higher than T_g . Finally, the influence of the microstructure developed by phase separation on their magnetic properties had been investigated. The saturation magnetization σ_s depends on the overall amount of Gd atoms in the alloys and is not remarkably affected by phase separation processes. The Curie temperature T_{Curie} of the magnetic transition is influenced by the changed chemical composition of the Gd-rich glassy phases compared to that of monolithic Gd-Co-Al glasses.

Zusammenfassung

In dieser Doktorarbeit wurde die flüssig-flüssig Phasentmischung von Gd-basierten Legierungen hinsichtlich der Phasengleichgewichte, der Gefügeentwicklung während der Schmelzabschreckung und dazugehöriger magnetischer Eigenschaften, untersucht.

Die Zustandsdiagramme der binären Untersysteme Gd-Zr und Gd-Ti wurden experimentell ermittelt. Insbesondere konnten die Phasengleichgewichte mit der flüssigen Phase mittels *in-situ* Röntgenbeugungsmessungen an elektrostatisch levitierten Schmelzen direkt, bestimmt werden. Das Gd-Zr System stellt ein eutektisches Phasendiagramm dar und besitzt eine metastabile Mischungslücke. Die eutektische Zusammensetzung wurde mit 18 ± 2 at.% Zr bestimmt und der Verlauf der Liquiduslinie bei erhöhten Temperaturen wurde experimentell ermittelt. Experimentell wurde die Koexistenz von kubisch-raumzentrierten Zr und Gd in einem Bereich bei hohen Temperaturen nachgewiesen. Das Gd-Ti-System ist von monotektischer Art. Die experimentellen Beobachtungen dieser Arbeit trugen wesentlich zur Verbesserung der Beschreibung der Phasendiagramme Gd-Zr- und Gd-Ti-Phasen bei.

Die Phasengleichgewichte des ternären Gd-Ti-Co-Systems wurde anhand zweier Legierungszusammensetzungen untersucht. Die Röntgenbeugungsdiffraktogramme der geschmolzenen Legierung $Gd_{35}Ti_{35}Co_{30}$ sind ein direkter Beleg für die Koexistenz zweier flüssiger Phasen, aufgrund der flüssig-flüssig Phasentmischung. Die erste experimentelle und thermodynamische Auswertung des ternären Gd-Ti-Co-Systems zeigt, dass sich die stabile Mischungslücke des binären Gd-Ti-Systems ins ternäre Gd-Ti-Co-System bis zu ungefähr 30 at.% Co erstreckt.

Es wurden neue Gd-TM-Co-Al (TM = Hf, Ti oder Zr)-basierte metallische Gläser, die separierte Phasen besitzen, hergestellt. Ihr Gefüge wurden hinsichtlich Zusammensetzung- und Abkühlratenabhängigkeit der Phasentmischung charakterisiert. Aufgrund der großen positiven Mischungsenthalpie zwischen Gd auf der einen und Hf, Ti oder Zr auf der anderen Seite, weisen diese Legierungen eine flüssig-flüssig Phasentmischung während der Abschreckung aus der Schmelze auf. Die Einflussgrößen, die die Gefügeentwicklung während der Phasentmischung bestimmen, sind die thermodynamischen Eigenschaften der flüssigen Phase, die kinetische Parameter und die

Abschreckbedingungen. Indem diese Parameter und Bedingungen kontrolliert werden, kann das Gefüge auf makro- sowie mikroskopischer Längenskala maßgeschneidert werden. Dies beinhaltet entweder tropfenförmige oder miteinander verbundene Gefüge auf einer mikroskopischen Skala und Glas-Glas oder Glas-Kristall Komposite auf einer makroskopischen Längenskala.

Ein wesentlicher Parameter für das abgeschreckte Gefüge ist die Temperatur-Abhängigkeit der flüssig-flüssig Phasentrennung, die durch die chemische Zusammensetzung der Legierung bestimmt wird. Frühere und/oder spätere Stadien der spinodalen Entmischung oder nahezu homogene amorphe Zustände können abhängig von dem Temperaturunterschied zwischen kritischer Temperatur der flüssig-flüssig Phasentrennung und der Glasübergangstemperatur erhalten werden. Wenn die kritische Temperatur der Mischungslücke, T_c , viel höher ist als die des Glasübergangs, T_g , können makroskopische Vergrößerungen der tropfenförmigen Verteilung der flüssigen Phase und sekundäre flüssige oder kristalline Ausscheidungen in den gebildeten amorphen Phasen erhalten werden.

Durch die Phasentrennung und die erhaltenen heterogenen Gefüge werden die magnetischen Eigenschaften beeinflusst. Die Sättigungsmagnetisierung, σ_s , hängt von der gesamten Anzahl der Gd-Atome der Legierung ab und wird nicht bemerkenswert vom Phasentrennungsprozess beeinflusst. Die Curie Temperatur T_{Curie} wird im Vergleich zu monolithischen Gd-Co-Al Gläsern, und abhängig von der chemischen Zusammensetzung der Gd-reichen Phase, verändert.

Contents

Abstract	iii
Contents	vii
Chapter 1: Introduction	1
Chapter 2: Fundamentals	4
2.1 Thermodynamics of alloys	4
2.1.1 Phase equilibria and phase diagram	4
2.1.2 Thermodynamic basis of liquid-liquid phase separation	5
2.2 Metallic glass	8
2.2.1 Concept of metallic glass	8
2.2.2 Glass formation in metallic alloys	9
2.3 Phase separation in metallic glasses	14
Chapter 3: Experimental methods	17
3.1 Alloy preparation	17
3.2 Analysis techniques	19
3.2.1 Chemical analysis	19
3.2.2 Thermal analysis	19
3.2.3 X-ray diffractions	20
3.2.4 Electron microscopy	24
3.2.5 Atom probe tomography	24
3.3 Magnetic measurements	26
Chapter 4: Experimental results	27
4.1 Experimental assessment of Gd-Zr, Gd-Ti and Gd-Ti-Co phase diagrams	27
4.1.1 The binary Gd-Zr system	27
4.1.1.1 <i>In situ</i> observation of phase equilibria at elevated temperatures	28
4.1.1.2 Microstructure of as-solidified Gd-Zr alloys	36
4.1.2 The binary Gd-Ti system	37
4.1.2.1 <i>In situ</i> observation of phase equilibria at elevated temperatures	38
4.1.2.3 Microstructure of as-solidified Gd-Ti alloys	46
4.1.3. The ternary Gd-Ti-Co system	49

4.1.3.1 <i>In situ</i> observation of phase equilibria at elevated temperatures.....	50
4.1.3.2 Microstructure of as-solidified Gd-Ti-Co alloys.....	54
4.2 Structure formation and phase separation in Gd-based metallic glasses.....	59
4.2.1 Phase separation in Gd-Hf-Co-Al alloys.....	59
4.2.1.1 Phase formation and thermal stability.....	60
4.2.1.2 Microstructure investigation.....	62
4.2.2 Phase separation in Gd-Ti-Co-Al alloy.....	66
4.2.3 Phase separation in Zr-Gd-Co-Al alloys.....	68
4.2.3.1 Characterization of the as-quenched states.....	68
4.2.3.2 <i>In situ</i> SAXS/WAXS investigation.....	75
4.3 Magnetic properties of phase separated metallic glasses.....	79
4.3.1 Magnetic properties of Gd-Hf-Co-Al alloys.....	79
4.3.2 Magnetic properties of Gd-Ti-Co-Al alloys.....	83
Chapter 5: Discussion of structure formation.....	85
Chapter 6: Summary and outlook.....	97
Chapter 7: Appendix.....	100
Acknowledgement.....	104
Bibliography.....	106
Publications.....	119

Chapter 1: Introduction

In material science, according to the Ehrenfest classification, *phase separation* is a first-order phase transformation involving the process in which one homogeneous phase (liquid or glass) is separated into two different amorphous phases [1]. The term “phase separation” may be unfamiliar to the common men. Nevertheless, this phenomenon is well-known and commonly observed in our daily life. An immiscible liquids that are incapable of being mixed to form a homogeneous substance, water and oil, could be the most representative example. The subject of “*phase separation*” is of great scientific significance in the wide field of material science. It has indeed been investigated extensively for oxide-glasses and polymers [2,3,4,5].

For metallic alloy systems just recently, a new type of phase-separated metallic glasses that exhibit glass-glass structure in the as-quenched state, have been prepared by rapid quenching of the melt. It has been first reported for a quinary alloy La-Zr-Cu-Ni-Al system by Kündig *et al.* [6]. In this alloy the occurrence of phase separation was revealed by a differential scanning calorimetry (DSC) trace that exhibits two thermal events corresponding to La-rich glass and Zr-rich glass phases. In addition, the microstructure investigation also confirmed the presence of the two glassy phases [6]. This work by Kündig *et al.* is perhaps very significant as the first direct evidence for liquid-liquid phase separation in a metallic glass during cooling from the liquid state. Since this first founding, Park *et al.* and Mattern *et al.* also reported this interesting behavior for a quaternary Y-Ti-Al-Co system [7] and a ternary Ni-Nb-Y system [8] in succession. In these alloys, liquid-liquid phase separation takes place already in the melt prior to crystallization during the rapid quenching. The origin of the strong demixing tendency that drives phase separation into two liquid phases, is due to the positive enthalpy of mixing between the constituents in the liquid state, i.e. La-Zr ($\Delta H_{\text{mix}}^{\text{La-Zr}} = + 13 \text{ kJ mol}^{-1}$), Y-Ti ($\Delta H_{\text{mix}}^{\text{Y-Ti}} = + 15 \text{ kJ mol}^{-1}$) and Nb-Y ($\Delta H_{\text{mix}}^{\text{Nb-Y}} = + 30 \text{ kJ mol}^{-1}$) for instance [9,10]. Afterwards, it has been shown that the mechanical property of metallic glasses could also be enhanced by introducing a chemical and/or microstructural heterogeneity via such phase separation.

Generally, to develop new alloys for phase-separated metallic glasses, two main prerequisites must be satisfied. Firstly, the alloy system should exhibit high glass-forming

ability (GFA) which requires a strong negative enthalpy of mixing between the constituents. Secondly, an element has to have strong demixing tendency with at least one of the main constituents of the alloy, given by positive enthalpy of mixing [6]. For this reason, the development of a phase-separated metallic glass faces an apparent paradox with the glass forming ability. Nevertheless, phase separation in metallic glasses has attracted researchers not only because it provides an opportunity to synthesize different types of composites, for instance, glass-glass or glass-crystals, which influences the properties of materials [11,12,13,14], but also it is of scientific interest to be able to investigate the decomposition behavior of glass [15,16,17,18,19]. Regardless of whether phase separation takes place via nucleation and growth or via spinodal decomposition, from the practical point of view the microstructure of all these alloys virtually corresponds to that of the later stage in which coarsened and hierarchical.

The broad scope of this thesis work was to investigate the microstructure formation and possible phase separation in Gd-TM (TM is transition metal) multi-component systems upon rapid quenching the melt. The main objectives of this PhD study were:

1. To prepare new Gd-containing phase-separated metallic glasses
2. To experimentally investigate the efficacy of adding alloying elements with positive enthalpy of mixing on phase separation in Gd-based metallic glasses.
3. To contribute to fundamental understanding of structure formation and phase separation in the liquid upon quenching
4. To analyze the influence of phase separation on magnetic properties of Gd-based phase-separated glasses

For the study of liquid-liquid phase separation in this work, the following alloy systems were chosen:

1. Gd-Hf-Co-Al ($\Delta H_{\text{mix}}^{\text{Gd-Hf}} = + 11 \text{ kJ mol}^{-1}$)
2. Gd-Ti-Co-Al ($\Delta H_{\text{mix}}^{\text{Gd-Ti}} = + 15 \text{ kJ mol}^{-1}$)
3. Gd-Zr-Co-Al ($\Delta H_{\text{mix}}^{\text{Gd-Zr}} = + 9 \text{ kJ mol}^{-1}$)

Based on the bulk glass forming ternary Gd-Co-Al [20] and Zr-Co-Al [21,22] alloys, the additions of different element are characterized by different values of enthalpy of mixing which were expected to result in different microstructures.

The understanding of microstructure formation of such multi-component systems requires the knowledge of thermodynamic information, which is unknown so far for the alloy systems under investigation. In this context, a systematic investigation of phase diagrams and especially the miscibility gap is required in order to obtain a deeper understanding on how phase separation develops during solidification of such alloys. Therefore, phase diagrams of the binary Gd-Zr and Gd-Ti systems and the ternary Gd-Ti-Co system are experimentally as well as thermodynamically assessed in order to bridge the gap between simple alloy systems with a miscibility gap and the phase-separated metallic glasses.

This PhD dissertation consists of 6 chapters. The following chapter (Chapter 2) is an introduction to the theoretical background. This chapter is subdivided into sections dealing with thermodynamics of alloys, metallic glasses and phase separation in metallic alloys in more detail. Chapter 3 details the experimental procedures applied in the present study. The apparatus and conditions used for sample preparation and analysis as well as the experimental setups for *in situ* X-ray diffraction measurements at Deutsches Elektronen-Synchrotron (DESY in Hamburg) are introduced in this chapter. Chapter 4 reports all the experimental results of the investigations done on Gd-based alloy systems; the experimental assessments of phase diagrams of the Gd-based subsystems is presented in chapter 4.1, the structure formation and phase separation in Gd-based metallic glasses obtained by rapid quenching of the melt are described in chapter 4.2 and the magnetic properties of phase-separated Gd-based metallic glasses are given in chapter 4.3. Chapter 5 summarizes the results obtained from the studies in chapter 4 and discusses in a general view of the structure formation of heterogeneous metallic glasses via liquid-liquid phase separation upon quenching the melt. Finally, the summary and the outlook for this study are presented in chapter 6. The references cited in this dissertation are listed at the end.

Chapter 2: Fundamentals

2.1 Thermodynamics of alloys

2.1.1 Phase equilibria and phase diagram

From the thermodynamic point of view, the stability of a system at a given temperature and pressure is determined by its Gibbs free energy G ,

$$G = H - TS, \quad (2.1)$$

Where H is the enthalpy T is the absolute temperature and S is the entropy. A system is stable and in equilibrium when the lowest value (minimum) of G is attained. A phase diagram is a graphical description of the thermodynamic variables when equilibrium is achieved among the phases of a system, that is, a phase diagram provide a map of equilibrium phases as a function of temperature (at atmospheric pressure). The equilibrium phase diagram is obtained from the common tangent construction applied to the Gibbs free energy curves of the various phases that may be present in the system. Understanding of thermodynamic and thermophysical properties is of high practical importance in the description of phase transformations and alloy design. As already stated in large number of material science textbooks, there are various types of phase transformation and phase diagrams (Fig. 2.1). Among them, the most important phenomena within the scope of this work, is the liquid-liquid phase separation $L \rightarrow L_1 + L_2$ in binary and multi-component alloy systems. For an alloy system to achieve the liquid-liquid phase separation, the system must exhibit a certain region of temperature and composition, where the system exists in equilibrium as two liquid phases of different chemical composition, and this region is determined by the thermodynamic variable *enthalpy of mixing* ΔH_{mix} and referred to as *miscibility gap*. Since the development of solution models and computational methods has permitted a quantitative coupling of thermodynamics and phase diagrams, a massive amount of information about binary alloy phase diagram is now available [23].

Nevertheless, there are still many uncertainties of the experimental data at higher temperatures especially concerning the liquid phase equilibria.

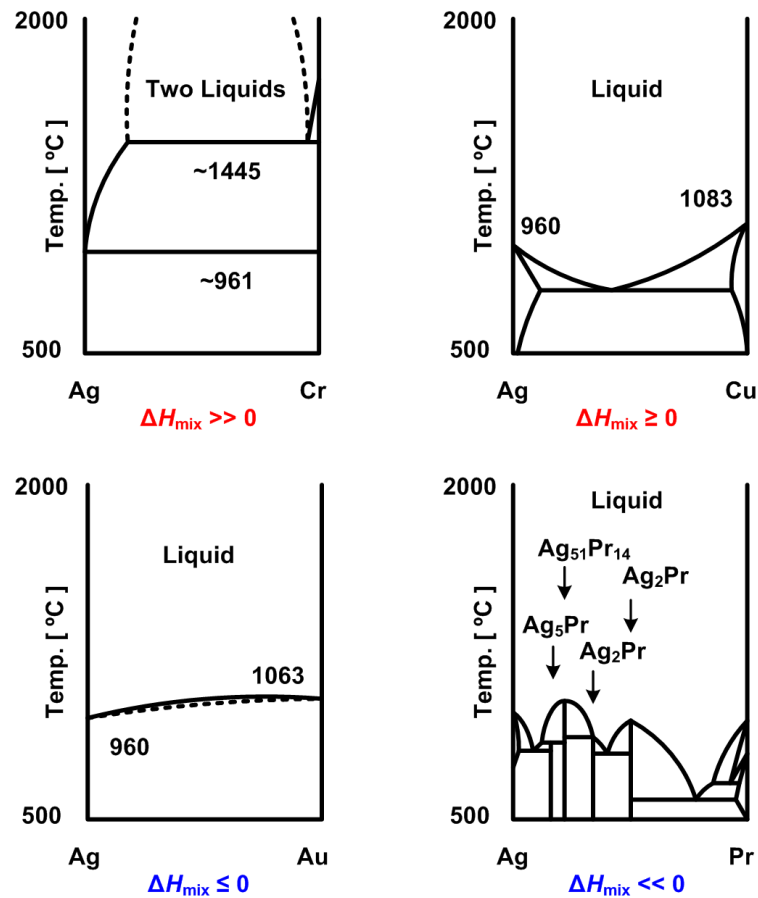


Figure 2.1: Four types of Ag-X (X = Cr, Cu, Au and Pr) binary alloy phase diagrams showing the effect of enthalpy of mixing ΔH_{mix} on topological changes [23].

2.1.2 Thermodynamic basis of liquid-liquid phase separation

As briefly introduced in previous section, a liquid-liquid phase separation takes place when temperature and composition of an alloy melt is in the region of *miscibility gap*. The occurrence of the miscibility gap is characterized by thermodynamics, especially a positive enthalpy of mixing ΔH_{mix} between constituent elements is required as indicated in Fig. 2.1. For each phase in a binary *A-B* alloy system, total free energy of the mixture is defined as:

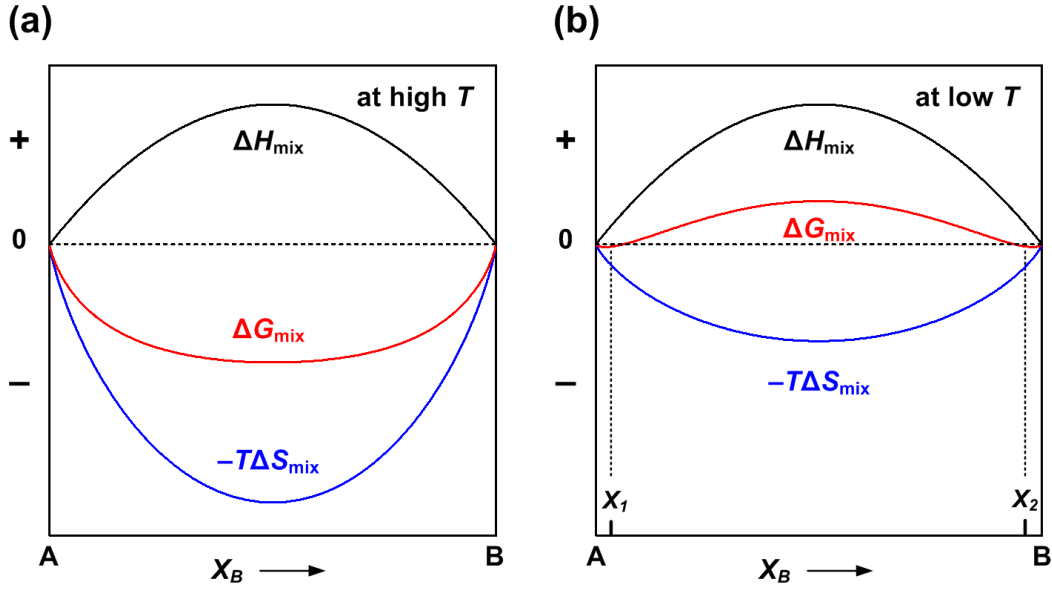


Figure 2.2: Schematic illustration of the effect of a positive enthalpy of mixing ΔH_{mix} and temperature T on the free energy of mixing ΔG_{mix} .

$$G_{A-B} = x_A G_A + x_B G_B + \Delta G_{\text{excess}} \quad (2.2)$$

and

$$\Delta G_{\text{excess}} = \Delta H_{\text{excess}} - T\Delta S_{\text{excess}} \quad (2.3)$$

where ΔG_{excess} is the excess Gibbs free energy caused by the mixing, and ΔH_{excess} and ΔS_{excess} are the excess enthalpy and entropy, respectively. The excess enthalpy is often also referred to as enthalpy of mixing ΔH_{mix} . For some binary alloy systems, values of the ΔH_{mix} are positive ($\Delta H_{\text{mix}} > 0$) due to the bonding energy relationship of the constituent elements [24,25]. Meanwhile, since disorder is always favored, value of entropy is negative ($\Delta S_{\text{mix}} < 0$).

Fig. 2.2 schematically illustrates the effect of the positive enthalpy of mixing ΔH_{mix} and temperature T on the free energy of mixing ΔG_{mix} . When, $\Delta H_{\text{mix}} > 0$, possible situations are temperature dependent. At higher temperatures, $T\Delta S_{\text{mix}}$ is greater than ΔH_{mix} for whole composition range and consequently the ΔG_{mix} exhibits negative values for all compositions (Fig. 2.2a). In this case, a homogeneous liquid phase is then stable i.e. the mixture is miscible. At relatively lower temperatures, on the other hand, $T\Delta S_{\text{mix}}$ becomes

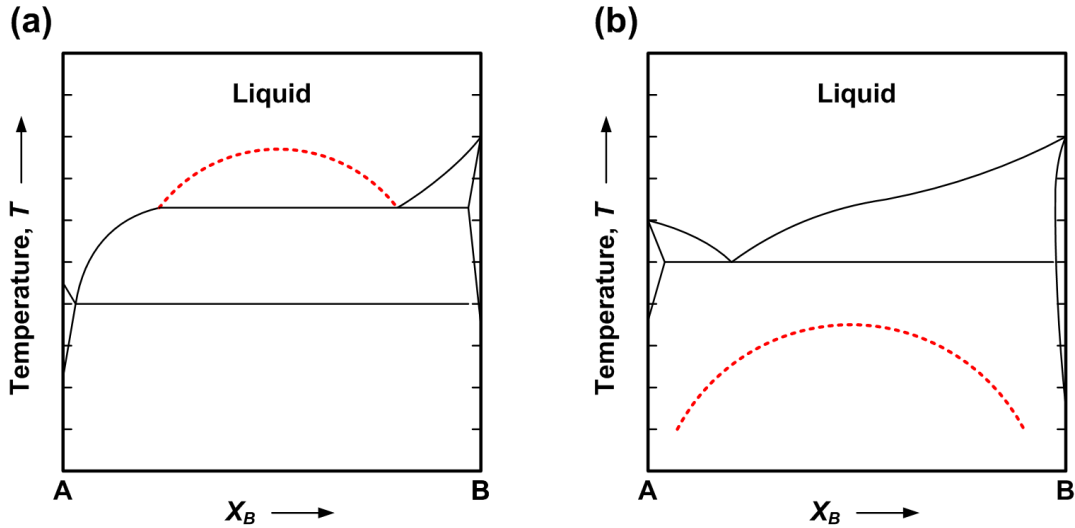


Figure 2.3: Topological changes in the phase diagram for a binary A - B system with a positive enthalpy of mixing ($\Delta H_{\text{mix}} > 0$). The dashed curves (in red color) are (a) *stable miscibility gap* and (b) *metastable miscibility gap*, respectively.

smaller than ΔH_{mix} . Therefore ΔG_{mix} curve develops a hump of negative curvature ($\Delta G_{\text{mix}} > 0$) in the middle of composition range which is accompanied with two minima (Fig. 2.2b). Within the composition range between two minima X_1 and X_2 the homogeneous liquid phase is no longer stable but spontaneously tends separate into two different liquid phases and the two separated liquid phases are then stable at compositions X_1 and X_2 , respectively. Compositions which are not between X_1 and X_2 are still miscible as a single phase mixture. The distance between two maxima i.e. the distance between bitangent points decreases with increasing temperature until a critical temperature $T \approx T_c$ is reached, above which single phase mixture is stable. The temperature dependence of two minima finally maps out miscibility gap in a phase diagram. This miscibility gap where liquid-liquid phase separation to be favored is found in about 10 % (about 300 binary systems) of known binary alloy system [23].

In these binary alloy phase diagrams there are two possible types of miscibility gaps according to the extent of positive deviations in ΔG_{mix} : “*stable miscibility gap*” when the positive deviations are large enough the system exhibits a extended miscibility gap above the liquidus (Fig. 2.3a). And “*metastable miscibility gap*”, on the other hand, when the positive deviations are not large enough that the system exhibits a flattening of the liquidus indicating a tendency for phase separation. In this case, however, a miscibility gap still exists below the liquidus (Fig. 2.3b), and therefore, if a sufficient suppression for

crystallization of the solid phases can be achieved by rapid quenching a melt, then the deeply undercooled liquid may undergo a liquid-liquid phase separation. The free energy change of mixing ΔG_{mix} also subdivides the miscibility gap into regions of instability and metastability.

2.2 Metallic glass

2.2.1 Concept of metallic glass

In general, glass is an inorganic solid material that usually possess transparency or translucency as well as exhibiting hardness and brittleness, and impervious to the natural elements [26]. The most familiar types of glass in our daily life can be a window glasses and housewares which are usually made of silicate and oxides. Although glass is one of most commonly used materials, it still has been poorly understood [27,28,29,30,31]. From the scientific point of view, solid matters with the major bonding types: ionic, covalent, hydrogen, van der Waals, and metallic can be obtained in a non-crystalline solid form by various methods [32]. The methods of producing these materials categorize the broader class of the non-crystalline solid materials into two sub-classes: glass is any non-crystalline solid produced by continuous cooling from the equilibrium liquid state, and amorphous solid is any non-crystalline solid obtained by any other method, for instance, vapor deposition or solid-state processing methods, but not continuous cooling from the liquid state [33].

Generally and traditionally, nature of metals and alloys in solid state is considered as crystalline if they possess a translational symmetry. That is, their constituent atoms are arranged in a periodic manner (as known as long-range order) in three dimensions. When these metals and alloys melt, they lose their crystallinity and the atomic arrangement becomes random and less dense. Accordingly, the volume and the mobility of constituent atoms increase and the viscosity decreases in the liquids state. Thus, from the structural and thermodynamic perspective, the liquid is amorphous and in equilibrium state above the melting temperature. For some metallic melts, if the liquid solidifies with sufficiently rapid cooling rate, the nucleation and growth of crystallites (crystallization) can be bypassed and the liquid phase persists until a temperature well below melting temperature T_m . In this deeply undercooled state the viscosity becomes so high and the liquid gets frozen-in. This

frozen-in liquid possesses a liquid-like structure and characteristics of solid metals simultaneously. By analogy, an alloy that i) possess no long-range order (crystallinity) of constituent atoms that their crystalline counterparts usually have, and ii) vitrified by continuous cooling from the melt is referred as a metallic glass [33].

The history of metallic glasses began with the Duwez's discovery in 1960 (Caltech USA) [34]. They had discovered the first metallic glass in Au-Si system by rapid quenching technique, known as the *gun* technique providing a very high cooling rates about 10^6 K s^{-1} . In this technique, a small droplet of the alloy melt was propelled onto the surface of a highly conducting copper substrate and spread out in the shape of thin foil. The amorphous state of the Duwez's alloy was synthesized by showing no evidence for any crystallinity at all but a few broad diffuse maxima instead in its X-ray diffraction (XRD) pattern. Soon afterwards, a simple criterion of a favorable condition for glass formation in metallic and ionic system was pointed out by Cohen and Turnbull, that is, the low melting eutectic compositions have greater glass-forming tendency [32]. Since this discovery of the new concept of metals and alloys, the metallic glass became the subject of research interest and evolved into an individual field of research. In the early days, a thin film, ribbons or wires were the only possible forms of metallic glasses that can be obtained. However, a bulk metallic glass was developed in a Pd-based alloy in the early 1980s [35], following this a number of researchers began in earnest the systematic study and development of new bulk metallic glass forming systems especially for the industrially favored systems such as Cu- [41,42,43], Fe- [37,38,40,44], Mg- [36] and Ti- [39] based alloys.

2.2.2 Glass formation in metallic alloys

As with all kinds of matter, metals and alloys also come in three fundamental states depending on the strength of bonds holding the constituent atoms (Let's leave the plasma state out of discussion). They are gaseous, liquid and solid phases. In general, when a material is cooled or pressured, it experiences two abrupt changes in structure and properties (phase transformations). They are the condensation (gas \rightarrow liquid transition) and the solidification (liquid \rightarrow solid transition) [28]. Fig. 2.4 schematically depicts the paths of these phase transitions, especially the two distinct solidification paths for a liquid. The first solidification path is known as the crystallization. When the cooling rate is sufficiently

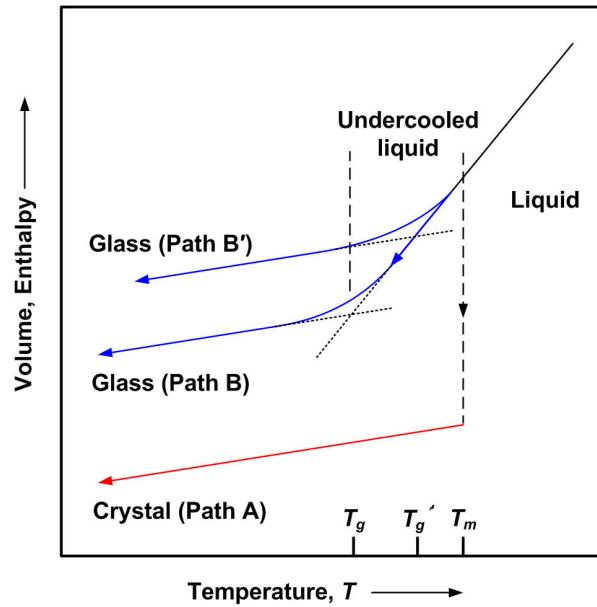


Figure 2.4: Cooling rate dependence of solidification paths, crystallization (path *A*) and glass formation (path *B*). The higher the cooling rate (path *B'*), the glass transition occurs earlier at a relatively higher temperature T_g' .

low, the solidification of liquid takes Path *A* in Fig. 2.4. Through Path *A*, the transition from liquid to crystal takes place at the melting temperature T_m , where properties such as volume, viscosity, enthalpy and entropy change discontinuously. The result is a conventional crystalline solid with a long-range order in the atomic arrangement. However, when the cooling rate is higher than a critical value, liquid bypasses the nucleation and growth of crystallites, but instead the solidification takes place through an alternative process Path *B*. When the liquid phase perseveres until a lower temperature, the liquid approaches to the glass transition temperature T_g , accompanied with the continuous change in properties such as volume, enthalpy and entropy. The continuous change in such properties let the glass transition seem like a second-order phase transition. However, as shown in Fig. 2.4, glass transition is cooling rate dependent and the corresponding T_g is not an intrinsic property but a temperature interval [45,46]. At a temperature around T_g , the liquid gets frozen-in, and this frozen liquid is referred to as glass (metallic glass). Unlike their crystalline counter parts, glasses obtained by this alternative solidification, Path *B*, exhibit no long-range order but highly disordered atomic arrangement. The more the undercooled liquid is stable against crystallization, the easier a glass can be vitrified. The ability of an alloy to be solidified as a glass during quenching a melt is referred to as the

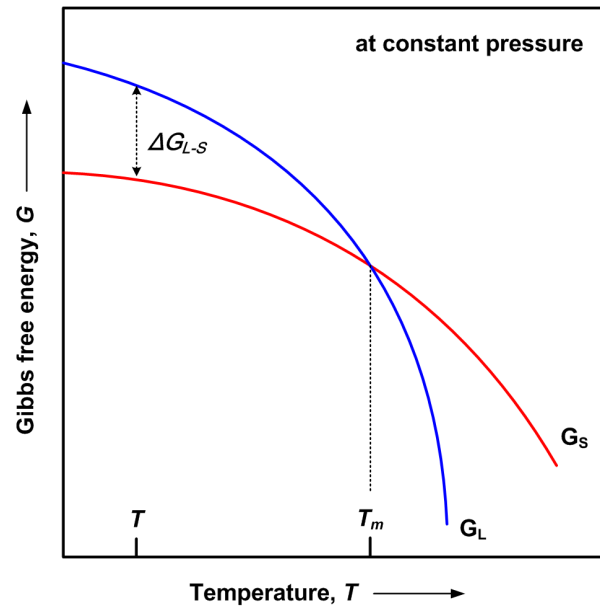


Figure 2.5: Schematic illustration of Gibb’s free energy of the liquid and crystalline solid state as a function of temperature.

glass forming ability (GFA). From a fundamental perspective, glass formation and GFA can be described by different aspects as following.

Fig. 2.5 schematically depicts the temperature dependence of the Gibb’s free energy G for a metallic material in liquid state G_L and in crystalline solid state G_S (at a constant pressure). Usually, the melt will experience the crystallization at the melting temperature T_m during cooling. With further cooling to a temperature below T_m , the system will take the path G_S to attain the lowest free energy value. However, if a rapid heat extraction occurs by quenching at a cooling rate above a critical value (about $10^3 - 10^9 \text{ K s}^{-1}$ for metallic liquid), the melt not only cools faster, but also experiences a significant undercooling [47,48]. The undercooling (also known as supercooling) is the process of lowering the temperature of a liquid below the melting temperature T_m with maintaining a liquid form [49,50].

Generally, if a melt is in the undercooled state, due to the Gibb’s free energy difference between the solid and the liquid phases, ΔG_{L-S} , a great driving force for crystallization is accumulated and the system, therefore, naturally tends to achieve the crystalline state. This makes the undercooled liquid and glasses to be in non-equilibrium, i.e. they are metastable. In order to maintain the undercooled state of a liquid to a sufficiently low temperature for freezing it, the driving force for the crystallization must be

minimized. That is, the free energy difference ΔG_{L-S} must be very low or negative. By mathematical definition,

$$\Delta G_{L-S} = \Delta H_f - T\Delta S_f, \quad (2.4)$$

where ΔH_f and ΔS_f are changes in the enthalpy and entropy of fusion, respectively. A very low or a negative value of ΔG_{L-S} can be obtained either by decreasing the value of the enthalpy ΔH_f or increasing the value of entropy ΔS_f or both. A higher ΔS_f results in an increase in the degree of dense random packing of constituent atoms, which also leads to a decrease of enthalpy ΔH_f . Thus, the larger the number of components in the alloy system, the higher the glass forming ability can be achieved. ΔH_f is also low for the systems of low melting temperature and therefore, a composition at close to eutectics are favorable for glass formation. Theoretically, if the liquid could be cooled fast and far enough to bypass or avoid crystallization, the glass formation could be achieved in every liquid [51]. Thus, the fact whether a glass formation takes place or not is strongly related to the kinetics of crystallization, i.e. the nucleation rate must be low for better GFA. The nucleation rate I , for the homogeneous nucleation from an undercooled melt under the assumption that nuclei is in spherical shape and the compositions of melt and nuclei are identical was derived by Turnbull [52]:

$$I = \frac{k}{\eta(T)} \exp \frac{-b\alpha^3\beta}{T_r(\Delta T_r)^2}, \quad (2.5)$$

Where

b is a geometric shape factor ($b= 16\pi/3$ for a spherical nucleus)

k is a kinetic constant

$\eta(T)$ is the viscosity of the undercooled liquid at temperature T

T_r is the reduced temperature ($T_r = T/T_m$)

ΔT_r is the reduced undercooling ($\Delta T_r = 1 - T_r$)

α and β are dimensionless parameters related to the liquid/solid interfacial energy (σ_{L-S}) and to the entropy of fusion ΔS_f , respectively

The equation 2.5 clearly shows that for a given temperature and viscosity η , as the term $\alpha^3\beta$ increases, which means a decrease in ΔH_f and/or an increase in σ_{L-S} and ΔS_f , the nucleation

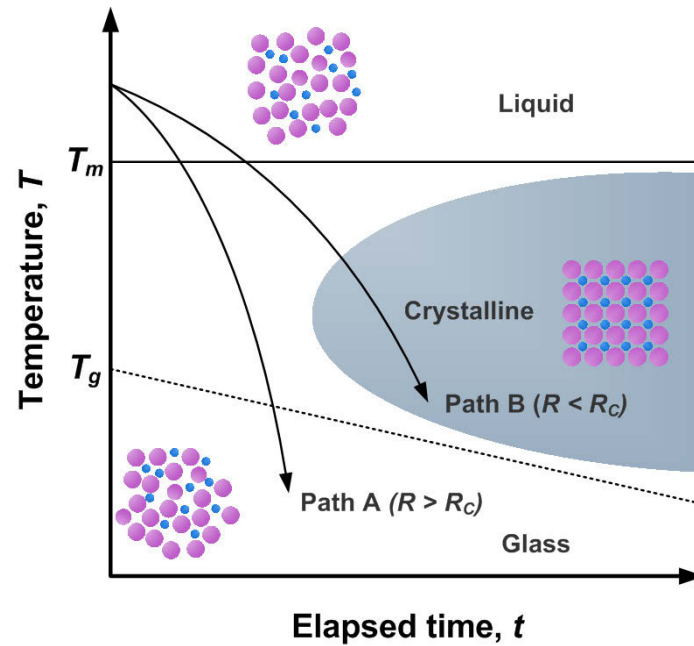


Figure 2.6: Schematic *TTT* diagram with different cooling rates and corresponding solidification paths: (path *A*) glass formation and (path *B*) crystallization.

rate I , becomes slow drastically. In accordance with the equation 2.5 when the viscosity of the undercooled liquid is high or if the melting temperature T_m is low or for the both, the nucleation rate I , will be low and therefore, the GFA becomes high [33].

The process of quenching a melt is best described by the time-temperature-transformation (*TTT*) diagram, as shown in Fig. 2.6. The nose-shape boundary in the *TTT* diagram, separating the domains of undercooled liquid state and crystalline state is where the crystallization rate reaches a maximum. The temperature range between the T_m and the T_g is called the undercooled liquid region (supercooled liquid region) in which the material is metastable. When a liquid cools below its melting temperature T_m (also known as liquidus), the solidification paths are completely different depending on applied cooling rate R . If the cooling rate is not sufficiently fast $R < R_c$, the solidification path *B* will be favored and therefore, the crystallization occurs. In order to preserve the amorphous state until the temperature is low enough for the liquid to undergo a glass transition (path *A*), the liquid must be cooled at a critical cooling rate R_c (over 10^5 K s^{-1} for metallic glasses for example) or even faster. It was already discovered by experiments in 1960s, that larger than a critical value of atomic size mismatch found to be about 15 % is necessary for suppressing the tendency for crystallization [53]. A theoretical study later confirmed that the value fits to the results [54]. It is therefore clear that the atomic sizes of constituent

elements and their difference play an important role in glass formation. Based on the above-described findings in this chapter, Inoue *et al.* [55,56] have summarized and proposed three empirical rules for the achievement of high glass forming ability: (i) The alloy should be a multi-component system consisting of at least three elements, (ii) significant atomic size mismatch of more than 12 % should exist, and (iii) large negative heats of mixing (enthalpy of mixing ΔH_{mix}) among three main constituent elements should be fulfilled.

2.3 Phase separation in metallic glasses

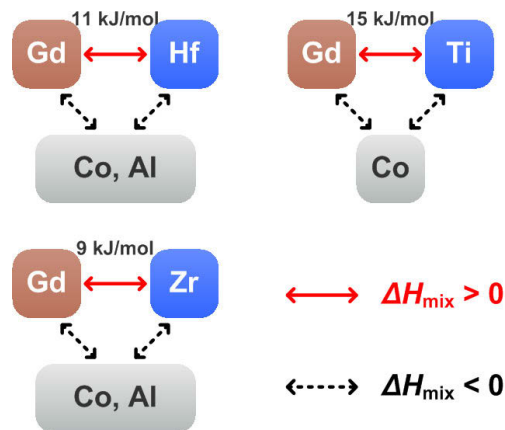


Figure 2.7: Mixing enthalpy relationship between constituent elements of the alloy systems studied in this work. The positive ΔH_{mix} between two main constituents are shown by solid line with the values from Ref. [9,10]

As just introduced above, a positive enthalpy of mixing between constituent elements is the most important prerequisite for phase separation. It has also been mentioned above that a large negative enthalpy of mixing is required to achieve a better glass forming ability. Therefore, these two criteria seem to be contradictory to each other. However, these conflicting prerequisites can be satisfied by introducing an element possessing a positive enthalpy of mixing with at least one of the constituents of the glass forming system. Fig. 2.7 shows values of the enthalpy of mixing between constituents for some alloys studied in this work. The values of enthalpy of mixing presented in this work were quoted as calculated by the Miedema's model for an A - B system ($\Delta H_{\text{mix}}^{A-B}$) at an

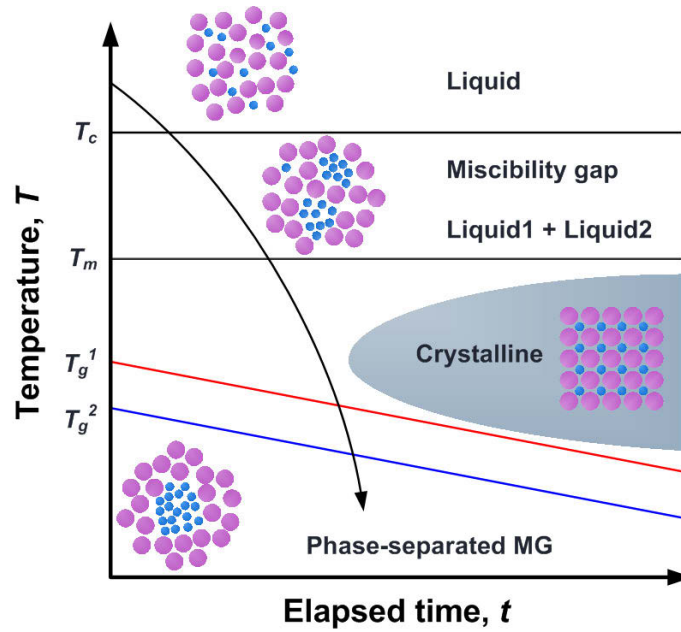


Figure 2.8: Schematic *TTT* diagram for a hypothetical alloy possessing a miscibility gap.

equi-atomic composition [9,10]. Obviously, rapid quenching of a melt is essential for both conditions. If both the criteria are simultaneously satisfied in an alloy system, phase separation in metallic glass can be observed. Once a phase separation occurred during quenching of the melt, the composition of each separated liquid phases (newly formed liquids with composition X_1 and X_2 in Fig. 2.2b, for example) and corresponding glass forming ability determine the final structure of the alloy. The kinetics of phase separation and glass formation upon continuous cooling is best described by *TTT* diagram. Fig. 2.8 shows a schematic *TTT* diagram for a hypothetical alloy possessing a miscibility gap. When the alloy melt is cooled from above the critical temperature of miscibility gap T_c at a cooling rate indicated by solid curve, the melt of homogeneous liquid phase enters into miscibility gap at temperature T_c . Then liquid-liquid phase separation takes place and decomposes the melt into two different liquid phases. The resultant two liquids are completely different in chemical composition. Therefore, if the alloy melt consisting of two separated liquids is further cooled, the solidification and/or vitrification of the liquids undergo separated scenarios with different glass transition temperatures (T_g^1 and T_g^2). If both separated liquids exhibit sufficient GFA and the applied cooling rate is fast enough the glass-glass composite (glassy phase reinforced metallic glass) will be obtained. However, if the GFA of one or both the liquid is not sufficiently high enough, alternative composites like glass-crystalline or crystalline-crystalline for example will be finally obtained. Based on this scenario with respect to liquid-liquid phase separation, Kündig *et*

al. reported the first phase-separated metallic glass in La-Zr-Cu-Ni-Al system [6]. Later Park *et al.* and Mattern *et al.* also reported phase-separated metallic glass formation in quaternary Y-Ti-Al-Co system [7] and a ternary Nb-Ni-Y system [8] in succession. Table 2.1 summarizes the results of phase separation reported in different alloy systems together with the indication of atom pairs exhibiting positive enthalpy of mixing in the liquid state.

Table 2.1: Reported alloy systems exhibiting liquid-liquid phase separation. Elements written in bold type represent atom pair with positive enthalpy of mixing in the liquid state.

Alloy systems	Synthesis method	Enrichment of the two glassy phases	References
La-Zr -Cu-Ni-Al	Melt spinning	La-rich and Zr-rich phases	[6]
Ti-Y -Co-Al	Melt spinning	Ti-rich and Y-rich phases	[7]
Ni- Nb-Y	Melt spinning	Ni-based glassy phases with Nb- and Y enrichment	[8]
Cu-Zr-Al-Ag	Cu-mold casting	Ag-rich glassy particles in Cu-rich glassy matrix	[11]
Zr-Nd -Al-Co	Melt spinning	Zr-rich and Nd-rich phases	[13]
Cu-(Zr,Hf)-(Gd, Y)-Al	Melt spinning Cu-mold casting	Gd-rich and Hf-rich phases or Y-rich and Hf-rich phases	[14]
Zr-(Ce,Pr) -Al-Ni	Melt spinning	Zr-rich and RE-rich phases (RE = Ce, Pr)	[57]
La-Y-Ti -Al-Co	Melt spinning	Ti-rich, Y-rich and La-rich phases	[58]
Al-Ni-Y-Co-Pb	Melt spinning	Pb-rich particles in Al-rich glassy matrix	[59]

Chapter 3: Experimental methods

3.1 Alloy preparation

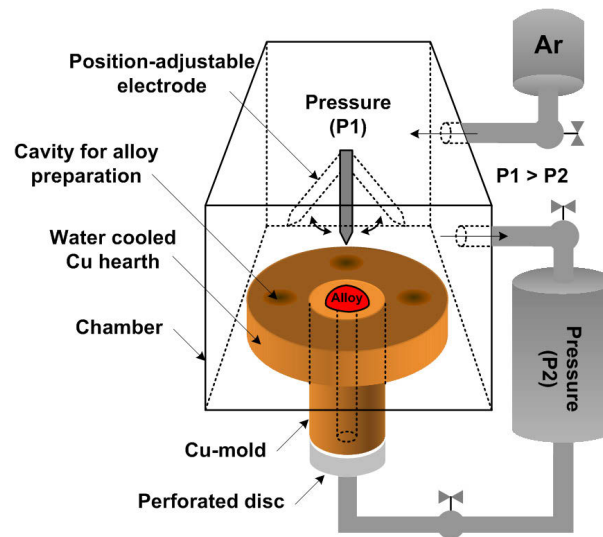


Figure 3.1: Schematic illustration of the arc melting instrument combined with a suction facility at the IFW-Dresden.

The samples of the alloys investigated in this thesis were prepared in different systems as well as in a variety of forms i.e. the shape of ingots, cylindrical rods and ribbons, depending on their purpose. Several compositions in binary Gd-Zr, Gd-Ti and ternary Gd-Ti-Co systems were prepared to investigate the phase equilibria of the sub-systems with a miscibility gap on one hand and the alloys in quaternary Gd-TM-Co-Al (TM = Hf, Ti or Zr) systems were investigated for the synthesis of new phase-separated metallic glass and the structure formation on the other hand. Master alloy ingots were prepared by arc melting (Arc melter: Edmund Bühler GmbH device no. 2414048) under a purified Ti-gettered argon atmosphere on a water-cooled copper substrate. In order to keep the oxygen content of the alloys as low as possible and to achieve homogeneity, elements purity of 99.9% or higher were used and the ingots were remelted at least 3 times. For the cylindrical rods with a diameter of 2 mm and a length of about 20 - 80 mm, 5 g of master alloys were

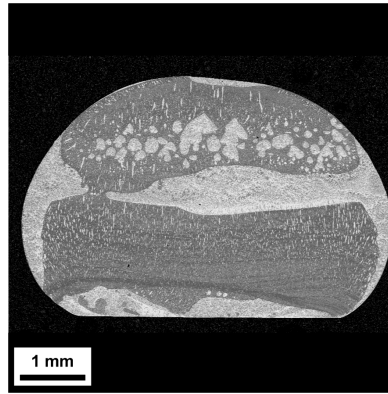


Figure 3.2: SEM image of the cross section for a Gd-Ti as-cast ingot. The brighter and darker contrasts represent the Gd-rich and Ti-rich phases, respectively.

melted and directly quenched into water-cooled copper moulds by an in-situ suction facility attached to the arc melter. A schematic illustration of the arc melter with an *in situ* suction facility is shown in Fig. 3.1. The difference in sample mass after arc melting was less than 0.1 %, which is negligible. In order to produce ribbons, a single roller melt spinning facility (Edmund Bühler GmbH) with a copper wheel of 20 cm in diameter was employed. It should be noted here that in the phase separating alloys the microstructure of as-cast master alloy is severely inhomogeneous as shown in Fig. 3.2. Therefore, taking a piece of master alloy of larger size, like taking quarter of 20 g or half of 10 g ingots for example must be avoided. Otherwise the composition of melt-spun ribbon is not warranted. For this reason, 5 - 6 g of master alloys were individually prepared in order to obtain the same chemical composition from produced ribbons as nominal composition of alloys. The master alloy was inductively melted in a quartz crucible (QSIL AG, Quarzschmelze Ilmenau). The Quartz crucible has a rectangular nozzle tip of 3-4 mm length and 0.7 mm width. The position of the nozzle tip was adjusted to about 0.3 mm respect to the rapidly rotating wheel surface. An overpressure of about 300 mbar of 99.9 % pure argon was applied from an external reservoir to eject the molten alloy. Prior to casting the chamber was evacuated to a pressure of 10^{-5} - 10^{-6} mbar. The temperature was monitored by an external two-color pyrometer from the upper surface of the molten alloy through a quartz window. The applied velocity of wheel rotation was 30 m/s. The dimension of resulting ribbons were approximately 3-4 mm width and 30-50 μm thickness. A schematic illustration of melt spinning facility is shown in Fig. 3.3

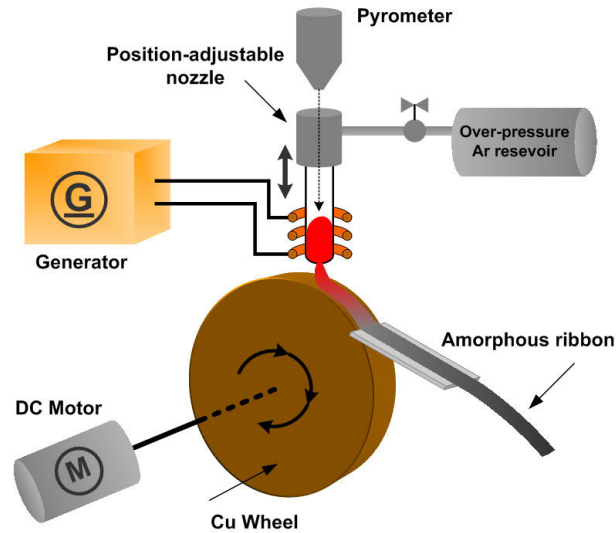


Figure 3.3: Schematic illustration of the melt spinning facility at the IFW-Dresden.

3.2 Analysis techniques

3.2.1 Chemical analysis

In order to confirm the actual composition of the samples for phase diagram study in chapter 4, chemical analysis was performed by A. Voß in the chemical analysis group of the IFW-Dresden, using a inductively coupled plasma with optical emission spectrometry (ICP-OES) (IRIS Intrepid II XUV: Thermo Fisher Scientific GmbH).

3.2.2 Thermal analysis

The onset temperature of the glass transition T_g , and the crystallization temperature T_x for the glassy alloys were determined by differential scanning calorimeter (Diamond DSC: Perkin Elmer) with a heating rate of 40 K/min from 573 K - 933 K. For binary Gd-(Zr, Ti) and ternary Gd-Ti-Co systems the phase transitions, onset temperature of melting T_m and the liquidus temperature T_{liq} , have been checked up to a maximum temperature of about $T = 1950$ K by employing a high temperature differential thermal analysis (DTA:

SETERAM DTA-92) and high temperature DSC (Netzsch DSC-404C). All DSC devices were operated with Al_2O_3 crucible under argon atmosphere. For the high temperature measurements with DTA, ZrO crucible and helium atmosphere were employed in order to minimize the reaction between alloy and crucible at a high temperature regime. The temperature calibration of *in situ* hard X-ray measurement with levitation technique in chapter 4 was also done by the high temperature thermal analysis. The thermal analyses described above were performed by B. Bartusch and J. Werner in the IFW-Dresden.

3.2.3 X-ray diffractions

X-ray diffraction is the one of the most commonly used technique to characterize the structure of materials [60]. Each crystalline solid produces its unique diffraction pattern that consists of sharp peaks at the angles which satisfy the Bragg condition. In contrast to the case of crystalline materials, the amorphous materials produce diffuse halos instead [60]. The X-ray diffraction studies in this work were also carried out in order to analyze the phase formation after rapid quenching or at elevated temperature upon heating (recorded *in situ*). For these investigations, two different types: reflection configuration in Bragg-Brentano geometry and transmission configuration were employed, respectively. A Panalytical X'pert Pro diffractometer using $CoK\alpha$ radiation ($\lambda = 1.78897 \text{ \AA}$), equipped with a sample spinner at the IFW-Dresden was used in order to analyze as-cast ribbons and rods. The diffractometer was operated at a voltage of 40 kV and a current of 40 mA. The intensities were obtained at 2θ values from 20 to 100 degrees with a step size of $\Delta 2\theta = 0.05^\circ$ and 1,000 s exposure time per step.

Small-angle X-ray scattering

The X-ray diffraction in transmission configuration in this work was performed at two synchrotron beam lines of the HASYLAB in Hamburg for different purposes. In order to investigate the temperature and time dependence of the structure formation, and especially to clarify the occurrence of the phase separation prior to crystallization, *in situ* small-angle X-ray scattering (SAXS) in combination with simultaneously recorded wide-angle X-ray scattering (WAXS) was employed. SAXS technique provides the structure information of size from 1 nm to about 100 nm. Small-angle X-ray scattering (SAXS) was

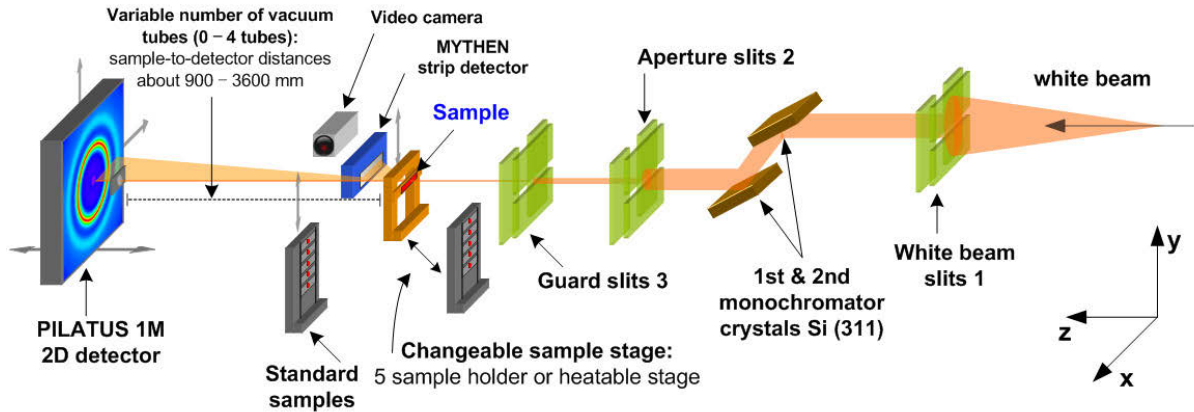


Figure 3.4: Layout of SAXS beamline B1 at HASYLAB, DESY Hamburg. Two detectors record SAXS and WAXS patterns simultaneously.

measured with direct assistance of Dr. U. Vainio at the synchrotron beam line B1 at the HASYLAB/DESY, using an energy of 16 keV. A schematic layout of the beam line is illustrated in Fig. 3.4. Ribbon samples were placed on a heating stage which was used under vacuum for *in situ* measurement. SAXS patterns were registered by a *PILATUS 300 k* area detector at a distance covering a q -range between 0.2 and 4.3 nm⁻¹. The temperature was increased in steps of 10 K. For each temperature, the background was measured, followed by a calibration standard (glassy carbon) and subsequent measurement of the sample. For isothermal analysis, the samples were heated at 100 K min⁻¹ up to the corresponding temperature and measurements were immediately started (10 min per pattern), then repeated for up to 6 hours. Simultaneously the wide-angle X-ray scattering (WAXS) curves were recorded by a linear *MYTHEN* strip detector. We noticed that SAXS data was obtained from q -ranges of about 0.08 - 2.9 nm⁻¹ due to the longest possible sample-to-detector distance (~ 3.6 m). An example of SAXS/WAXS data in Fig. 3.5 shows the dependence of measurable q -ranges on sample-to-detector distance.

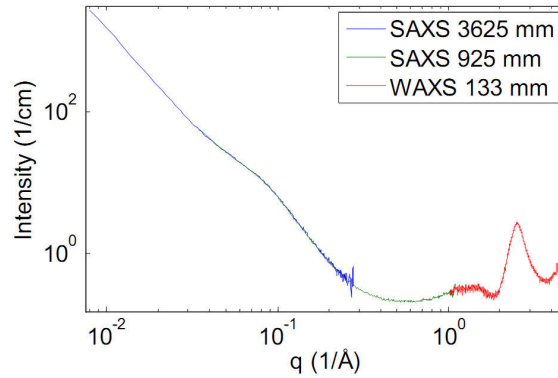


Figure 3.5: An example SAXS/WAXS data obtained at 16 keV. SAXS was measured at two different distances (not simultaneously). The *sample-to-detector distances* are shown in the legend. Adopted from the introduction of the beamline B1 provided by Dr. U. Vainio *et al.* in HASYLAB/DESY.

High energy X-ray diffraction

In order to investigate the phase equilibria of the binary Gd-Ti, Gd-Zr and ternary Gd-Ti-Co systems, *in situ* synchrotron high energy X-ray diffraction was performed in transmission geometry at $E = 100$ keV ($\lambda = 0.01239$ nm) with direct assistance of Dr. J. Bednarčík at the beam-line BW5 of the HASYLAB in Hamburg, Since the studies of high temperature phase equilibria and of metastable phases are very problematic with the changes of the composition by the impurities from melt-crucible reaction and the undesirable heterogeneous nucleation sites provided by sample containers. For this reason, the samples were processed under high vacuum condition in an electrostatic levitation (ESL) instead of the conventional methods. ESL in this work is specially developed as a containerless processing for performing *in situ* X-ray scattering experiment [61,62,63]. It was developed by Dr. D. Holland-Moritz and his group members in the Deutsches Zentrum für Luft- und Raumfahrt (DLR), Köln. External infra-red lasers are applied to heat the sample independently. The sample was cooled either by switching off the lasers or decreasing the current of lasers. The temperature was measured by two pyrometers in different directions. The temperature values obtained from pyrometer were corrected by a calibration of the temperatures of the eutectic reaction and of a solid state phase transformation visible in the diffraction patterns to the DSC measurement. The scattered intensity was continuously recorded by a two-dimensional X-ray

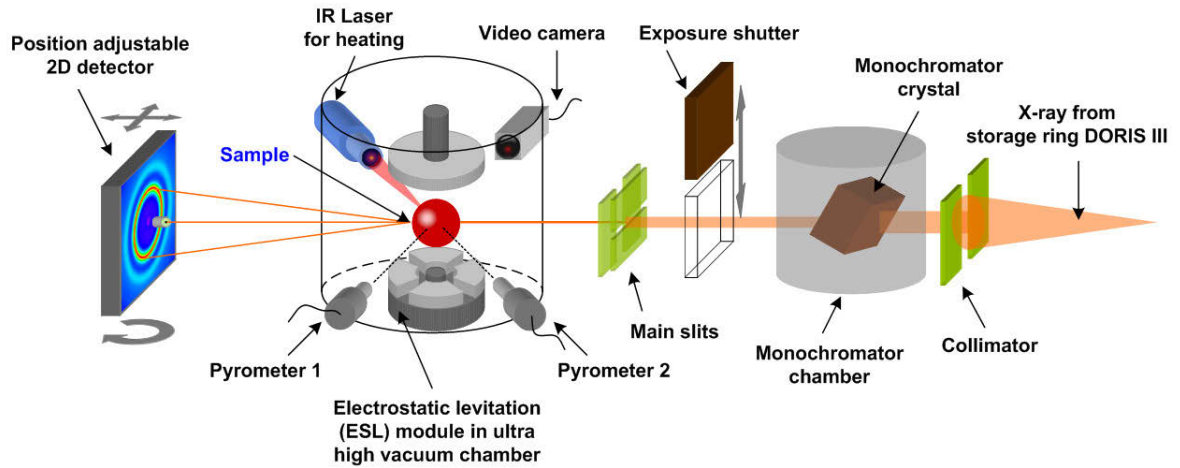


Figure 3.6: Layout of high energy X-ray diffraction beamline BW5 at HASYLAB, DESY Hamburg equipped with the electrostatic levitation (ESL) facility.

detector (PerkinElmer: XRD 1622) with acquisition times of 0.5 and 1 s either at a constant temperature or during heating or cooling. *Fit2D* software package was used to obtain the azimuthal integration of the raw 2D images [64].

For the *in situ* X-ray diffraction experiments with synchrotron in this work, the scattering intensity $I(q)$ is generally given as a function of the scattering vector q :

$$q = \frac{4\pi \sin \theta}{\lambda}, \quad (3.1)$$

where θ is the diffraction angle and λ is the wavelength of the radiation. The Bragg distance is calculated as $d = 2\pi/q$. Since the scattering vector q is independent on the wavelength λ , the use of q is more convenient than use of the scattering angle 2θ . For this reason, the diffraction data in this work is generally shown as a function of the scattering vector q (nm^{-1}).

3.2.4 Electron microscopy

Sometimes the difference between an amorphous structure and an extremely fine-grained crystalline structure is very difficult to distinguish when only techniques like XRD, DSC are used. Hence, for better understanding of either of these material types, additional analytical techniques like microscopy have to be employed together.

For this reason, the microstructure of the samples was investigated by electron microscopy, using the scanning electron microscopy (SEM) and transmission electron microscopy (TEM) at the IFW-Dresden. The SEM studies were carried out with a Zeiss Gemini 1530 (Carl Zeiss AG) operated at 15-30 kV. In order to distinguish between two different glassy phases or the amorphous matrix and precipitates, the backscattered electron (BSE) mode was mainly used. The TEM investigations were performed using two different TEMs, a CM20 FEG (Philips) and a Tecnai F30 (FEI) operated at an accelerating voltage of 200kV and 300kV, respectively. The scanning transmission electron microscopy (STEM) in high angle annular dark field (HAADF) mode was also performed on the Tecnai F30 to obtain the micrographs with better contrast of the precipitates. All microscopes were equipped with energy-dispersive x-ray spectrometer (EDX). The EDX investigation was performed in order to obtain a local chemical composition of the samples. The samples for SEM were ground using conventional grinding papers with sequence of 600 - 1200 - 2400. This was then followed by fine polishing using a (Buehler Phoenix 4000). The samples for TEM investigation were prepared by two different methods either manual grinding followed by ion-milling (Gatan 691 precision ion polishing system PIPS) or focused ion beam (FIB).

3.2.5 Atom probe tomography

In the case of some phase separated metallic glasses and also of glass-forming systems, decomposition or crystallization results in a few nano-meter scale microstructure. Due to this extremely fine dimension of heterogeneities (< 10 nm), microstructure and composition analysis of those heterogeneities using ordinary microscopy is not sufficient. Previously, Park *et al.* have reported that especially for the Cu-Zr-Gd-Al metallic glass system with low concentration of Gd, an enhanced plasticity is obtained [14]. This has

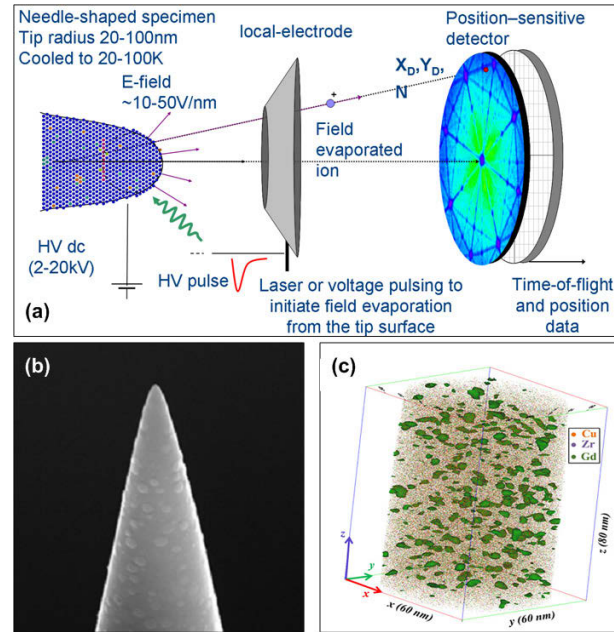


Figure 3.7: (a) Schematic illustration of the basic principles of the APT technique (taken from Ref. [65]). (b) Image of a needle-shaped specimen. (c) Reconstructed 3D image of a Cu-Zr-Gd sample revealed phase separation [66].

been explained by phase separation induced local chemical heterogeneity in the amorphous matrix. However the direct evidence for that was not provided. For this reason, we decided also to apply atom probe tomography (APT) investigations on the Zr-Gd-Co-Al system to understand if the alloys in the initial state are homogeneous amorphous or are phase separated and to also obtain microstructure with elemental concentration in atomic resolution. The basic principles of the APT technique are schematically shown in Fig. 3.7a. This technique produces three-dimensional images of needle-shaped metals with its internal structure by reconstruction of thousands of two-dimensional slices which are analyzed by a two dimensional position sensitive detector (right hand side in Fig. 3.7a). In this work, a dual-focus ion beam system (FEI Strata 400) was used for the fabrication of the atom probe tomography (APT) tips. The APT specimens were analyzed using the local electrode atom probe (LEAP 3000 X SiTM) equipped with diode-pumped solid -state laser operating at the second harmonic frequency of 532 nm , with a pulse duration of ~ 10 ps and a laser spot size of $< 10 \mu\text{m}$. Pulse laser atom probe analyses were carried out at 27 K and an average detection rate of $0.005 \text{ ions pulse}^{-1}$. Atom probe tomography (APT) investigations were performed by Dr. A. Shariq in the Fraunhofer-CNT in Dresden.

3.3 Magnetic measurements

The field and temperature dependence of magnetization were measured with a magnetic property measurement system (Quantum Design MPMS XL7) and physical property measurement system (Quantum Design) equipped with the VSM option at the IFW-Dresden. Temperature dependence of magnetization curves (M - T) of the samples was measured in a field of 100 Oe. The Curie temperature T_{Curie} is determined as the temperature where the absolute values of the first derivative dM/dT are maximum. In order to determine the saturation magnetization σ_s , the ribbon samples were measured up to 5 - 9 T at 10 K. The coercivities were also estimated from the field dependence of magnetization results. Magnetic measurements were performed by Dr. B. Schwarz in the IFW-Dresden.

Chapter 4: Experimental results

4.1 Experimental assessment of Gd-Zr, Gd-Ti and Gd-Ti-Co phase diagrams

As described in previous chapters, understanding the phase equilibria in binary immiscible system i.e. Gd-Zr and Gd-Ti in this work is the most important step towards the development and investigation of the phase separated metallic glasses in multi-component system. This chapter introduces the results of the investigations carried out on the binary Gd-Zr, Gd-Ti and ternary Gd-Ti-Co systems and corresponding discussions.

4.1.1 The binary Gd-Zr system

The binary Gd-Zr system plays an important role for the alloys of magnetic applications, i.e. the magnetic properties can be tuned and monitored by tailoring the alloys with the Gd-Zr system [67,68,69,70]. Furthermore, the addition of Gd enhances the glass forming ability of Cu-Zr-Al alloys to be prepared as bulk metallic glasses (BMG) [71]. Recently, in Cu-Zr-Gd system, phase separated metallic glasses could be also prepared by rapid quenching of melts [66].

The phase diagram for the Gd-Zr system is of the *eutectic type* with no intermetallic phases [23]. The first experimental phase diagram has been reported by Copeland *et al.* in 1961 [72]. The experimental methods in their work were differential thermal analysis (liquidus, solidus, eutectic and peritectoid), X-ray diffraction and optical microscopy of annealed samples (solubility). Electrical resistivity was also investigated for solid-state transformations. The composition and temperature for eutectic reaction were found to be near 27.5 at.% Zr, and at $T = 1491 \pm 5$ K, respectively. The solubilities were determined to be about 3 at.% Zr in *hcp*-Gd at $T = 873$ K and 6.7 at.% Gd in *bcc*-Zr at $T = 1533$ K. A few years later, additional information on the solubility of Zr in *hcp*-Gd was also reported by Copeland *et al.* in Ref. [73]. The thermodynamic mixing properties are unknown so far.

Based on these limited data, a thermodynamic dataset for the Gd-Zr system has been optimized by Zinkevitch *et al.* [74]. The calculated phase diagram is in good agreement with the published experimental findings, except for the eutectic composition which was calculated to be 12 at.% Zr. In a recent report by Schmitz *et al.* [75] it is concluded a value of about 25 at.% Zr from the investigation on the microstructure of cast Gd-Zr alloys. Thus, all the former reports were suffered from uncertainties of the experimental data at higher temperatures especially for the liquid phase equilibria. Under such conditions of higher temperature, the experimental difficulties such as weak signal and very high reactivity between metallic melts and the container arise and hamper the acquisition and determination of thermodynamic properties.

Therefore, as an alternative method *in situ* investigation on liquid-solid phase equilibria was applied by using high-energy synchrotron X-ray diffraction on levitated melt drops. Recently, there have been reports where the assessment of phase diagrams containing reactive elements were successfully investigated by this technique [76,77]. The experimental setup for this technique was introduced in a previous chapter (see chapter 3). In order to investigate the microstructure and thermal behavior, alloy ingots of Gd_xZr_{100-x} ($x = 17, 20, 23, 35, 50$ and 65 at.%) are directly cast into cylindrical rods with 3 mm diameter using copper mold casting method. For *in situ* X-ray diffraction investigations, alloy ingots of 200 mg mass with nominal compositions $Gd_{65}Zr_{35}$, $Gd_{50}Zr_{50}$ and $Gd_{35}Zr_{65}$ were prepared by arc-melting. The sizes of the spherical shaped ingots were about 4 mm in diameter which is sufficient for the electro static levitation (ESL) technique. The difference in sample mass after arc-melting was less than 0.1%.

4.1.1.1 *In situ* observation of phase equilibria at elevated temperatures

Fig. 4.1 shows DSC trace of the $Gd_{50}Zr_{50}$ alloy upon heating and cooling within temperature range of 723 - 1673 K. Three phase transformations are indicated upon heating. The cooling curve also exhibits these transformations together with the usual slight undercooling, and the two transitions at high temperature are dissolved. For the other alloys $Gd_{65}Zr_{35}$ and $Gd_{35}Zr_{65}$, the transition temperatures were identical with those of $Gd_{50}Zr_{50}$ alloy. The transition temperatures are summarized in Table 4.1.

The *in situ* XRD patterns unambiguously determine the corresponding phase reactions. Selected XRD patterns $I(q)$ of the $Gd_{35}Zr_{65}$ alloy as a function of temperature

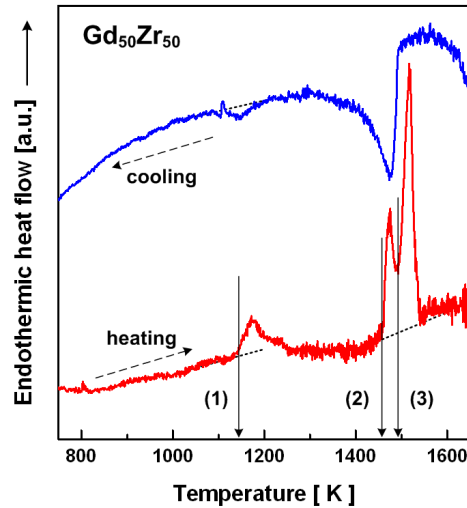


Figure 4.1: DSC trace of $\text{Gd}_{50}\text{Zr}_{50}$ up to 1673 K recorded at a heating rate of 20 K/min; heating and cooling curves are shown.

representing the characteristic phase equilibria determine the different temperature ranges of coexist phases as shown in Fig. 4.2. The hexagonal phases $hcp\text{-Gd}(\text{Zr})$ and $hcp\text{-Zr}(\text{Gd})$ coexist below $T = 1140$ K. The reaction (1) on the DSC curve at $T = 1150$ K (Fig. 4.1) corresponds to the transformation (i) $hcp\text{-Zr}(\text{Gd}) \leftrightarrow bcc\text{-Zr}(\text{Gd})$ in the Fig. 4.2 which is in accordance with [23,72,73,74]. We observe the equilibrium between $hcp\text{-Gd}(\text{Zr})$ and $bcc\text{-Zr}(\text{Gd})$ phases between $1150 \text{ K} < T < 1450$ K. The reaction (2) on the DSC curve at $T = 1452$ K is related to the transformation (ii) $hcp\text{-Gd}(\text{Zr}) \leftrightarrow bcc\text{-Zr}(\text{Gd})$. At temperature range $1455 \text{ K} < T < 1495$ K the coexistence of $bcc\text{-Gd}$ and $bcc\text{-Zr}$ phases is evident. The DSC event (3) at $T = 1495$ K corresponds to the eutectic reaction $L \leftrightarrow bcc\text{-Gd} + bcc\text{-Zr}$. The melting of the sample can be seen by the disappearance of the reflections for $bcc\text{-Gd}$ phase and the occurrence of a diffuse diffraction maximum in the *in situ* XRD patterns reveal the melting of the sample. Above $T = 1495$ K the Gd-rich melt is in equilibrium and coexists with the $bcc\text{-Zr}$ phase then the sample is semi-solid regime. During further heating for $\text{Gd}_{35}\text{Zr}_{65}$ the fraction of $bcc\text{-Zr}$ decreases with temperature up to $T = 1830$ K, and above $T_{\text{liq.}} = 1830 \pm 20$ K only liquid phase is present. A systematic shift of the position of the diffuse maxima (dashed line in Fig. 4.2) with temperature which corresponds to the change of the composition of the Gd(Zr) melt is observed in the semi-solid regime. In the *in situ* XRD patterns for the $\text{Gd}_{65}\text{Zr}_{35}$ and $\text{Gd}_{50}\text{Zr}_{50}$ alloys the same phase sequences were also observed, however with different fractions of the phases corresponding to the lever rule.

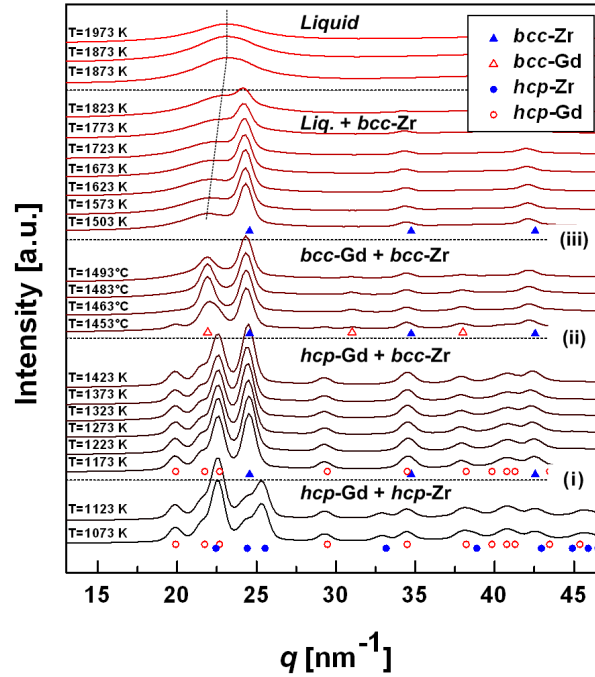


Figure 4.2: Selected XRD patterns of $Gd_{35}Zr_{65}$ at elevated temperatures. Different symbols are indicating the positions of reflections of the crystalline phases. Horizontal dashed lines marks the phase transitions. Diagonal dashed line indicates the position of the diffuse maxima of the Gd(Zr) liquid phase.

The liquidus temperature $T_{liq.} = 1680 \pm 20$ K and $T_{liq.} = 1780 \pm 20$ K were determined for $Gd_{65}Zr_{35}$ and $Gd_{50}Zr_{50}$, respectively.

Fig. 4.3 shows in detail the positions of the diffuse maximum q_1 of Gd(Zr) liquid and the (110)-reflection of the bcc -Zr(Gd) phase $q_{(110)}$ as a function of temperature. The presented values of data were calculated by a fit of the diffraction maxima and peaks obtained from independent measurements of four different samples, two from $Gd_{35}Zr_{65}$, and one from $Gd_{50}Zr_{50}$, and $Gd_{65}Zr_{35}$. In general, the position of the first diffuse maximum q_1 for metallic glasses and metallic liquids scales approximately with a concentration-averaged atomic diameter d of the alloy analogously to the Ehrenfest equation [78]:

$$q_1 = k2\pi / d \quad (4.1)$$

with a constant $k \approx 1.2$, and $d = \sum c_i \times d_i$, where d_i and c_i are the atomic diameter and the concentration of element i . This equation is not exactly valid, but the change in q_1 nevertheless can be often well described by a linear dependence on the concentration c_i of

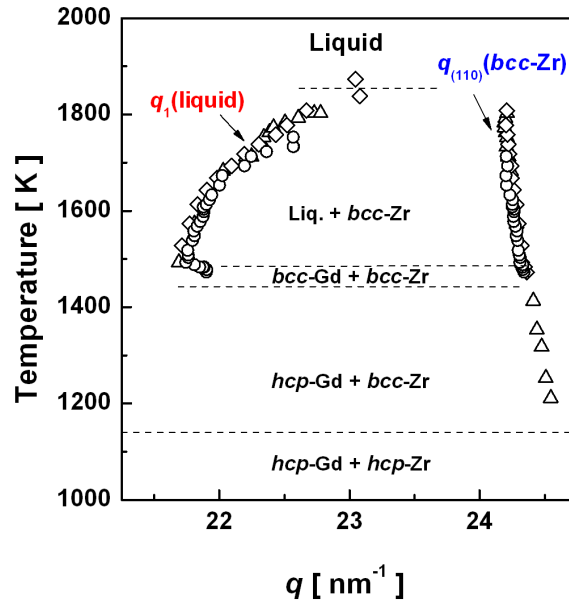


Figure 4.3: Positions of the first maximum q_1 of the Gd(Zr) liquid, and $q_{(110)}$ of $bcc\text{-Zr}$ vs. T , data are from different measurements of Gd-Zr alloys (open circle: $\text{Gd}_{50}\text{Zr}_{50}$, triangle: $\text{Gd}_{35}\text{Zr}_{65}$ (sample a), rhombi: $\text{Gd}_{35}\text{Zr}_{65}$ (sample b))

the added element within an element substitution series [79,80]. An increased solubility of smaller atom Zr ($d_{\text{Zr}} = 0.316$ nm) in the Gd-rich liquid ($d_{\text{Gd}} = 0.362$ nm) which reduces the average atomic diameter explains the experimentally observed shift of the position of the first maxima q_1 to larger q -values with rising temperature. The thermal expansion has almost a negligible influence on the shift of the position q_1 , i.e., it is one order of magnitude smaller.

As shown in Fig. 4.4, the characteristic q_1 -values of the Gd-Zr liquid corresponding to the given alloy compositions were obtained from the XRD patterns at $T > T_{\text{liq}}$. The extracted concentration dependence of the maximum position q_1 as a function of Zr content $q_1(x_{\text{Zr}})$ is shown in the inset of Fig. 4.4. This can be well described by a linear fit function $q_1(x_{\text{Zr}}) = 21.18 \pm 0.031x_{\text{Zr}}^{\text{Liquid}}$ of the chemical composition in at.%. The extrapolation to $x_{\text{Zr}} = 100$ is in a good agreement with the value of liquid Zr reported in the literature [81].

Table 4.1: Invariant reactions, transition temperatures of the Gd-Zr system

Reaction	T (K)		calc. compositions of phases (at.%)		
	calc.	exprimet	1	2	3
$L \leftrightarrow bcc\text{-Gd} + bcc\text{-Zr}$	1495	1495 ± 10	$\text{Gd}_{83.6}\text{Zr}_{16.4}$	$\text{Gd}_{92.7}\text{Zr}_{7.3}$	$\text{Gd}_{4.9}\text{Zr}_{95.1}$
$bcc\text{-Gd} \leftrightarrow hcp\text{-Gd} + bcc\text{-Zr}$	1441	1452 ± 10	$\text{Gd}_{94.5}\text{Zr}_{5.5}$	$\text{Gd}_{96.2}\text{Zr}_{3.8}$	$\text{Gd}_{4.4}\text{Zr}_{95.6}$
$hcp\text{-Gd} + bcc\text{-Zr} \leftrightarrow hcp\text{-Zr}$	1159	1145 ± 10	$\text{Gd}_{97.0}\text{Zr}_{3.0}$	$\text{Gd}_{1.9}\text{Zr}_{98.1}$	$\text{Gd}_{2.8}\text{Zr}_{97.2}$

The lattice parameters of *bcc*-Zr(Gd), *bcc*-Gd(Zr) and *hcp*-Gd(Zr) were determined from the *in situ* XRD patterns and summarized in Table 4.2.

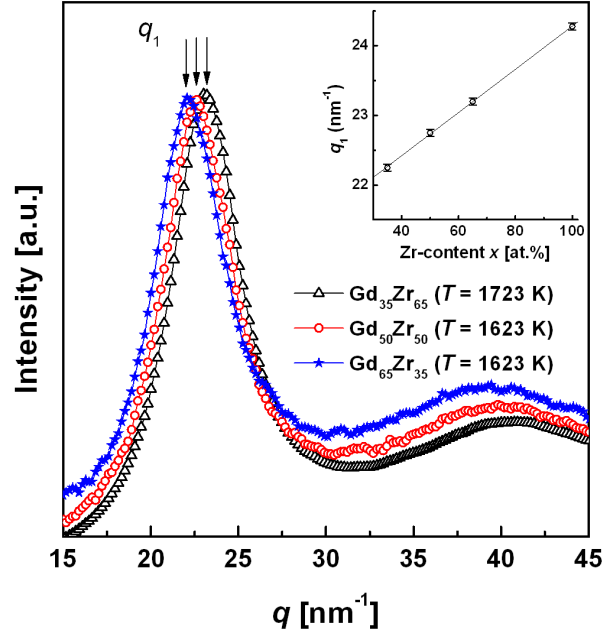


Figure 4.4: Diffraction patterns $I(q)$ of different $\text{Gd}_{100-x}\text{Zr}_x$ liquids. The position of the first diffuse maximum at q_1 as a function of the Zr-content x_{Zr} is shown in the inset. The value of q_1 for liquid Zr is adopted from Ref. [81].

Table 4.2: Constituent phases and lattice parameters a_0 , c_0 of hexagonal and cubic Gd(Zr) and Zr(Gd) phases at elevated temperatures of $\text{Gd}_{35}\text{Zr}_{65}$.

T (K)	Phases	Gd(Zr)		Zr(Gd)	
		a_0 (nm)	c_0 (nm)	a_0 (nm)	c_0 (nm)
1051	<i>hcp</i> -Gd + <i>hcp</i> -Zr	0.3653 ± 1	0.5820 ± 2	0.3256 ± 1	0.5175 ± 2
1123	<i>hcp</i> -Gd + <i>hcp</i> -Zr	0.3653 ± 1	0.5827 ± 2	0.3259 ± 1	0.5177 ± 2
1211	<i>hcp</i> -Gd + <i>bcc</i> -Zr	0.3657 ± 1	0.5833 ± 2	0.3620 ± 1	-
1253	<i>hcp</i> -Gd + <i>bcc</i> -Zr	0.3656 ± 1	0.5841 ± 2	0.3626 ± 1	-
1318	<i>hcp</i> -Gd + <i>bcc</i> -Zr	0.3655 ± 1	0.5844 ± 2	0.3630 ± 1	-
1353	<i>hcp</i> -Gd + <i>bcc</i> -Zr	0.3654 ± 1	0.5845 ± 2	0.3636 ± 1	-
1413	<i>hcp</i> -Gd + <i>bcc</i> -Zr	0.3653 ± 1	0.5850 ± 2	0.3640 ± 1	-
1423	<i>hcp</i> -Gd + <i>bcc</i> -Zr	0.3656 ± 1	0.5854 ± 2	0.3641 ± 1	-
1433	<i>hcp</i> -Gd + <i>bcc</i> -Zr	0.3656 ± 1	0.5854 ± 2	0.3641 ± 1	-
1483	<i>bcc</i> -Gd + <i>bcc</i> -Zr	0.4056 ± 1	-	0.3648 ± 1	-
1493	<i>bcc</i> -Gd + <i>bcc</i> -Zr	0.4059 ± 1	-	0.3650 ± 1	-

The lattice parameter a_0 of the bcc -Zr(Gd) phase as a function of temperature is shown in Fig. 4.5. The temperature dependence of the lattice parameter of pure bcc -Zr is, in addition, presented as extrapolated from the experimental values reported in the literatures [82,83]. The lattice parameter of bcc -Zr(Gd) phase increases much stronger, and this is related to the solid solubility of the larger Gd atoms. The experimental points of the Gd-Zr phase diagram can be determined by using the data of the temperature dependence of the maximum position q_1 of the liquid phase as well as the lattice parameter of bcc -Zr(Gd). The composition dependence according to Fig. 4.4 allows to calculate the Zr-content x_{Zr} of the Gd(Zr) liquid at a given temperature from the experimental data $q_1(T)$ in nm^{-1} :

$$x_{Zr}^{Liquid}(T) = \frac{q_1(T) - 21.18}{0.031}, \quad (4.2)$$

which holds true for the values of the liquid diffraction maximum in the two phase region $L + bcc$ -Zr(Gd) shown in Fig. 4.3. The liquidus line of the Gd-Zr phase diagram then can be represented by the results of the calculation as shown in Fig. 4.6a. The eutectic composition is estimated at 18 ± 2 at.% Zr for the Gd-Zr system from the temperature

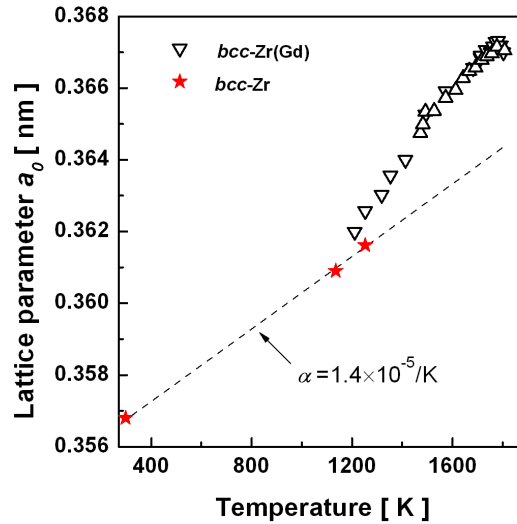


Figure 4.5: Temperature dependence of the lattice parameter a_0 of bcc -Zr(Gd) (inverted triangle). The deviation from the values of pure bcc -Zr (star) [77,84] represented by the dashed line is due to dissolution of Gd. The size of the symbols corresponds to the error bars.

dependence of the Zr content $x_{Zr}(T)$. The data of the liquidus line reported in the literature [72], which are different from the results of this work, are also shown.

Similar to the liquid phase the lattice parameters $a_{bcc-Zr(Gd)}$ as a function of temperature shown in Fig. 4.5 also allow to determine the solubility of Gd in the bcc -Zr phase. According to Vegard's rule for a solid solution between bcc -Gd and bcc -Zr, the Gd concentration (in at.%) in the bcc -Zr phase can be given by:

$$x_{Gd}(T) = \frac{a_{bcc-Zr(Gd)}(T) - a_{bcc-Zr}(T)}{a_{bcc-Gd} - a_{bcc-Zr}} \times 100, \quad (4.3)$$

An extrapolation of the data given in the literatures [82,83], presented also in Fig. 4.4, approximates the temperature dependence of the lattice parameter of the bcc -Zr phase, $a_{bcc-zr}(T)$. For the lattice parameter difference $\Delta a = a_{bcc-Gd} - a_{bcc-Zr}$ of the pure bcc -phases a constant value $\Delta a = 0.047$ nm is taken from the difference of the room temperature values $a_{bcc-Zr} = 0.3586$ nm [86] and $a_{bcc-Gd} = 0.405$ nm [87] under the assumption that the influence of slightly different thermal expansion coefficients can be neglected. Analogously, the lattice parameter $a_{bcc-Gd}(Zr)$ estimates the Zr content in the bcc -Gd(Zr) phase :

$$x_{Zr}(T) = \frac{a_{bcc-Gd(Zr)} - a_{bcc-Gd}}{a_{bcc-Zr} - a_{bcc-Gd}} \times 100, \quad (4.4)$$

where, a value of $a_{bcc-Gd} = 0.4096$ nm at $T = 1500$ K is used, which is obtained by an extrapolation from the value of bcc -Gd ($a = 0.405$ nm [87]) at room temperature together with the thermal expansion coefficient of Gd $\alpha = 9.4 \times 10^{-6}/K$. Dissolved Zr in the bcc -Gd(Zr) phase reduced the value of lattice parameter (see Table. 4.2). For the bcc -Gd(Zr) and bcc -Zr(Gd) phases the calculated compositions are plotted as the corresponding data points in the phase diagram shown in Fig. 4.6. The maximum solubility of 6.4 ± 1 at.% Gd in bcc -Zr(Gd) at $T = 1700$ K and of 7.9 ± 1 at.% Zr in bcc -Gd(Zr) at $T = 1500$ K are obtained from the diffraction data. The results of phase composition and transformation temperatures as determined by the DSC measurements, *in situ* XRD, and those of the microstructure analysis discussed in the following section, are also comprised in Fig. 4.6. The experimental data reported in Ref. [72] are slightly different from the results of this

work with respect to the liquidus line, but nevertheless it is in a good agreement for the solubility within the solid phases.

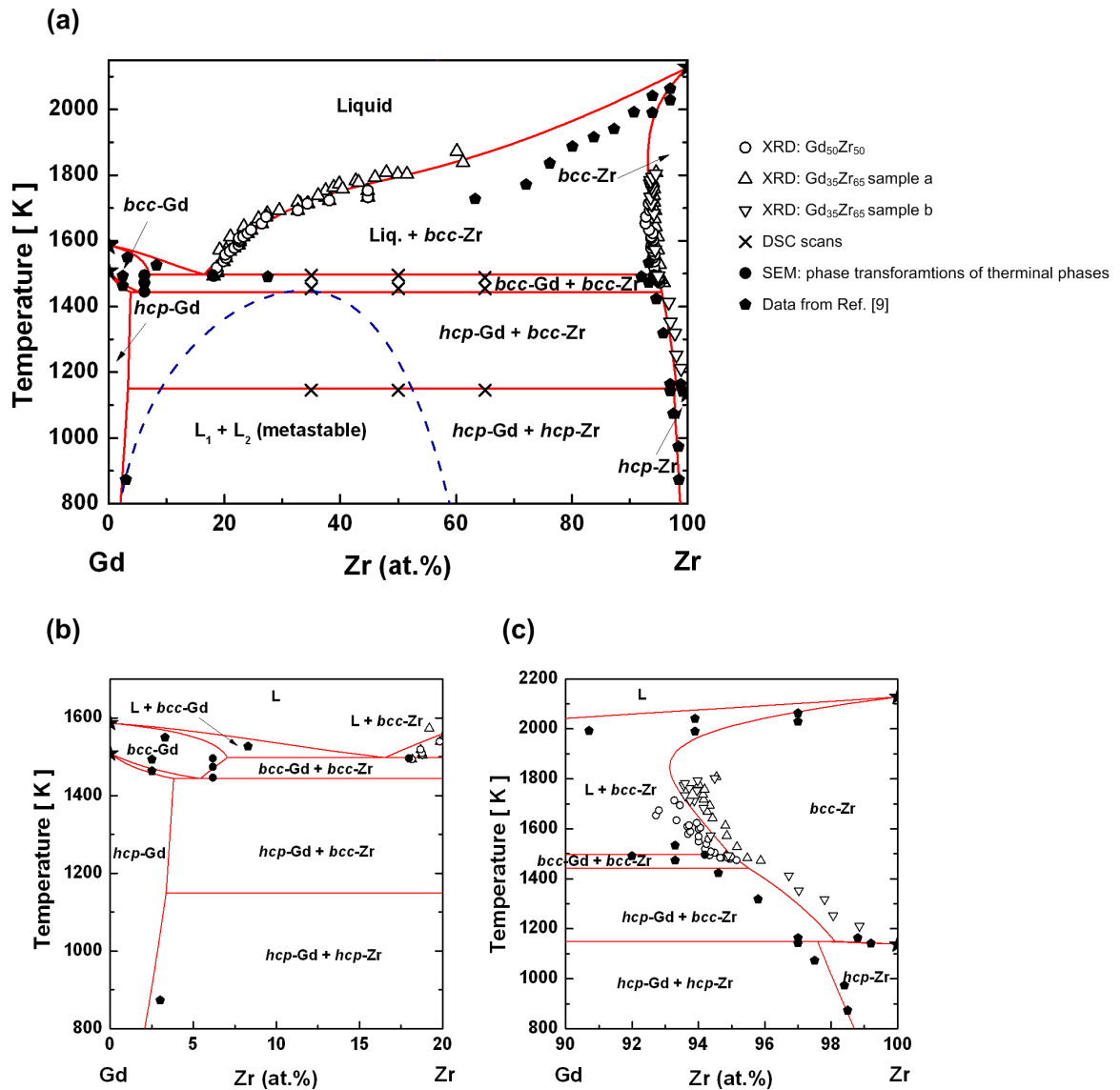


Figure 4.6: (a) Gd-Zr phase diagram determined by *in situ* XRD, DSC measurements and microstructure analysis (SEM). Phase diagram data from the literatures are also given [81,85]. Calculation using thermodynamic description of this work is represented by the lines.

4.1.1.2 Microstructure of as-solidified Gd-Zr alloys

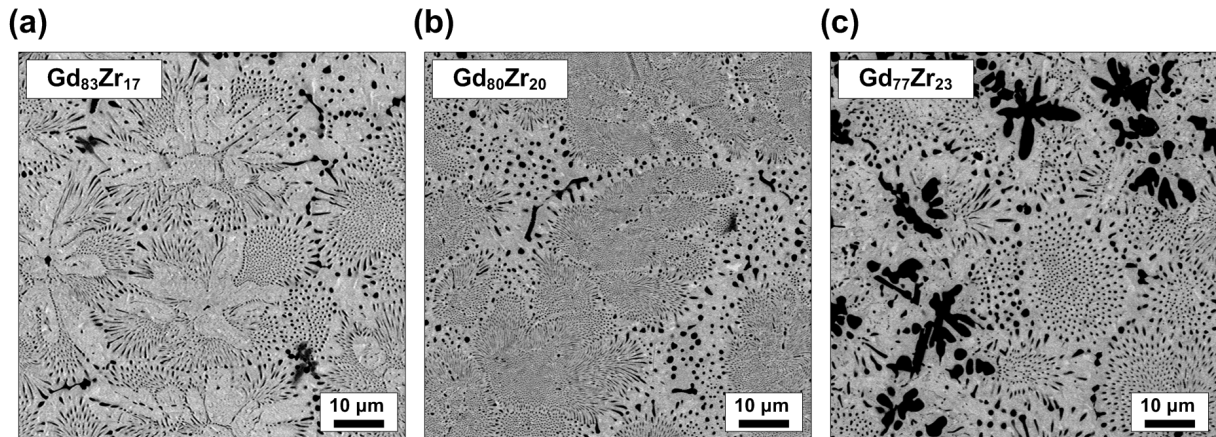


Figure 4.7: SEM images of cast Gd-Zr alloys in the vicinity of the eutectic composition. Morphologies of (a) Gd dendrites (gray) and Gd-Zr eutectic, (b) mainly Gd-Zr eutectic together with isolated Zr dendrites (black) and (c) Zr dendrites (black) and Gd-Zr eutectic are visible.

Unlike in previous studies [23,72,73,74,75], composition of 18 ± 2 at% Zr is determined for the eutectic composition by analysis of the X-ray diffraction data. In order to confirm this new result, investigations on the microstructure were additionally carried out. Fig. 4.7 shows microstructures of the cast Gd-Zr alloys near to the eutectic composition estimated from the X-ray diffraction results. The composition dependence of solidification modes is clearly revealed in the microstructure comparison, i.e. the formation of the Gd dendrites for the $\text{Gd}_{83}\text{Zr}_{17}$ (Fig. 4.7a) and that of the Zr dendrites for the $\text{Gd}_{77}\text{Zr}_{23}$ (Fig. 4.7c) as the primary crystallization. For the $\text{Gd}_{80}\text{Zr}_{20}$ (Fig. 4.7b), some isolated Zr dendrites still can be observed, but nevertheless the eutectic morphology of Gd-Zr is dominant. The eutectic composition is therefore expected between 17 and 20 at.% Zr. The chemical characterizations (EDX) on sections of the eutectic cells ($10 \mu\text{m} \times 10 \mu\text{m}$ by averaging) approximate the eutectic composition of 18.2 ± 0.5 at.% Zr which is in good agreement with the *in situ* XRD results. Table 4.3 summarizes the chemical compositions of the dendrites and those of the eutectic cells. The obtained value of the eutectic composition is clearly different despite the determined terminal solubility of the primary solid phases found to be within the error limits of the values reported in the literatures [62,75,76,77]. Experimental and thermodynamic assessment of the binary Gd-Zr system has been performed by combining *in situ* high-energy X-ray diffraction with electrostatic

levitation technique. The phase equilibria at high temperature, i.e. the coexistence of high temperature phases and the thermodynamic properties of the liquid phase could be successfully determined. Especially, a finite range of coexistence of *bcc*-Gd + *bcc*-Zr was detected unknown from previous assessments [23,72,73,74,75]. Based on the experimental results, a new thermodynamic description and improved Gd-Zr phase diagram were developed.

Table 4.3: Chemical compositions (at.%) of the eutectic of Gd-Zr and primary dendrites as determined by EDX analysis.

Nominal composition	Chemical analysis	Gd-dendrite	Zr-dendrite	Eutectic
Gd ₈₃ Zr ₁₇	Gd _{83.1} Zr _{16.9}	Gd _{93.8} Zr _{6.2}	-	
Gd ₈₀ Zr ₂₀	Gd _{80.2} Zr _{19.8}	-	-	Gd _{81.6} Zr _{18.4}
Gd ₇₇ Zr ₂₃	Gd _{76.8} Zr _{23.2}	-	Gd _{5.8} Zr _{94.2}	Gd _{82.0} Zr _{18.0}

4.1.2 The binary Gd-Ti system

Based on the experimental assessments of the Gd-Ti system reported by Croenu *et al.* [88] and Savitskii [89], Murray has redrawn the phase diagram with a prediction of a miscibility gap in the liquid state (a stable miscibility gap) [90], and it is also cited by Massalski [23] as shown with solid lines in Fig. 4.8. Recently, a modified Gd-Ti phase diagram with a much wider miscibility gap (dashed line in Fig. 4.8) was reported by Schmitz *et al.* [75]. They determined the critical temperature of about 1580 °C at Gd₂₀Ti₈₀ by means of electromagnetic levitation experiments. Since all the previous reports exhibit conflicts in the experimental data and suffer from the uncertainties of thermodynamic data especially for the phase equilibria at high temperature with the liquid phase. As suggested by Okamoto [91], the binary Gd-Ti system is therefore reinvestigated within the same framework and motivation of the Gd-Zr system. The *in situ* high energy X-ray diffraction at elevated temperatures combined with container-less electrostatic levitation (ESL) technique was again performed to obtain reliable experimental data on the liquid state.

For *in situ* X-ray diffraction investigations, alloy ingots of 200 mg mass with nominal compositions Gd₃₀Ti₇₀, Gd₄₀Ti₆₀ and Gd₆₀Ti₄₀ were prepared by arc-melting. The sizes of the spherical shaped ingots were about 4 mm in diameter which is sufficient for the electro static levitation (ESL) technique. The difference in sample mass after arc-melting

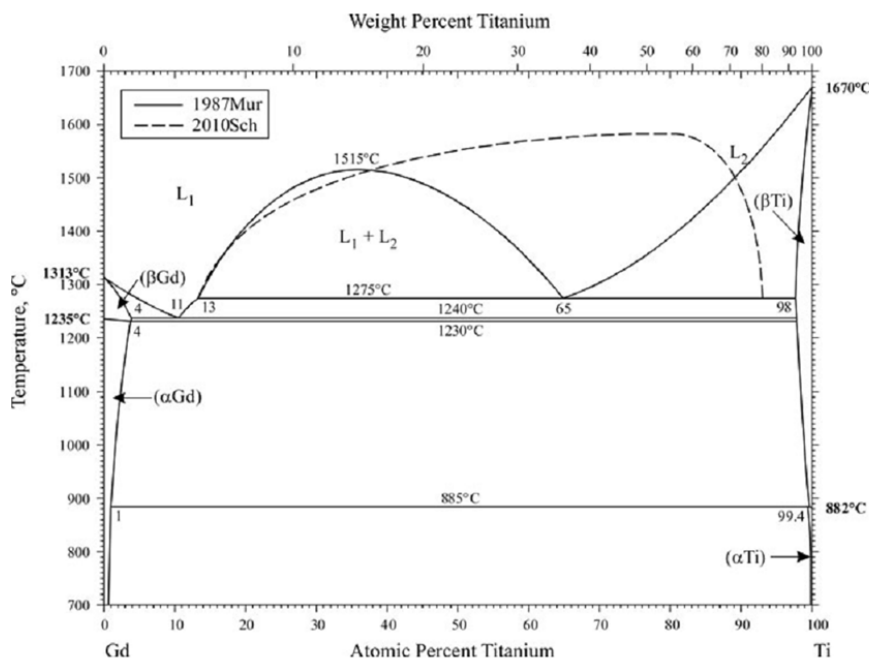


Figure 4.8: Gd-Ti phase diagram adopted from Ref. [91]. A modified miscibility gap reported by Schmitz *et al.* is also given for comparison [75].

was less than 0.1%. For more details of the experimental setup, see the section of X-ray diffraction in chapter 3. In order to investigate the microstructure, the sessile drop experiment was applied. For this, alloy ingots of 800 mg in mass with nominal compositions $\text{Gd}_{40}\text{Ti}_{60}$, $\text{Gd}_{60}\text{Ti}_{40}$ and $\text{Gd}_{70}\text{Ti}_{30}$ were additionally prepared by arc-melting. The sessile drop investigations were carried out using the experimental setup described in details elsewhere [92]. The samples were heated up to 2073 K with heating rate of 6 K/min, and then solidified either by fast cooling rate of 200 - 300 K/min by switching off the heater or by a controlled slow cooling rate. The arc-melted samples were prepared from proper quantities of pure Gd and Ti (Alfa Aesar 99.99 wt.% purity) under an argon atmosphere with a Ti getter.

4.1.2.1 *In situ* observation of phase equilibria at elevated temperatures

The DTA scans of different Gd-Ti alloys up to 1950 K shown in Fig. 4.9 indicate the occurrence of four phase transformations upon heating. In the curves of cooling cycle, the solidification and the *bcc* - *hcp* transformation of Gd are barely distinguishable due to

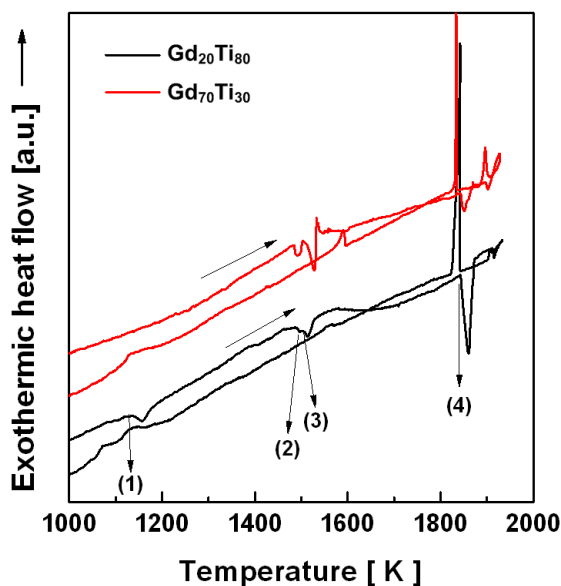


Figure 4.9: DTA scans of $\text{Gd}_{20}\text{Ti}_{80}$ and $\text{Gd}_{70}\text{Ti}_{30}$ (10 K/min) up to 1900 K; heating and cooling curves are shown.

incomplete reaction of the melt with the zirconia crucible despite the reaction (4) at the highest temperature is still visible.

As already proved in the section of the Gd-Zr system above, the corresponding phase transformations can be determined unambiguously by the *in situ* XRD patterns. Fig. 4.10 shows the intensity map of a series of simultaneously recorded diffraction patterns $I(q)$ of a $\text{Gd}_{30}\text{Ti}_{70}$ sample with corresponding temperature profile as a function of time during levitation experiment. According to the characteristic diffraction peak positions, the phases and the coexistence temperature ranges within the temperature interval about $T = 1250 \text{ K} - 1700 \text{ K}$ are indicated. One can clearly distinguish sequences of coexistence, i.e. the ranges of *hcp*-Gd + *bcc*-Ti, *bcc*-Gd + *bcc*-Ti and *L* + *bcc*-Ti.

The selected XRD patterns $I(q)$ at elevated temperatures in Fig. 4.11 represent the phase equilibria of a $\text{Gd}_{40}\text{Ti}_{60}$ sample between $T = 1460 \text{ K}$ and 1900 K . The different coexistence ranges of phases as a function of temperature can be determined in more detail by the whole set of recorded XRD patterns together with the onset temperatures of the DTA curves. At the temperature below $T = 1140 \text{ K}$, *hcp*-Gd(Ti) and *hcp*-Ti(Gd) phases coexist. Reactions (1) and (2) of the DTA result (Fig. 4.9) correspond to the phase transitions of the terminal solid phases. The reaction (1) of the DTA curve at $T = 1140 \text{ K}$ corresponds to the peritectoid transformation $\text{hcp-Ti(Gd)} \leftrightarrow \text{bcc-Ti(Gd)} + \text{hcp-Gd}$ which is in accordance with the former reports [23,75,88,89,90]. The coexistence of *hcp*-Gd(Ti) and

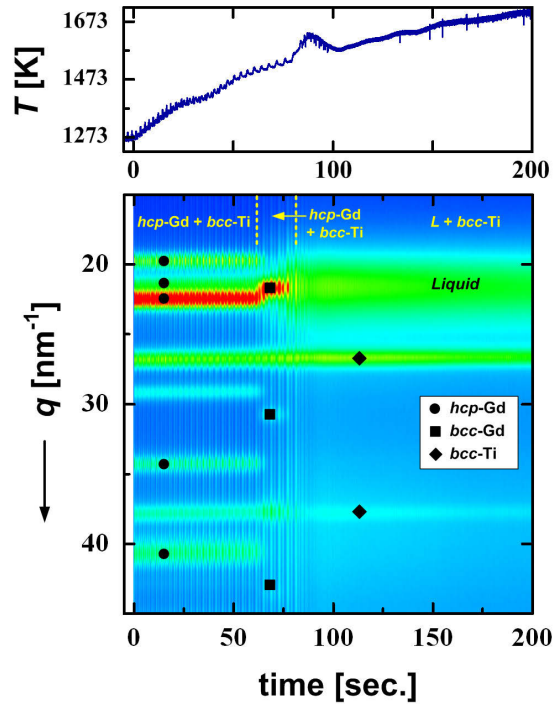


Figure 4.10: Temperature profile (uncorrected pyrometer data) versus time and intensity map of XRD patterns $I(q)$ for $Gd_{30}Ti_{70}$. The patterns were recorded each for 0.5 s.

$bcc-Ti(Gd)$ phases are observed between $1150\text{ K} < T < 1480\text{ K}$. The eutectoid transformation $hcp-Gd(Ti) + bcc-Ti(Gd) \leftrightarrow bcc-Gd(Ti)$ is then observed, which is related to the reaction (2) at $T = 1488\text{ K}$ of the DTA result. The coexistence of $bcc-Gd(Ti)$ and $bcc-Ti(Gd)$ phases is revealed from the XRD patterns for a short temperature interval $1490\text{ K} \leq T \leq 1505\text{ K}$. The eutectic reaction $bcc-Ti(Gd) + bcc-Gd(Ti) \leftrightarrow L$ is responsible for the melting of $bcc-Gd(Ti)$ phase, which is related to the reaction (3) of the DTA curve at $T = 1508\text{ K}$. This partial melting of the sample is represented by the demising of $bcc-Gd(Ti)$ reflections followed by the occurrence of a diffuse diffraction maximum in the XRD-patterns. In a wide temperature range from 1520 K up to about 1850 K , the coexistence of the Gd-rich liquid L_2 and the $bcc-Ti(Gd)$ phase is clearly evident from the *in situ* XRD patterns. For the $Gd_{60}Ti_{40}$ alloy, the same phase sequences were also observed in the *in situ* XRD patterns as found for $Gd_{30}Ti_{70}$ (Fig. 4.10) and $Gd_{40}Ti_{60}$ (Fig. 4.11). The lever rule also holds true for the differences in the intensity ratios for the different alloy compositions related to volume fractions of the phases. Since the two Gd- and Ti-rich melts are significantly different in mass density, the decomposition in liquid state led the severe instabilities of the levitated sample in shape and position, and then the sample usually flew away. For this reason, unfortunately, only a limited number of XRD patterns could be

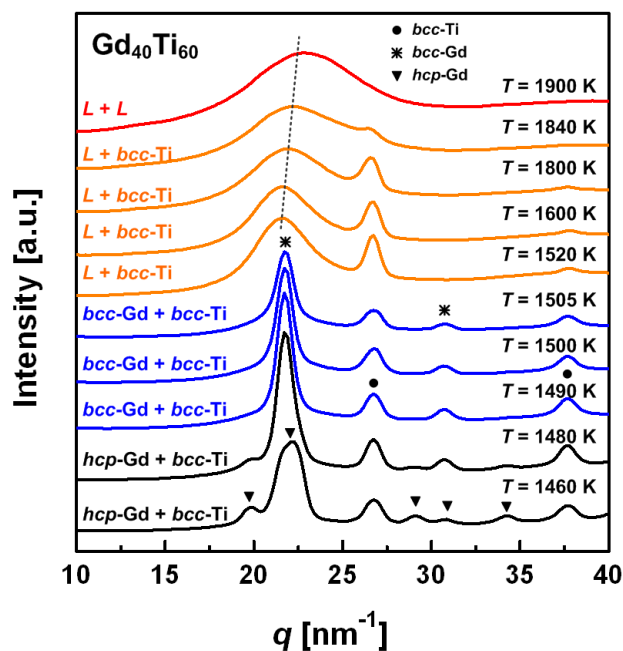


Figure 4.11: XRD of $Gd_{40}Ti_{60}$ at elevated temperatures. Characteristic temperature range of phase coexistence and phase transitions is presented. Characteristic diffraction peaks of the solid phases are marked.

obtained for a higher temperature regime $T > 1840$ K. For one sample of $Gd_{40}Ti_{60}$ alloy, the disappearance of the $bcc-Ti(Gd)$ phase reflections and simultaneous large shift of the position of the diffuse maximum were observed for a higher temperature $T > 1840$ K (Fig. 4.11). This behavior reveals the occurrence of the monotectic reaction $L_1 \leftrightarrow L_2 + bcc-Ti(Gd)$ which corresponds to the reaction (4) of the DTA curve at $T = 1841$ K. Since Gd atoms scatter incident X-rays about 10 times stronger than Ti atoms, the intensity contribution of the Ti-rich liquid L_1 is small and cannot be resolved even for the Ti-rich alloys. Nevertheless, the shift of the maximum positions in Fig. 4.11 (indicated by dashed line) can only be explained by the composition change in the Gd-rich liquid L_2 with temperature according to liquidus line and for $T \geq 1840$ K along the binodal line. The phase separation of the liquid phase also induces a broadening of the diffuse diffraction maximum with an asymmetry at the higher q side at $T \geq 1850$ K. The invariant reactions of the Gd-Ti systems as derived from the *in situ* XRD and DTA analysis are summarized in Table 4.4.

Fig. 4.12a compares two diffraction patterns of $Gd_{40}Ti_{60}$ obtained below and above the monotectic temperature. The distinct shift of the maximum position towards a higher q -

value and a broadening of the diffuse maximum are the clear indication for the occurrence of phase separation at about $T = 1900$ K. Fig 4.12b shows the diffraction patterns for $Gd_{30}Ti_{70}$ obtained below and just above the monotectic reaction which was the possible highest temperature before the lost of the samples. As can be clearly indicated, the shape change of the diffuse maximum induced by a phase separation is much more pronounced in $Gd_{30}Ti_{70}$ due to the stronger intensity contribution of the Ti-rich liquids compared to $Gd_{60}Ti_{40}$ alloy. As shown Fig. 4.12b, two characteristic XRD patterns (circles) were approximated by a sum of Lorentzian peak functions (solid lines). The approximation on $T = 1850$ K represents a superposition of two diffuse peaks originating from the two liquids $L_1 + L_2$ with a small fraction of bcc-Ti solid phase.

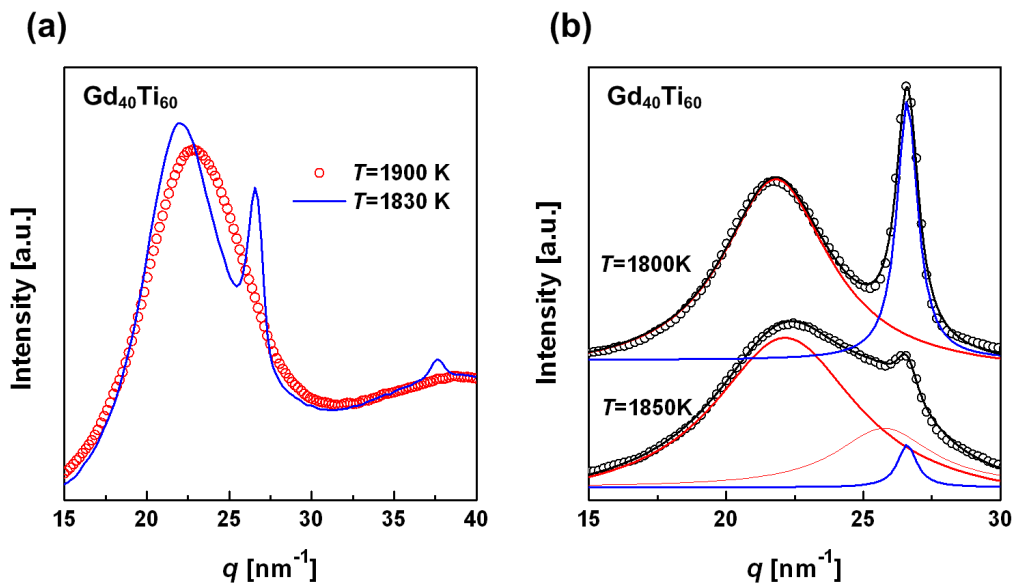


Figure 4.12: XRD patterns of Gd-Ti alloys below and above the monotectic temperature.

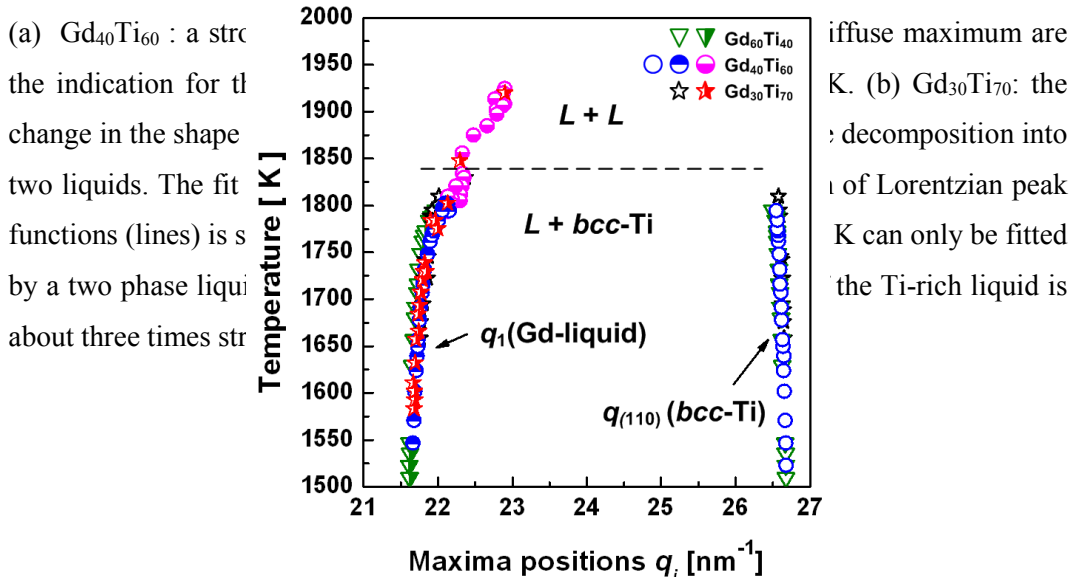


Figure 4.13: Maximum positions q_1 of the Gd(Ti) liquid, and $q_{(110)}$ of *bcc*-Ti versus T . data are from measurements of different Gd-Ti alloys

Fig. 4.13 shows in detail the temperature dependence of the position of the diffuse maximum q_1 for Gd-rich liquid phase L_2 , as well as the position of the (110)-reflection of the *bcc*-Ti(Gd) phase $q_{(110)}$. The presented data are obtained from independent measurements of the three Gd-Ti alloys with different compositions. The obtained data have a good reproducibility within some scattering of $\Delta q = 0.1 \pm 0.1 \text{ nm}^{-1}$, which defines the accuracy of the experiment. The maximum position q_1 of the Gd-rich liquid exhibits a shifting to larger q -values, which is related to increase of Ti solubility in the liquid at higher temperatures. In contrast, the position of $q_{(110)}$ slight shifts to lower q -values, which reflects mainly the thermal lattice expansion of the *bcc*-Ti(Gd) phase with temperature. According to the Ehrenfest equation (eq. 4.1), the position of the first diffuse maximum q_1 approximately scales with an interatomic distance d of the alloy [78]. The change in q_1 nevertheless can be often well described by a linear dependence on the concentration c_i of the added element within an element substitution series [79,80,93]. An increased solubility of Ti ($d_{\text{Ti}} = 0.292 \text{ nm}$) in the Gd-rich liquid ($d_{\text{Gd}} = 0.362 \text{ nm}$) reduces the interatomic distance resulting in the shifting of the maximum position q_1 to larger q -values with rising temperature. The thermal expansion of the liquid Gd-rich liquid is neglected here because the effect on the position q_1 is one order of magnitude smaller but within the error bars of q_1 determination. The available positions of XRD diffraction maxima for liquid Zr [81], Ti [94] and Gd-Zr (shown in previous section: chapter 4.1) obtained from experiments are compared in Fig. 4.14 with the calculation by Eq. 4.1 ($k = 1.22$). The comparison shows a good agreement between calculation and experimental data for the Gd-Zr liquids, as well as the value of q_1 for pure Ti compared to the experimental one. Since Zr and Ti have similarity in chemical properties, Eq. 4.1 is also applicable to the Gd-Ti liquid. A linear fit of the data within Gd-rich side ($0 \leq x \leq 30 \text{ at.\% Ti}$) gives

$$q_1(x) = 21.28 + 0.0424x, \quad (4.5)$$

Then, the chemical composition of the Gd(Ti) liquid as a function temperature can be determined by applying the maximum position q_1 of the liquid phase (presented in Fig. 4.13) to Eq. 4.5. The Ti content x_{Ti} is calculated from the experimental data $q_1(T)$ with q_1 in nm^{-1} and x_{Ti} in at. %:

$$x_{Ti}^{liquid} = \frac{q_1(T) - 21.28}{0.0424}, \quad (4.6)$$

As shown in Fig. 4.15, the calculations with the values of the liquid diffraction maximum q_1 in the two phase regime $L + bcc\text{-Ti(Gd)}$ represent the liquidus line of the Gd-Ti phase diagram. The liquidus line varies from about 92 ± 2 at.% Gd for $T = 1500$ K up to about 80 ± 2 at.% Gd for $T = 1800$ K. Unusual steepness of the liquidus line inferred from that the position of maxima q_1 is related to the weak change of the diffraction intensities between Gd-rich liquid phase L_2 and $bcc\text{-Ti(Gd)}$ phase up to $T = 1800$ K as shown in Fig. 4.11. Although the determination of the maxima position showed a good accuracy with a small error of $\pm 0.1 \text{ nm}^{-1}$, nevertheless an error of ± 2 at.% follows for the calculated chemical composition of the Gd-rich liquid. For temperatures $T > 1841$ K, the shift of the maximum position and the derived liquid composition correspond to the Gd-rich part of the binodal line of the miscibility gap.

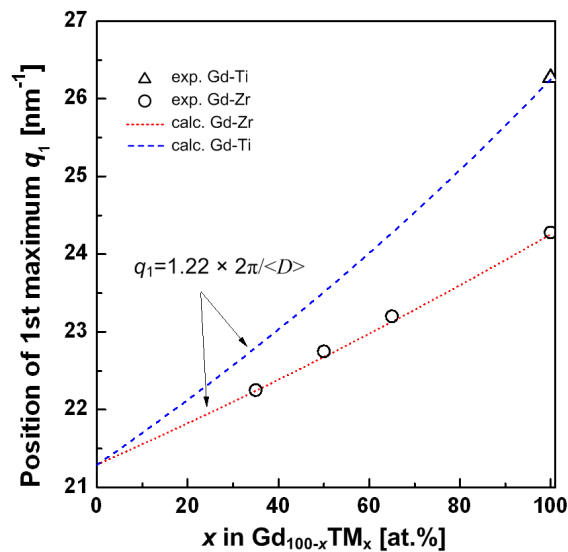


Figure 4.14: Position of the 1st diffuse diffraction maximum of Gd-TM liquids (TM = Ti, Zr). Experimental data from [81,94] are given by symbols. Calculations based on the Ehrenfest equation [78] are shown by the lines.

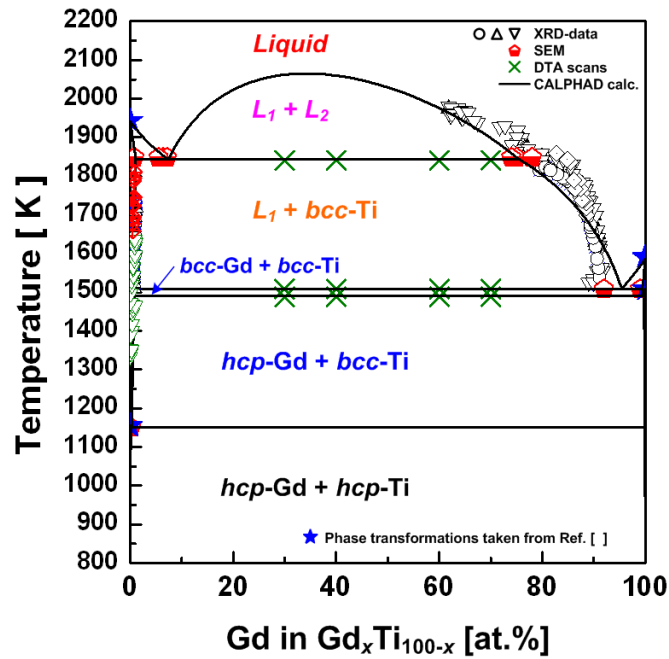


Figure 4.15: Experimentally assessed Gd-Ti phase diagram. Lines represent the CALPHAD calculation of Ref. [143].

The analysis of the lattice parameter $a_{bcc-Ti(Gd)}$ as a function of temperature shown in Fig. 4.16 estimates the solubility of Gd in the $bcc-Ti(Gd)$ phase. By applying Vegard's rule for a solid solution phase the Gd concentration (in at.%) in the $bcc-Ti(Gd)$ phase is given by

$$x_{Gd}(T) = \frac{a_{bcc-Ti(Gd)}(T) - a_{bcc-Ti}(T)}{a_{bcc-Gd} - a_{bcc-Ti}} \times 100, \quad (4.7)$$

An extrapolation of the literature data given in Refs. [82,95] (also presented in Fig. 4.16) can approximate the temperature dependence of the lattice parameter of the pure $bcc-Ti$ phase, $a_{bcc-Ti}(T)$. Under the assumption that the influence of slightly different thermal expansion coefficients of pure bcc phases are negligible, a constant value $\Delta a = a_{bcc-Gd} - a_{bcc-Ti} = 0.0775$ nm is derived from the room temperature values $a_{bcc-Ti} = 0.3275$ nm [95] and $a_{bcc-Gd} = 0.405$ nm [87]. The lattice parameters of $bcc-Ti(Gd)$ phase exhibit only slight increase, which is in accordance with a very low solubility of Gd atoms. About 0.6 ± 0.3 at.% Gd at $T = 1800$ K is concluded as the Gd content in $bcc-Ti(Gd)$ phase from the lattice parameter.

Analogously, the Ti content in the bcc -Gd(Ti) phase can also be estimated from the lattice parameter $a_{bcc\text{-Gd(Ti)}}$:

$$x_{Ti}(T) = \frac{a_{bcc\text{-Gd(Ti)}}(T) - a_{bcc\text{-Gd}}(T)}{a_{bcc\text{-Ti}} - a_{bcc\text{-Gd}}} \times 100, \quad (4.8)$$

An extrapolation from the lattice parameter value of bcc -Gd ($a = 0.405$ nm [87]) at room temperature along with the thermal expansion coefficient of Gd ($\alpha = 9.4 \times 10^{-6}/\text{K}$) determined a value of $a_{bcc\text{-Gd}} = 0.4096$ nm at $T = 1500$ K. The dissolution of Ti results in the smaller value of the lattice parameter of the bcc -Gd(Ti) phase ($a_{bcc\text{-Gd(Ti)}} = 0.4092 \pm 0.0002$ nm). For $T = 1500$ K, the maximum solubilities of about 0.8 ± 0.3 at.% Ti in bcc -Gd(Ti) are obtained from the XRD diffraction data. The results of phase composition and transformation temperatures determined by *in situ* XRD, DTA measurements and microstructure analysis discussed in the following section are comprise in Fig. 4.15.

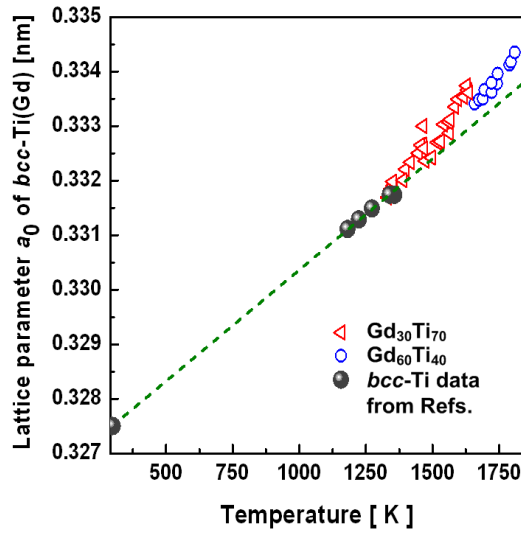


Figure 4.16: Temperature dependence of the lattice parameter a_0 of bcc -Ti(Gd). The deviation from the values of pure bcc -Ti (taken from Refs. [82,95]) represented by the dashed line is due to dissolution of Gd.

4.1.2.3 Microstructure of as-solidified Gd-Ti alloys

Fig. 4.17 shows the microstructures of half of cross section for the different Gd-Ti samples after the sessile drop experiment. The optically observed melting behavior of the Gd-Ti alloys during heating up to $T = 2073$ K have a good agreement with the *in situ* XRD measurements. In the sessile drop experiment the melting of the $\text{Gd}_{40}\text{Ti}_{60}$, $\text{Gd}_{60}\text{Ti}_{70}$ and $\text{Gd}_{70}\text{Ti}_{30}$ samples started at $T = 1495 \pm 20$ K and the completed at $T = 1870 \pm 50$ K.

The occurrence of the decomposition into two Gd- and Ti-rich liquids by a liquid-liquid phase separation $L \leftrightarrow L_1 + L_2$ can clearly be seen from microstructures. Since the Ti-rich liquid (dark) is lighter in mass density than Gd-rich liquid (light gray), the Ti-rich liquid is situated at the top of the droplet. As Gd content increased, one can also see that the volume fraction of Ti-rich liquid is reduced which is in accordance with the lever rule.

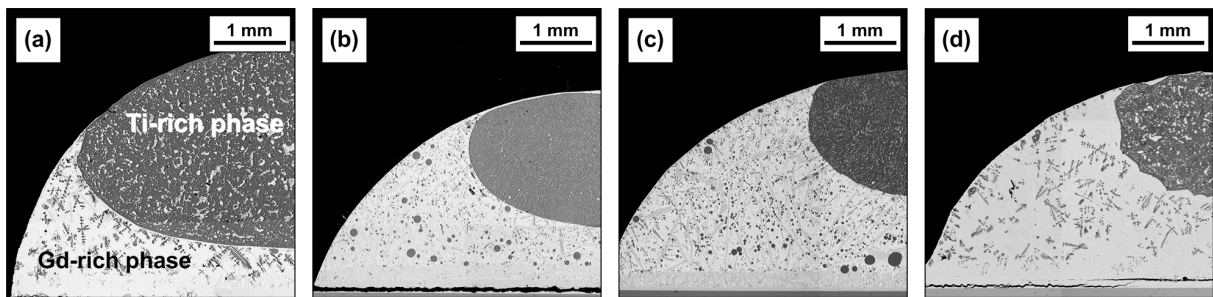


Figure 4.17: SEM images of the cross section of solidified Gd-Ti alloys after sessile drop melting up to 2073 K (a): $\text{Gd}_{60}\text{Ti}_{40}$ - slowly cooled, (b): $\text{Gd}_{40}\text{Ti}_{60}$ - fast cooled, (c): $\text{Gd}_{70}\text{Ti}_{30}$ - fast cooled, (d): $\text{Gd}_{70}\text{Ti}_{30}$ - slowly cooled. Occurrence of liquid-liquid phase separation is concluded from the coarse microstructure. The Ti-enriched liquid (dark region) is lifted up due to the buoyancy resulting from the density differences. Secondary phase reaction and decomposition occur within the two former liquids upon quenching.

The chemical compositions of the Gd- and Ti-rich regions were measured by EDX analysis over large areas of $500 \mu\text{m} \times 500 \mu\text{m}$. The measured values are summarized in Table 4.5 and are corresponding to the compositions of the two liquids at the monotectic temperature within the experimental errors. Although the microstructure of sessile droplets exhibit cooling rate dependence especially in their dendrites sizes, nevertheless the average chemical compositions of the areas representing the two liquids are identical. The Ti-rich liquid L_1 first starts to solidify into *bcc*-Ti phase below the monotectic temperature during cooling. Fig. 4.18a shows the enlarged SEM image from the solidified Ti-rich liquid L_1 region of the $\text{Gd}_{70}\text{Ti}_{30}$ alloy (shown in Fig. 4.17d). According to the XRD results, the corresponding sequence of phase formation is $L_1 \rightarrow \textit{bcc}\text{-Ti}(\text{Gd}) + L_2 \rightarrow \textit{bcc}\text{-Ti}(\text{Gd}) + \textit{bcc}\text{-Gd}(\text{Ti})$. The area analysis on corresponding regions of Fig. 4.18a (dark) determined the

solubility of 0.5 at.% Gd in *bcc*-Ti(Gd) phase. As temperature decreases further the *bcc*-Ti precipitates the Gd-phase at its grain boundaries (gray lines in Fig. 4.18a) due to the reduced solubility. A solubility of 0.2 at.% Gd in the *hcp*-Ti phase is obtained from the EDX point analysis. The white droplet in Fig. 4.18a (upper right corner) reveals the formation of the Gd-rich liquid L_2 by the monotectic reaction. The contrast variation within the white droplet is due to secondary Ti precipitation and the eutectic reaction within Gd-rich liquid L_2 upon further cooling.

The enlarged SEM image from the solidified Gd-rich liquid (bright region of Fig. 4.17d) is also given in Fig. 4.18b. The microstructure consists of Ti-dendrites (black) and Gd-Ti eutectic microstructure. According to the XRD results, the corresponding sequence

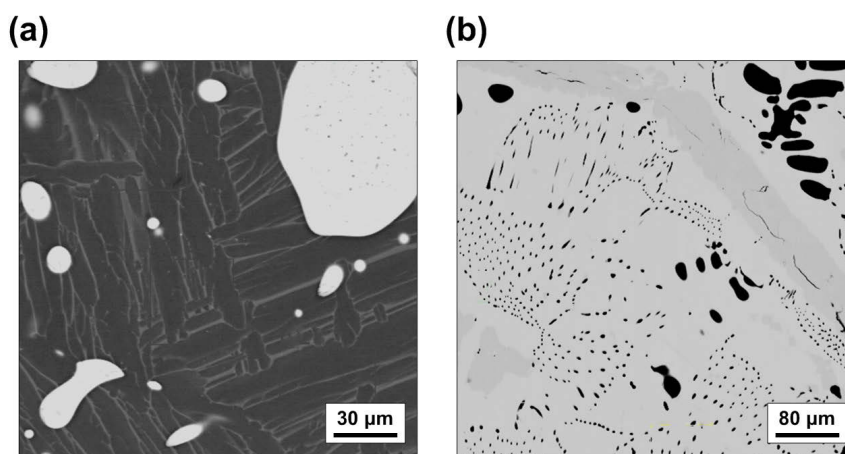


Figure 4.18: Magnified SEM images of solidified Ti-rich (a) and Gd-rich (b) liquids of $Gd_{70}Ti_{30}$. (a): Ti-dendrites (black) with Gd precipitation at the grain boundary (gray lines) and solidified entrapped Gd-droplets (white) are visible. (b): Ti-dendrites (black) and (Gd + Ti) eutectic microstructure are visible.

of phase formation is $L_2 \rightarrow bcc\text{-Ti(Gd)} + L_2 \rightarrow bcc\text{-Ti(Gd)} + bcc\text{-Gd(Ti)}$. Gd-dendrites (gray) are also formed probably due to undercooling of the Gd-rich melt. From the EDX analysis of the corresponding Gd-Ti two-phase regions a value of 92 ± 3 at.% Gd is concluded as the eutectic composition. In the *hcp*-Ti(Gd) dendrites about 0.2 at.% Gd is found to be dissolved. On the other hand, about 0.5 at.% Ti is dissolved in *hcp*-Gd(Ti) dendrites. The values obtained from SEM/EDX experiments are summarized in Table 4.5 and also presented in Fig. 4.15.

The composition of the eutectic reaction $L \leftrightarrow bcc\text{-Gd(Ti)} + bcc\text{-Ti(Gd)}$ determined by SEM/EDX analysis for different Gd-Ti alloys exhibit some scatter ranging from 89 to 95 at.% Gd (see Table 4.4 for the average values). The liquidus line as the first

approximation can be calculated by Eq. 4.7. Since no experimental data for the Gd-rich liquid are available to prove some additional systematic deviations that probably responsible for the discrepancies with the calculated phase diagram, cannot be ruled out. Taking the experimental error into account especially for the liquidus line, the calculation result of this work is in a good agreement with the experimental data. The phase equilibria of the binary Gd-Ti system has been successfully investigated again by combining *in situ* high-energy X-ray diffraction with ESL technique. In particular, an extended range of coexistence of *bcc*-Ti and Gd-rich liquid L_2 phase up to $T = 1840$ K was detected which has been unknown from previous assessments in Refs. [23,88,89,90,96]. Based on the experimental results, a consistent thermodynamic description was developed and an improved new Gd-Ti phase diagram could be introduced.

Table 4.5: Chemical compositions of phases determined by SEM/EDX analysis.

Alloys	e_1		e_2		
	L_1 : Gd (at.%)	L_2 : Gd (at.%)	L : Gd (at%)	Gd: Ti (at%)	Ti : Gd (at%)
Gd ₄₀ Ti ₆₀	7.0 ± 2	78 ± 5	91.4 ± 3	0.2±0.1	0.4±0.1
Gd ₆₀ Ti ₄₀	5.5 ± 1	74 ± 5	-	0.2±0.1	0.5±0.1
Gd ₇₀ Ti ₃₀	6.1 ± 1	75 ± 5	92.3 ± 2	0.3±0.1	0.4±0.1

4.1.3. The ternary Gd-Ti-Co system

According to the phase diagram of Gd-Ti system discussed in previous section, the Gd-Ti system is of the monotectic type exhibiting a stable miscibility gap and corresponding liquid-liquid phase separation. Due to this, Gd-Ti-based multi-component systems (e.g. Gd-Ti-Co-Al system) are appropriate candidates for phase separated glass-glass or glass-crystalline composite materials [18]. The evolution of such unique microstructure of phase separated materials strongly depends on their thermodynamic properties and the quenching conditions [6,7,8,13,66,97]. Since there is no information about the ternary Gd-Ti-Co phase diagram in the literature, a systematic investigation of the phase diagram is required for a deeper understanding of how phase separation develops in Gd-Ti-Co-Al glass-forming alloys during solidification. Therefore, the ternary Gd-Ti-Co system not only as an extension of the binary Gd-Ti subsystem but also as a precedent study of Gd-Ti-Co-Al system, is investigated especially on the miscibility gap and liquid phases. Analogous to both Gd-Zr and Gd-Ti systems in previous sections, the liquid-solid

phase equilibria of the Gd-Ti-Co alloys was also investigated using *in situ* high-energy X-ray diffraction on levitated samples (containerless ESL technique), as well as the microstructure and thermal analysis.

4.1.3.1 *In situ* observation of phase equilibria at elevated temperatures

Fig. 4.19 shows the DSC traces for the $\text{Gd}_{50}\text{Ti}_{20}\text{Co}_{30}$ and $\text{Gd}_{35}\text{Ti}_{35}\text{Co}_{30}$ alloys up to $T = 1700$ K. As marked by solid arrows in Fig. 4.19, the heating curves indicate two phase

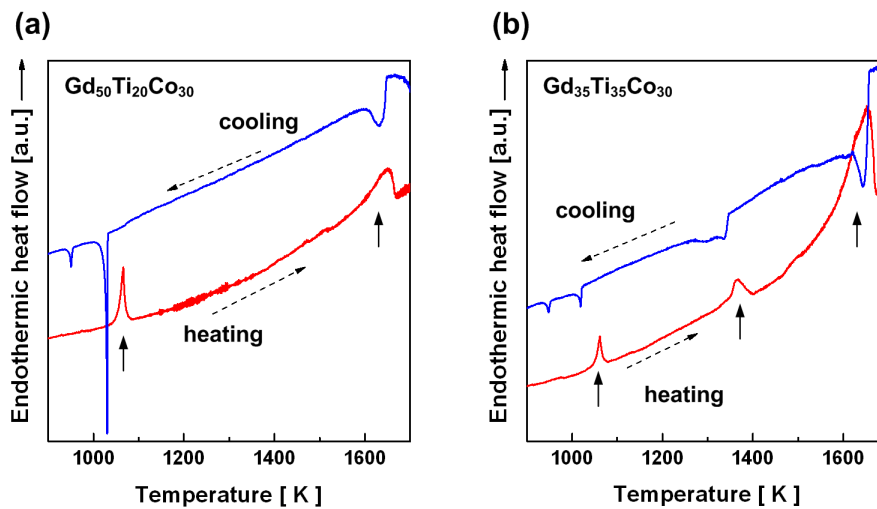


Fig. 4.19: DSC curves for (a) $\text{Gd}_{50}\text{Ti}_{20}\text{Co}_{30}$ and (b) $\text{Gd}_{35}\text{Ti}_{35}\text{Co}_{30}$ alloys up to about $T = 1700$ K. Heating and cooling curves are given.

transformations for the $\text{Gd}_{50}\text{Ti}_{20}\text{Co}_{30}$ (Fig 4.19a) and three phase transformations for the $\text{Gd}_{35}\text{Ti}_{35}\text{Co}_{30}$ (Fig 4.19b) by endothermic events. For both alloys, the cooling curves contains one more exothermic peak below $T = 1000$ K. The non-equilibrium state of as-quenched alloys might thus be the reason for the absence of the corresponding peak to the transformation event at about $T = 950$ K upon heating. Obviously, slight undercooling effect is also observed upon cooling. The corresponding phase reactions can be determined by the *in situ* XRD patterns. The characteristic phase equilibria of the $\text{Gd}_{50}\text{Ti}_{20}\text{Co}_{30}$ and $\text{Gd}_{35}\text{Ti}_{35}\text{Co}_{30}$ alloys are represented by the selected XRD patterns $I(q)$ at different temperatures as shown in Fig. 4.20. For the $\text{Gd}_{50}\text{Ti}_{20}\text{Co}_{30}$ alloy (Fig 4.20a), a semi-solid regime where the Gd-rich liquid (diffuse maximum at $q = 21.5 \text{ nm}^{-1}$) and the CoTi ($Pm-3m$) intermetallic phase [98] are coexisting, is evident from temperature between

1350 K < T < 1660 K. With increasing temperature up to $T = 1660$ K, the reflections of CoTi phase representing the volume fraction of the CoTi solid phase gradually demises. The reaction (1) in the DSC curve (Fig. 4.19a) corresponds to the transition (i) shown in Fig. 4.20a, which determines the liquidus temperature $T_{liq} = 1670 \pm 10$ K by complete disappearance of the CoTi reflections. The addition of Co to Gd-Ti system completely suppressed the allotropic transformation $hcp\text{-Gd} (P63/mmc) \leftrightarrow bcc\text{-Gd} (Im-3m)$. This is in good accordance with the literature for the binary Gd-Co system [99] that the reaction $L \leftrightarrow L + bcc\text{-Gd}$ becomes $L \leftrightarrow L + hcp\text{-Gd}$ with Co content more than about 2.5 at.%. Due to the composition change of the liquid phase by the dissolving of the CoTi phase, the

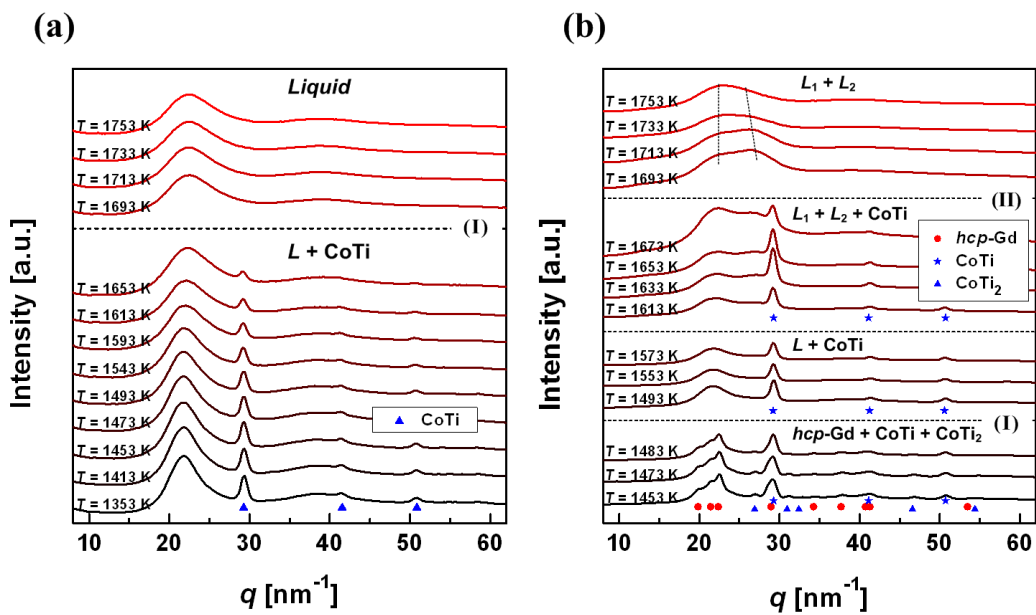


Fig 4.20 Selected XRD patterns for (a) $Gd_{50}Ti_{20}Co_{30}$ and (b) $Gd_{35}Ti_{35}Co_{30}$ alloys at elevated temperatures. The transition between temperature ranges of coexistence phases are indicated by horizontal dashed lines. Corresponding crystalline phases are indexed by symbols.

position of the first maximum q_1 for the liquid phase exhibits a gradual shift toward the larger q -values with temperature rising, and the value of $q = 22.4 \text{ nm}^{-1}$ is obtained for the XRD pattern at $T = 1753$ K.

For the $Gd_{35}Ti_{35}Co_{30}$ alloy (Fig. 4.20b), the sequences of phase formation observed from the *in situ* XRD patterns are more complex than that of the $Gd_{50}Ti_{20}Co_{30}$. The $hcp\text{-Gd}(\text{Co,Ti})$ phase coexists with CoTi and $CoTi_2 (Fd-3mZ)$ intermetallic compounds [100] below $T = 1485$ K. The DSC event (1) at $T = 1390$ K (Fig. 4.19b) corresponds to the

eutectic reaction $L \leftrightarrow hcp\text{-Gd} + \text{CoTi}_2$. The partial melting of the sample is indicated by the demising of $hcp\text{-Gd}$ and CoTi_2 reflections and the occurrence of a diffuse diffraction maximum in the XRD patterns above $T = 1490$ K, The XRD patterns. At the temperature range $1580 \text{ K} < T < 1680 \text{ K}$, the formation of a second liquid phase L_2 with a secondary diffuse maximum at about $q = 26.5 \text{ nm}^{-1}$ is observed. At this temperature range, two liquids coexist together with CoTi crystalline phase. The DSC event (2) in Fig. 4.19b is related to the melting of CoTi phase (ii) $L_2 \leftrightarrow \text{CoTi}$. From the XRD patterns above $T = 1690$ K, the coexistence of a Gd-rich and a Ti-rich liquid is clearly evident by two diffuse diffraction maxima at about $q = 21.5 \text{ nm}^{-1}$ for the Gd-rich liquid and at about $q = 26.5 \text{ nm}^{-1}$ for the Ti-rich liquid. This gives a direct evidence for the occurrence of liquid-liquid phase separation,

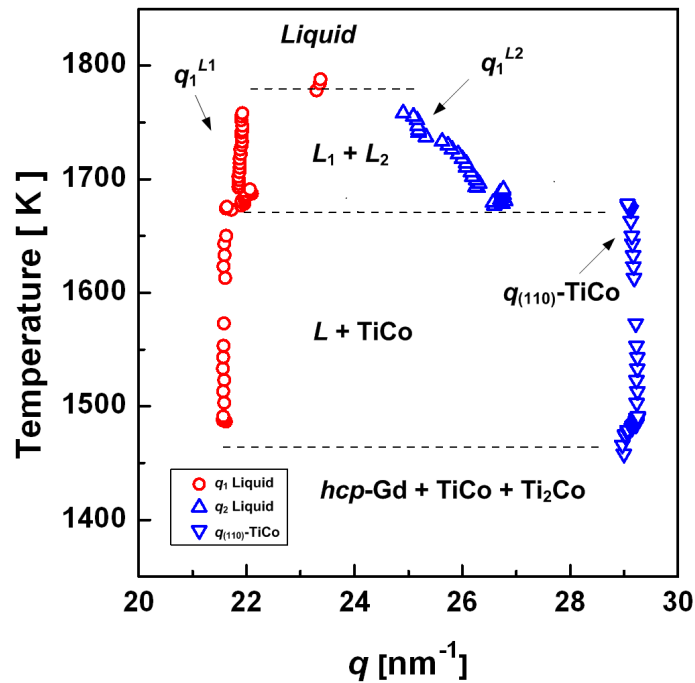


Figure 4.21: The positions of the first maxima of the Gd-rich (q_1^{Gd}) and Ti-rich (q_1^{Ti}) liquids as a function of temperature. The peak position of (110)-reflection of the CoTi intermetallic compound q_{110}^{CoTi} is also given. The data are summarized from the measurements of $\text{Gd}_{35}\text{Ti}_{35}\text{Co}_{30}$. The size of the symbols approximately corresponds to the error bars.

i.e. the Gd-Ti-Co alloy has a stable miscibility gap. With further heating up to $T = 1753$ K which was the possible highest temperature before lost of levitated sample, the positions of the diffuse maxima of both liquids systematically shift (dashed lines in Fig. 4.20b) due to the composition change along the binodal line.

Fig. 4.21 shows in detail the position of the diffuse maxima q_1^{Gd} of Gd-rich liquid, q_1^{Ti} of Ti-rich liquid and the peak position of the (110)-reflections q_{110}^{CoTi} of CoTi phase as a function of temperature. The data points are summarized from XRD patterns of $\text{Gd}_{35}\text{Ti}_{35}\text{Co}_{30}$ alloy. For the positions q_1^{Gd} and q_{110}^{CoTi} in the semi-solid regions ($L_1 + \text{CoTi}$ and $L_1 + L_2 + \text{CoTi}$) at the temperature range $1490 \text{ K} < T < 1680 \text{ K}$, only slight shift is observed. The maximum position q_1^{Gd} shifts from 21.57 nm^{-1} at $T = 1490 \text{ K}$ to 21.64 nm^{-1} at $T = 1680 \text{ K}$, and the peak position q_{110}^{CoTi} remains almost constant. This means that the solubility changes of the smaller Ti ($d_{\text{Ti}} = 0.280 \text{ nm}$) and Co ($d_{\text{Co}} = 0.270 \text{ nm}$) atoms in the Gd-rich liquid ($d_{\text{Gd}} = 0.362 \text{ nm}$), which changes the average interatomic distance resulting

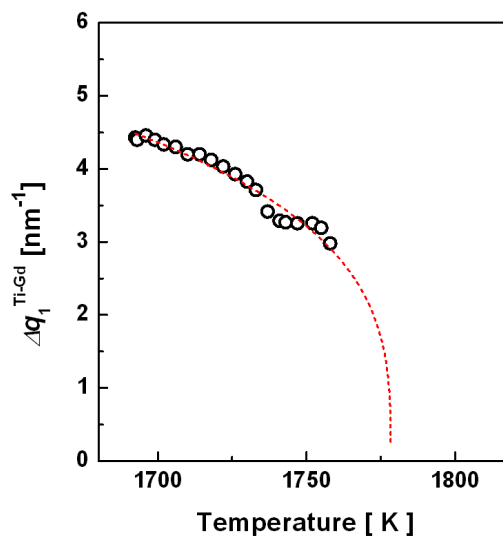


Figure 4.22: The position difference $\Delta q_1^{\text{Ti-Gd}}$ between the first maxima of the Gd-rich (q_1^{Gd}) and the Ti-rich (q_1^{Ti}) liquids for the $\text{Gd}_{35}\text{Ti}_{35}\text{Co}_{30}$ alloys a function of temperature. The solid line is fit to the experimental data (open circle): $\Delta q_1^{\text{Ti-Gd}} = q_0(1 - T / T_c) \text{ nm}^{-1}$. The size of the symbols corresponds to the error bars.

in the diffuse maximum position q_1^{Gd} , is very limited. Unfortunately, it was not possible to obtain reliable values for the maximum position q_1^{Ti} of Ti-rich liquid due to the complexity of the XRD patterns for the $L_1 + L_2 + \text{CoTi}$ regime. From the XRD patterns obtained from above $T = 1690 \text{ K}$ where two liquid phases present, one can clearly see that the maxima positions q_1^{Gd} and q_1^{Ti} exhibit convergence behavior with temperature. The maximum position q_1^{Ti} of Ti-rich liquid distinctly shifts to lower q -values whereas that of Gd-rich liquid q_1^{Gd} just slightly shifts to larger q -values with increasing temperature. This suggests that the Gd solubility change of the Ti-rich liquid with temperature is much more distinct than the Ti solubility change in Gd-rich liquid. Therefore, an approximation of the

asymmetric miscibility gap biased to the Gd-rich liquid side in the pseudo-binary section of the ternary phase diagram $\text{Gd}_{70}\text{Co}_{30}\text{-Ti}_{70}\text{Co}_{30}$ can be concluded from temperature dependences of q_1^{Gd} and q_1^{Ti} .

As the compositions of two liquids converge with temperature increasing within the miscibility gap, the density difference between the coexistent two liquids $\Delta\rho^{L_1-L_2}$ becomes smaller, and it finally vanishes when the critical temperature T_c of the miscibility gap is attained. Recently, Kaban *et al.* [101] reported that the power law with a critical-point exponent $\beta = 0.30 \pm 0.02$ which is close to the value of renormalized theory [102,103] can describe the temperature dependence of the density difference for many immiscible metallic alloys. Since the first maximum position q_1 corresponds to the density in the liquid phase, the critical temperature T_c in pseudo-binary section along the experimental tie line for $\text{Gd}_{35}\text{Ti}_{35}\text{Co}_{30}$ also can be estimated by fitting the power law to the position difference of the first maxima $\Delta q_1^{\text{Ti-Gd}}$,

$$\Delta q_1^{\text{Ti-Gd}} = q_0 (1 - T / T_c)^\beta \quad (4.9)$$

where q_0 is a constant and critical-point exponent β equals to 0.30. The fitting result to the experimental data is shown in Fig. 4.22. The value of T_c for the pseudo-binary section is estimated to be $T_c = 1780 \pm 10$ K.

4.1.3.2 Microstructure of as-solidified Gd-Ti-Co alloys

Fig. 4.23 shows SEM images of the cross sections of the different cast Co-Gd-Ti alloys. As shown in Fig. 4.23a and b, the microstructures of the $\text{Gd}_{50}\text{Ti}_{20}\text{Co}_{30}$ and $\text{Gd}_{32.5}\text{Ti}_{32.5}\text{Co}_{35}$ alloys show homogeneously distributed primary CoTi dendrites within a matrix of CoGd_3 and Gd solid solution phases but no indication of any kind of liquid-liquid phase separation. On the other hand, the microstructures of other alloys shown in Fig. 4.23c-f, clearly reveal the occurrence of the decomposition into two liquids by a liquid phase separation $L \rightarrow L_1 + L_2$.

The chemical composition of the solidified liquid phases over relatively large areas has been determined by EDX analysis in order to approximate the composition range of the miscibility gap in the ternary Gd-Ti-Co system. Obtained values of the chemical composition are summarized in Table 4.6 together with the constituent phases. According

to occurrence or absence of the liquid-liquid phase separation, the alloys are divided into two groups as shown in Table 4.6. The alloys in group 1 consist of primary CoTi dendrites within the matrix of *hcp*-Gd and CoGd₃ (*Pnma*) [104] phases with different volume fractions as shown in insets of Fig. 4.23a and b. This reveals the similar solidification and phase transformation process of these two alloys. The solubilities of Gd in CoTi phase and Ti in CoGd₃ phase were measured to be about 1 at.%. On the other hand, the alloys in group 2 exhibit rather complex phase transformation process due to the liquid-liquid phase separation. The compositions of the

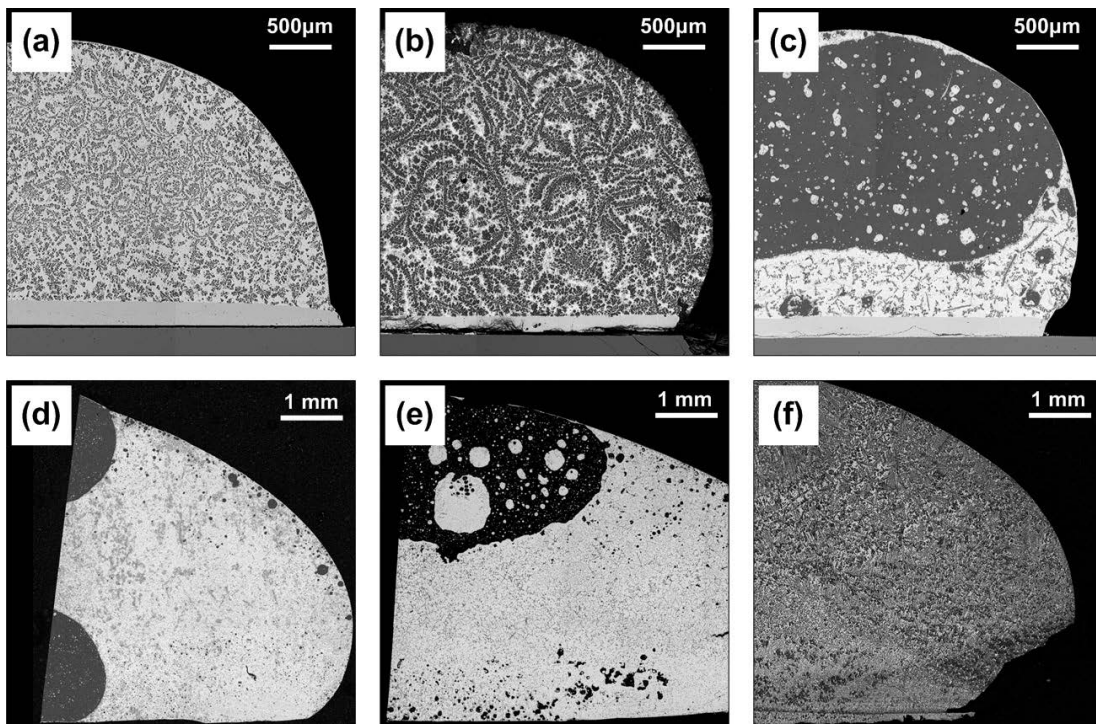


Figure 4.23: SEM images of the Gd-Ti-Co alloys: (a) Gd₅₀Ti₂₀Co₃₀, (b) Gd_{32.5}Ti_{32.5}Co₃₅, (c) Gd₃₅Ti₃₅Co₃₀, (d) Gd₂₀Ti₅₀Co₃₀, (e) Gd₄₅Ti₄₅Co₁₀ and (f) Gd_{37.5}Ti_{37.5}Co₂₅. Secondary phase reactions and decomposition occurring within the two primary liquids upon quenching are also visible.

separated Gd-rich and Ti-rich liquid phases show strong dependence on the alloy composition due to different solidification paths along the corresponding tie lines as summarized in Table 4.6. The Gd-rich liquid phases in the Gd₃₅Ti₃₅Co₃₀, Gd₂₀Ti₅₀Co₃₀ and Gd_{37.5}Ti_{37.5}Co₂₅ (in group 2) alloys, consist of the same mixture of primary CoTi dendrites and the matrix consisting of *hcp*-Gd and CoGd₃ phases as determined from the microstructure and chemical composition analysis. This suggests that the compositions of one end of the tie lines (Gd-rich side) end up in the same phase region. Analogously, the

solidified Ti-rich liquid phases of the three alloys exhibit similar behavior with the microstructures consisting of primary CoTi dendrites within an eutectic matrix (Ti(Co, Gd) + CoTi₂) of about Gd₂Ti₇₆Co₂₂ in chemical composition. This also leads to the conclusion that the opposite end of the tie lines (Ti-rich side) end up in the same phase region, and the Ti-rich liquid solidifies by the phase transformation scheme $L_2 \rightarrow \text{CoTi} + L_2 \rightarrow \text{CoTi} + \text{CoTi}_2 + \text{Ti}(\text{Co, Gd})$. In contrast, a different phase transformation process is essential for the Gd₄₅Ti₄₅Co₁₀ alloy (see Table 4.6).

Table 4.6: According to the characteristic features that occur upon liquid-liquid phase separation, the alloys investigated in this work are divided into two groups. Information on chemical compositions obtained by EDX analysis for the phase separated liquids (for group 2) or crystalline phases (for group 1) are summarized. The subsequent phases in each decomposed liquid are also given

Alloys	Phases	Compositions (at.%)	Constituent phases in solidified liquids	in Fig. 4.23
<i>Group 1</i>				
Gd ₅₀ Ti ₂₀ Co ₃₀	hcp-Gd	Gd ₉₅₍₁₎ Ti ₁₍₁₎ Co ₄₍₁₎		a
	CoGd ₃	Gd ₇₄₍₁₎ Ti ₁₍₁₎ Co ₂₅₍₁₎		
	CoTi	Gd ₁₍₁₎ Ti ₅₄₍₁₎ Co ₄₄₍₁₎		
Gd _{32.5} Ti _{32.5} Co ₃₅	hcp-Gd	Gd ₉₄₍₁₎ Ti ₁₍₁₎ Co ₅₍₁₎		b
	CoGd ₃	Gd ₇₉₍₁₎ Ti ₁₍₁₎ Co ₂₀₍₁₎		
	CoTi	Gd ₁₍₁₎ Ti ₅₆₍₁₎ Co ₄₃₍₁₎		
<i>Group 2</i>				
Gd ₃₅ Ti ₃₅ Co ₃₀	Gd-rich liquid	Gd ₄₇₍₂₎ Ti ₂₃₍₂₎ Co ₃₀₍₁₎	Gd + CoGd ₃ + CoTi	c
	Ti-rich liquid	Gd ₉₍₁₎ Ti ₅₆₍₂₎ Co ₃₅₍₁₎	Gd + CoTi + eutectic matrix*	
Gd ₂₀ Ti ₅₀ Co ₃₀	Gd-rich liquid	Gd ₆₁₍₃₎ Ti ₁₈₍₃₎ Co ₂₂₍₁₎	Gd + CoGd ₃ + CoTi	d
	Ti-rich liquid	Gd ₃₍₁₎ Ti ₆₈₍₁₎ Co ₂₉₍₁₎	Gd + CoTi + eutectic matrix	
Gd ₄₅ Ti ₄₅ Co ₁₀	Gd-rich liquid	Gd ₈₀₍₃₎ Ti ₁₃₍₃₎ Co ₇₍₁₎	Gd + Ti + CoTi ₂	e
	Ti-rich liquid	Gd ₃₍₁₎ Ti ₈₅₍₁₎ Co ₁₂₍₁₎	Gd + Ti + eutectic matrix	
Gd _{37.5} Ti _{37.5} Co ₂₅	Gd-rich liquid	Gd ₆₉₍₂₎ Ti ₁₂₍₁₎ Co ₁₉₍₁₎	Gd + CoGd ₃ + CoTi	f
	Ti-rich liquid	Gd ₅₍₂₎ Ti ₆₉₍₁₎ Co ₂₆₍₂₎	Gd + CoTi + eutectic matrix	

* The eutectic matrix in the Ti-rich liquid exhibits an average composition of about Ti₇₅₍₃₎Gd₂₍₁₎Co₂₂₍₃₎ which is in accordance with [23].

Fig. 4.24 shows an isothermal section of the ternary Gd-Ti-Co phase diagram at $T = 1500$ K calculated by the *CALPHAD* method (only up to 50 at.% Co is drawn here) representing only an extrapolation of the liquid phases from the three binary phase diagrams [105,106]. Since the solid phases were excluded and no ternary interaction

parameters are known for the calculation, the presented result is only a first approximation. The nominal compositions of the as-cast alloys and the compositions of the Gd-rich and Ti-rich liquid phases obtained from EDX analysis are marked by large solid symbols and corresponding open symbols, respectively. The average values of these data points presented in Fig. 4.24 are also given in Table 4.6. The calculated phase boundary between the homogeneous liquid L and the region of two liquids $L_1 + L_2$ is given by solid line together with the calculated tie lines (dashed lines) of the two liquids for $\text{Gd}_{35}\text{Ti}_{35}\text{Co}_{30}$, $\text{Gd}_{37.5}\text{Ti}_{37.5}\text{Co}_{25}$ and $\text{Gd}_{45}\text{Ti}_{45}\text{Co}_{10}$. Although there is slight difference between the experimental results and calculation, but nevertheless, the general tendency of the extension and the directions of the tie-lines are reproduced. As also shown in Fig. 4.24, experimental results give no indication of a phase separation for the $\text{Gd}_{50}\text{Ti}_{20}\text{Co}_{30}$ and $\text{Gd}_{32.5}\text{Ti}_{32.5}\text{Co}_{35}$ alloys, despite the fact that the compositions of these alloys lie within the calculated miscibility gap. The following reasons are somewhat explain the discrepancy between the experimental results and calculation.

For the calculation of ternary Gd-Ti-Co phase equilibria in this work, only the liquid phases of the constituent binary systems were considered. And the compositions of the separated liquid phases determined by EDX analysis do not exactly reflect the equilibrium compositions of the liquid phases. The first experimental and thermodynamic assessment of the ternary Gd-Ti-Co system particularly focusing on the liquid-liquid miscibility gap has been successfully carried out. We have obtained a direct evidence of liquid-liquid phase separation in the ternary Gd-Ti-Co system by *in situ* X-ray diffraction. The coexistence of two liquid phases in the high temperature range $1690 \text{ K} < T < 1760 \text{ K}$ was experimentally proven. The stable miscibility gap of the binary Gd-Ti system extends into the ternary Gd-Ti-Co system for up to about 35 at.% Co as the experimental results and the thermodynamic approximation by *CALPHAD* calculation concluded.

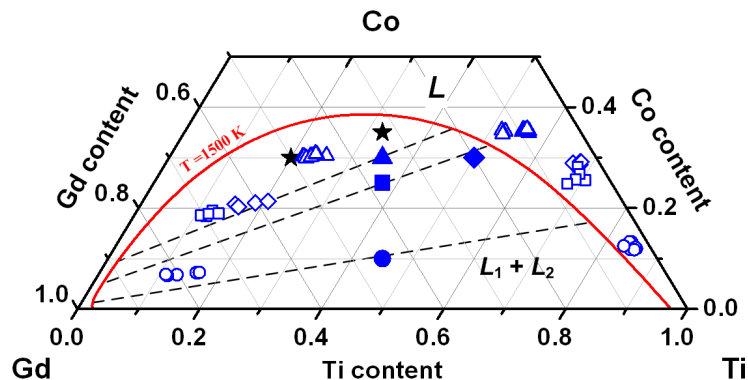


Figure 4.24: Schematic illustration of the section of the ternary Gd-Ti-Co phase diagram with nominal compositions of the alloys (solid symbols) and the compositions of phase separated liquids (corresponding open symbols). Circles: $\text{Gd}_{45}\text{Ti}_{45}\text{Co}_{10}$, squares: $\text{Gd}_{37.5}\text{Ti}_{37.5}\text{Co}_{25}$, triangles: $\text{Gd}_{35}\text{Ti}_{35}\text{Co}_{30}$, rhombi: $\text{Gd}_{20}\text{Ti}_{50}\text{Co}_{30}$. The alloys with no indication of phase separation are marked by black star symbols. The isothermal miscibility gap (red solid line) at $T = 1500$ K, including the calculated tie lines (dashed lines) calculated by *CALPHAD* method is also given.

4.2 Structure formation and phase separation in Gd-based metallic glasses

In this section, attempts will be presented to synthesize new phase separated metallic glasses especially in Gd-based multi-component alloys Gd-TM-Co-Al (TM = Hf, Ti or Zr) and to characterize their structure formations.

4.2.1 Phase separation in Gd-Hf-Co-Al alloys

The cooling rate and composition dependences of microstructure evolution in rapidly quenched $\text{Gd}_{55-x}\text{Hf}_x\text{Co}_{25}\text{Al}_{20}$ ($x = 0, 10, 20, 27.5, 35, 45$ and 55 at.%) alloys are presented. The alloy system was chosen because the system fulfills the prerequisites for the development of phase separated metallic glass: The ternary $\text{Gd}_{55}\text{Co}_{25}\text{Al}_{20}$ and $\text{Hf}_{55}\text{Co}_{25}\text{Al}_{20}$ alloys are known that exhibit a high glass forming ability (successfully produced in cylindrical form with about 2 mm in diameter) [20,107]. And there is a large positive enthalpy of mixing $\Delta H_{\text{mix}} = + 11 \text{ kJ mol}^{-1}$ between Gd and Hf [9,10] providing a tendency of the decomposition into the Gd-rich and the Hf-rich liquid phases during quenching. In order to explain the phase separation and glass formation in Gd-Hf-Co-Al quaternary alloys, enthalpies of mixing (ΔH_{mix}) between constituent elements are given in Table 4.7. The positive value of enthalpy of mixing between Gd and Hf drives the phase separation in the system. On the other hand, two minor alloy elements Co and Al were chosen due to their large negative enthalpy of mixing with the main elements. These negative enthalpies of mixing are prerequisites for glass forming.

Table 4.7: Enthalpy of mixing (ΔH_{mix}) relationship for binary atomic pairs in the Gd-Hf-Co-Al alloy system [9,10]

ΔH_{mix} (kJ mol ⁻¹)	Gd	Hf	Co	Al
Gd	0	+ 11	- 22	- 38
Hf	-	0	- 35	- 39
Co	-	-	0	- 19
Al	-	-	-	0

4.2.1.1 Phase formation and thermal stability

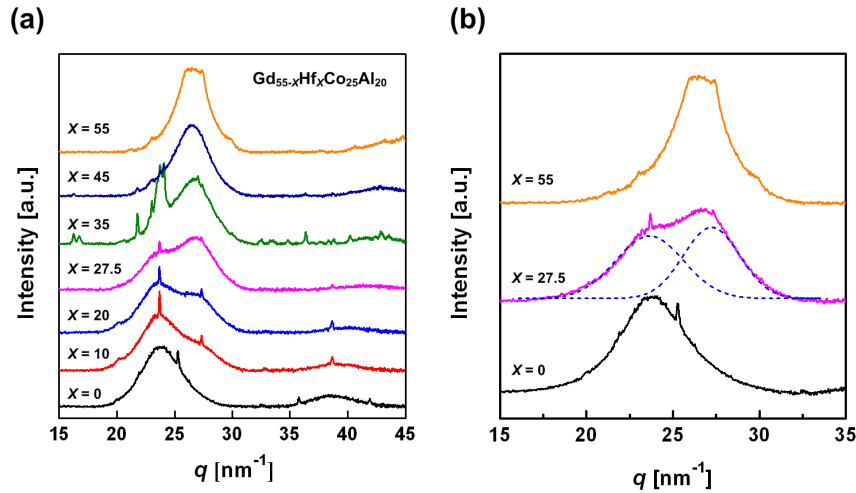


Figure 4.25: (a) XRD patterns of as-quenched $\text{Gd}_{55-x}\text{Hf}_x\text{Co}_{25}\text{Al}_{20}$ alloy ribbons ($x = 0, 10, 20, 27.5, 35, 45$ and 55 at.%). (b) Enlarged XRD patterns of $x = 0, 27.5$ and 55 . Dashed curves are the results of two Gaussian curves fitting.

A series of glassy ribbons of $\text{Gd}_{55-x}\text{Hf}_x\text{Co}_{25}\text{Al}_{20}$ ($x = 0, 10, 20, 27.5, 35, 45$ and 55 at.%) were prepared by melt spinning method, and the corresponding XRD patterns are shown in Fig. 4.25. The broad diffuse diffraction maxima indicating the amorphous nature of the as-spun ribbons are visible for all samples. For the alloy ribbons with Hf content $x = 10 - 45$ at.%, the occurrence of liquid-liquid phase separation is clearly revealed by two diffuse maxima which represents the coexistence of two glassy phases. According to a relative difference of the interatomic distances for both glassy phases, one can conclude that the first maximum at lower q -value ($q_1 \approx 23.8 \text{ nm}^{-1}$) corresponds to a Gd-rich glassy phase whereas the other maximum at higher q -value ($q_1 = 26.7 \text{ nm}^{-1}$) represents the Hf-rich glassy phase. Some of weak and sharp diffraction peaks indicating presence of small amount of crystalline phases are also visible for all alloys [20,107,108]. This is due to the reduced GFA of the alloys. Differences in the intensity ratios of two glassy phases for the different alloy compositions are related to the volume fractions of the phases in accordance with the lever rule. In order to estimate the volume fractions of the two glassy phases, the first diffuse halos at range of $q \approx 15 - 35 \text{ nm}^{-1}$ were fitted by two Gaussian functions. Fitted curves for the $\text{Gd}_{27.5}\text{Hf}_{27.5}\text{Co}_{25}\text{Al}_{20}$ alloy are shown in Fig. 4.25b (dashed curves). Under

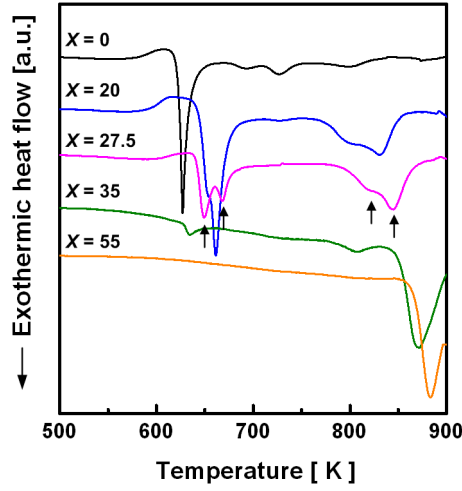


Figure 4.26: DSC traces obtained from $\text{Gd}_{55-x}\text{Hf}_x\text{Co}_{25}\text{Al}_{20}$ ($x = 0, 20, 27.5, 35$ and 55 at.%) at a heating rate of 40 K min^{-1} . Arrows indicate the overlaid exothermic peaks corresponding to secondary phase separation during quenching the melt.

the assumption that the area of Gaussian curves represents the volume fraction of the corresponding glassy phase, the volume fraction of Gd-rich phase V_{Gd} can be estimated by

$$V_{\text{Gd}} \approx \frac{A_{\text{Gd}}}{A_{\text{Gd}} + A_{\text{Hf}}}, \quad (4.10)$$

where A is the integral of the Gaussian curve. The results exhibit a linear dependence of the Gd-rich phase fraction with Hf content, and the values of the estimation are summarized in Table 4.8. For $x = 20, 27.5$ and 35 at.%, the presence of two glassy phases is also reflected by two crystallization events in DSC curves. As shown in Fig. 4.26 the comparison of DSC curves with that of two monolithic metallic glasses $x = 0$ and 55 at.% infers that the first exothermic event at lower temperature range $T_x^1 = 620 - 650 \text{ K}$ corresponds to the crystallization of the Gd-rich glassy phase, and that at higher temperature range $T_x^2 > 830 \text{ K}$ corresponds to the Hf-rich glassy phase, respectively. A change of the volume fraction ratios as a function of composition is also reflected by the change of the integral of exothermic events.

Table 4.8: Volume fractions of the Gd-rich phases estimated by Gaussian fitting with XRD patterns and image analysis of SEM micrographs.

Alloy composition	Vol. % (XRD)	Vol. % (Micrograph)
Gd ₅₅ Co ₂₅ Al ₂₀	100	100
Gd ₄₅ Hf ₁₀ Co ₂₅ Al ₂₀	77 ± 4	82 ± 2
Gd ₃₅ Hf ₂₀ Co ₂₅ Al ₂₀	63 ± 3	66 ± 1
Gd _{27.5} Hf _{27.5} Co ₂₅ Al ₂₀	36 ± 2	45 ± 3
Gd ₂₀ Hf ₃₅ Co ₂₅ Al ₂₀	23 ± 3	31 ± 4
Gd ₁₀ Hf ₄₅ Co ₂₅ Al ₂₀	8 ± 2	15 ± 4
Hf ₅₅ Co ₂₅ Al ₂₀	0	0

4.2.1.2 Microstructure investigation

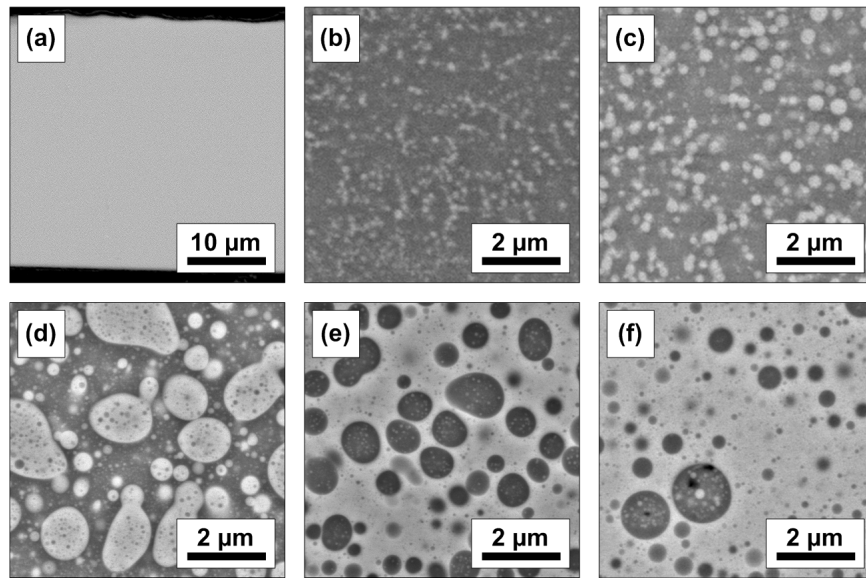


Figure 4.27: Backscattered electron micrographs obtained from the cross-section of rapidly quenched ribbons.

Fig. 4.27 shows a series of SEM images obtained from the cross-section of the ribbons for the alloys with different Hf content $x = 0 - 45$ at.%. A homogeneous structure without any contrast which is typical for a monolithic metallic glass is observed from the as-spun Gd₅₅Co₂₅Al₂₀ alloy within the experimental resolution limit of the SEM. On the other hand, the alloys with Hf addition exhibit morphologies of heterogeneous droplet-like

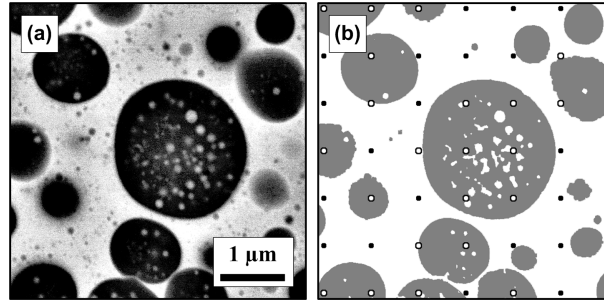


Figure 4.28: (a) The backscattered SEM image as-obtained from $x = 35$. (b) Its thresholded image with grid of points for phase fraction measurement. Open circles represent the points that lay on the Gd-rich phase.

structure with different volume fraction ratios of Gd-rich (dark) and Hf-rich (bright) glassy phases. As can be seen by comparing microstructures shown in Fig. 4.27b-f, the size and volume fraction ratios vary with different Hf additions. From the comparison of microstructures of $x = 27.5$ and 30 at.%, one can also see the phase inversion of precipitates and matrix inferring that the composition with the maximum critical temperature T_c of the miscibility gap present between $x = 27.5$ and 30 at.%.

A method of regular grid of points overlapped onto thresholded backscattered SEM images is used to determine the volume fraction of two glassy phases, i.e. the volume fraction of Gd-rich glassy phase has been provided by dividing the number of points (opened circles in Fig. 4.28b for example) laying on the Gd-rich glassy phase by the total number of points. The original backscattered SEM image and the thresholded image of the $\text{Gd}_{20}\text{Hf}_{35}\text{Co}_{25}\text{Al}_{20}$ alloy with grid of points are shown in Fig. 4.28. In order to reduce the statistical error more than three different SEM images from each alloy were used with automatic point counting by Boolean logic [109]. The calculated values are also given in Table 4.8 which are in a good agreement with the XRD data. The chemical compositions of the primarily decomposed and solidified Gd-rich and Hf-rich liquids were determined by EDX analysis. Although both domains droplets and matrix are not homogeneous but containing the secondary precipitates, the determined compositions can be representative at least for the certain temperature range within the miscibility gap. The Gd- and Hf-enrichment of two glassy phases were clearly distinguished from EDX results. For the alloys with $x = 10, 27.5$ and 45 at.%, the microstructures in more detail were investigated with the scanning transmission electron microscopy (STEM) images (shown in Fig. 4.29)

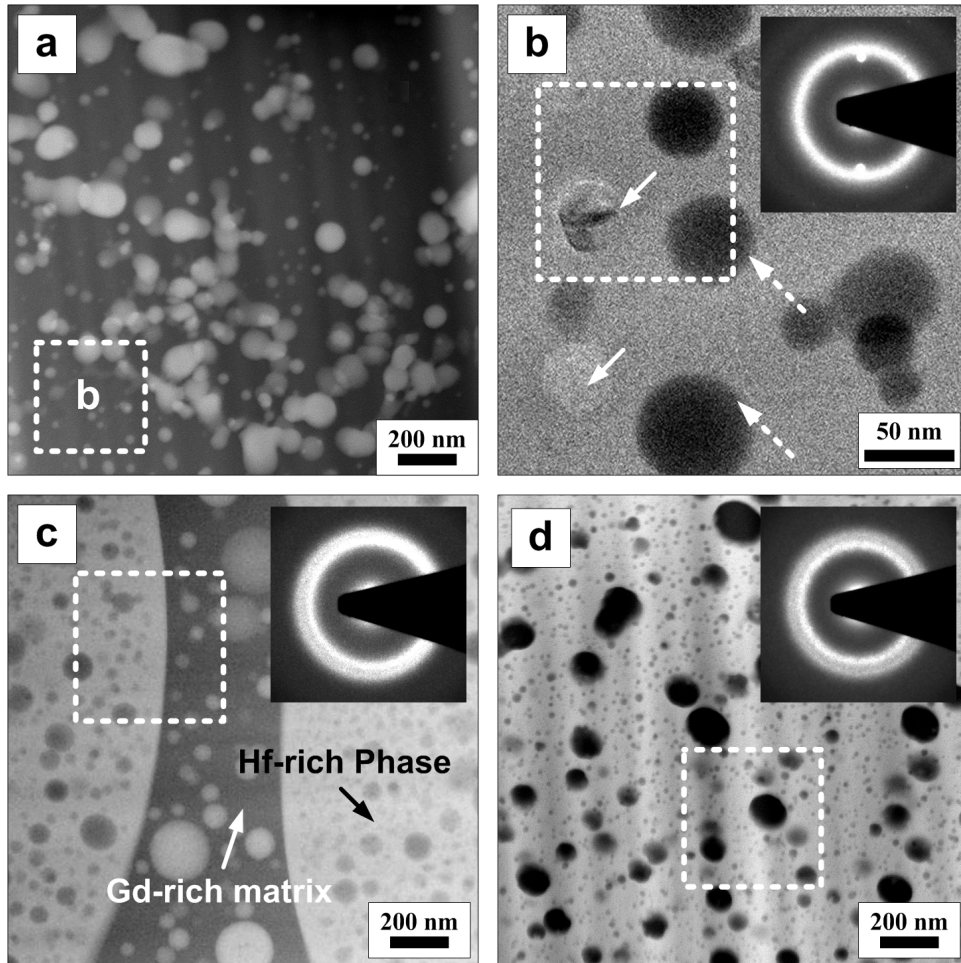


Figure 4.29: STEM-HAADF images obtained from (a) $x = 10$, (c) $x = 27.5$ and (d) $x = 45$. Bright field TEM image of the alloy with (b) $x = 10$ at.%. The corresponding selected area diffraction patterns are displayed as insets.

obtained in high angle annular dark field (HAADF) mode. The corresponding selected area diffraction patterns (SADP) are given as insets. The STEM-HAADF images in Fig. 4.29a, c and d distinctly show morphologies of droplet-like structures consisting of two glassy phases. The microstructure of $x = 27.5$ at.% (Fig. 4.29c) clearly shows the secondary precipitates within the primarily decomposed phases, i.e. nano-sized Gd-rich phase (dark spots) precipitated in the primary Hf-rich droplets (bright), for example. However, for the alloys $x = 10$ and 45 at.% (Fig. 4.29a and d, respectively), no such features of secondary precipitation was observed. The coexistence of two glassy phases was also confirmed by the corresponding SAED patterns with two diffuse halos: the outer and inner halo rings correspond to the Hf-rich glassy phase and the Gd-rich phase, respectively. Fig. 4.29b shows an enlarged TEM bright field image of the $x = 10$ as-spun ribbon together with the diffraction pattern obtained from the marked area (dashed square in Fig. 4.29a). The SADP

exhibits only the inner halo ring for the Gd-rich glassy matrix and some spots for an unknown Gd based crystallites (marked by solid arrows) despite the Hf-rich glassy phases (marked by dashed arrows) are still visible in the microstructure. This is due to that the intensity of electron diffraction maximum scattered from the Gd-rich phase is much stronger to overlap the intensity of the Hf-rich phase. Additional EDX analysis in STEM mode was carried out in order to determined local chemical composition of two different glassy phases. For alloys with Hf content $x = 10, 27.5$ and 45 at.%, the obtained values are summarized in Table 4.9 together with the values of $x = 0$ and 55 at.%.

Table 4.9: Chemical compositions of Gd-rich phase and Hf-rich phase for alloys with Hf content $x = 0, 10, 27.5, 45$ and 55 at.% determined by EDX analysis. Results have standard deviations of up to 2.3 %.

Alloy composition	Gd-rich phase		Hf-rich phase	
	Average composition (Std. Dev.)		Average composition (Std. Dev.)	
Gd ₅₅ Co ₂₅ Al ₂₀	Gd _{51.3} Co ₂₈ Al _{20.7}	(0.25)	-	
Gd ₄₅ Hf ₁₀ Co ₂₅ Al ₂₀	Gd _{55.1} Hf _{1.7} Co _{25.8} Al _{17.4}	(1.25)	Gd _{7.4} Hf _{41.8} Co _{42.2} Al _{8.6}	(2.30)
Gd _{27.5} Hf _{27.5} Co ₂₅ Al ₂₀	Gd _{57.9} Hf _{3.9} Co _{16.7} Al _{21.5}	(1.58)	Gd _{6.4} Hf _{46.8} Co _{35.8} Al ₁₁	(1.19)
Gd ₁₀ Hf ₄₅ Co ₂₅ Al ₂₀	Gd _{65.6} Hf _{0.5} Co _{0.5} Al _{33.4}	(0.53)	Gd _{2.8} Hf _{52.1} Co _{30.3} Al _{14.8}	(0.43)
Hf ₅₅ Co ₂₅ Al ₂₀	-		Hf _{49.9} Co _{25.3} Al _{24.8}	(0.66)

4.2.2 Phase separation in Gd-Ti-Co-Al alloy

This section presents the results of investigation on how the partial substitution of Gd in Gd-Co-Al bulk metallic glass by Ti ($\Delta H_{\text{mix}}^{\text{Gd-Ti}} = + 15 \text{ kJ mol}^{-1}$), influences on the phase separation behavior [9,10]. Partial substitution of Gd with Ti by 30 at.% was carried out. Rapidly quenched ribbons of $\text{Gd}_{60}\text{Co}_{30}\text{Al}_{10}$ and $\text{Gd}_{30}\text{Ti}_{30}\text{Co}_{30}\text{Al}_{10}$ were prepared again by single roller melt spinning.

The X-ray diffraction patterns obtained from $\text{Gd}_{60-x}\text{Ti}_x\text{Co}_{30}\text{Al}_{10}$ ($x = 0$ and 30 at.%) as-spun ribbons are shown in Fig. 4.30. As expected the ternary starting alloy $x = 0$ exhibits a XRD pattern with typical diffuse maximum ($q = 23.5 \text{ nm}^{-1}$) reflecting a homogeneous glassy structure. On the other hand, a mixture of diffuse maxima ($q_1 = 23.1 \text{ nm}^{-1}$) and sharp crystalline peaks observed from the XRD pattern for $\text{Gd}_{30}\text{Ti}_{30}\text{Co}_{30}\text{Al}_{10}$ revealing that the alloy consists of Gd-rich glassy phase and CoTi phase [111]. The microstructure of the ternary $\text{Gd}_{60}\text{Co}_{30}\text{Al}_{10}$ shows the absence of any contrast within the resolution of SEM (Fig. 4.31a) as expected from the XRD results. This implies a monolithic glassy nature of the alloys without any major heterogeneity such as a second glassy phase or significant crystallites. The $\text{Gd}_{30}\text{Ti}_{30}\text{Co}_{30}\text{Al}_{10}$ ribbon shows a morphology of well developed droplet structure, as shown in Fig. 5.8b. All the microstructural features

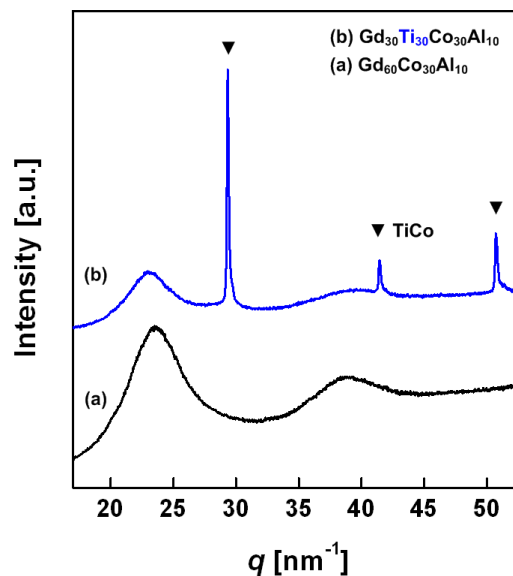


Figure 4.30: XRD patterns measured for as-spun ribbons.

like a spherical shape of Ti-rich precipitates (marked by dashed circles), coalescence of liquid droplets (arrow) and nano-scaled secondary precipitates within primary phases (shown in Fig. 4.31c), unambiguously indicates that the $\text{Gd}_{30}\text{Ti}_{30}\text{Co}_{30}\text{Al}_{10}$ alloy undergo a liquid-liquid phase separation during rapidly quenching the melt. Despite the occurrence of liquid-liquid phase separation in this alloy, only a single glassy phase enriched in Gd together with the crystalline phase (TiCo) were proven by XRD result. This implies that the Gd-rich liquid got frozen-in and formed a glassy matrix while the Ti-rich liquid solidified into crystalline phase due to insufficient glass forming ability. The resulting alloy is then a glass-crystalline composite.

The phase separation in metallic glasses strongly depends on the composition and solidification process, as concluded from the results above. Therefore, one could tailor the phase separating metallic glasses to obtain types of composite materials such as glass-glass, glass-crystalline and even crystalline-crystalline with variety of microstructures either by controlling the conditions of solidification process or designing a new alloy composition.

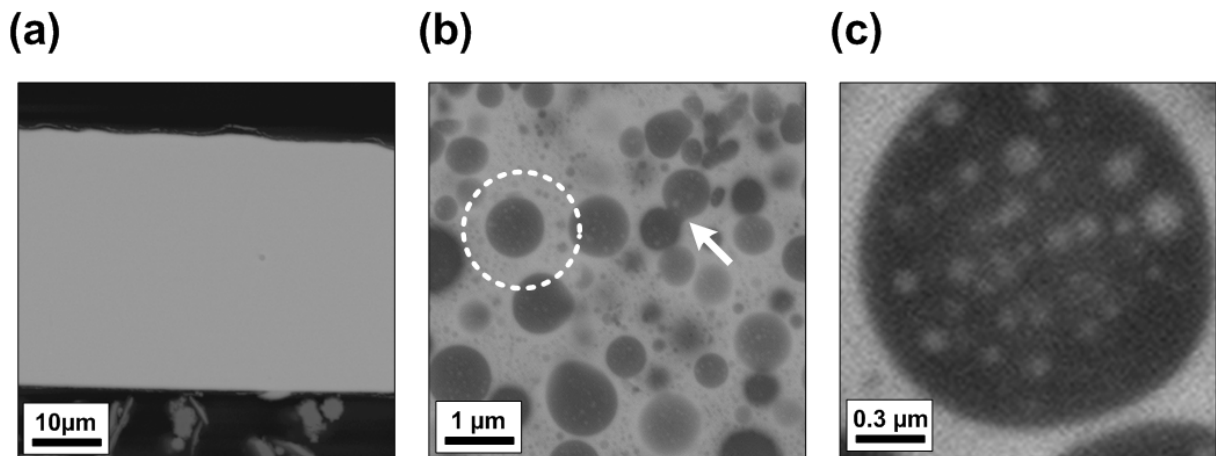


Figure 4.31: SEM micrographs with backscattered electron contrast obtained from the cross section of (a) $\text{Gd}_{60}\text{Co}_{30}\text{Al}_{10}$ and (b) $\text{Gd}_{30}\text{Ti}_{30}\text{Co}_{30}\text{Al}_{10}$ ribbons. The arrow and dashed circle indicate the coalescence of droplets and the secondary precipitates, respectively. (c) A magnified SEM image for the circled area in (b).

4.2.3 Phase separation in Zr-Gd-Co-Al alloys

This section attempts to introduce the results of the investigation on phase separation in rapidly quenched $Zr_{56-x}Gd_xCo_{28}Al_{16}$ ($0 \leq x \leq 20$) glassy ribbons. The ternary Zr-Co-Al [21] and Gd-Co-Al [20] alloys are bulk glass forming systems, and the enthalpy of mixing between Zr and Gd is $+9 \text{ kJ mol}^{-1}$ [9,10]. Therefore, the quaternary alloy system here, i.e. Zr-Gd-Co-Al is a suitable candidate for phase separated MGs. We will show that how the different amount of Gd content influences on the development of phase separation and corresponding microstructures.

4.2.3.1 Characterization of the as-quenched states

The bright field transmission electron microscope (TEM) images and the corresponding selected area electron diffraction (SAED) patterns for as-spun $Zr_{56-x}Gd_xCo_{28}Al_{16}$ ($x = 5, 10$ and 20 at.%) ribbons are presented in Fig. 4.32. A featureless contrast and single diffuse halo obtained from $x = 5$ (Fig. 4.32a) represent the monolithic glassy nature of the sample without the presence of any type of heterogeneity such as fine crystallites or a secondary glassy phase. This implies that only a small amount of Gd ($x \leq 5$ at.%) exhibits no influence on the occurrence of phase separation. However, this might be affected by the limitations of TEM spatial resolution with respect to very low and continuous profile of possible concentration fluctuations. The presence of spherical heterogeneities (marked by arrows) of about 10 nm in size was revealed from the microstructure for $x = 10$ at.% (Fig. 4.32b). The average value of the inter-cluster distance is measured to be about 20 nm. Two diffuse halo rings in the corresponding SAED pattern represent the presence of two glassy phases. For $x = 20$ (Fig. 4.32c), the heterogeneous microstructure with two glassy phases are

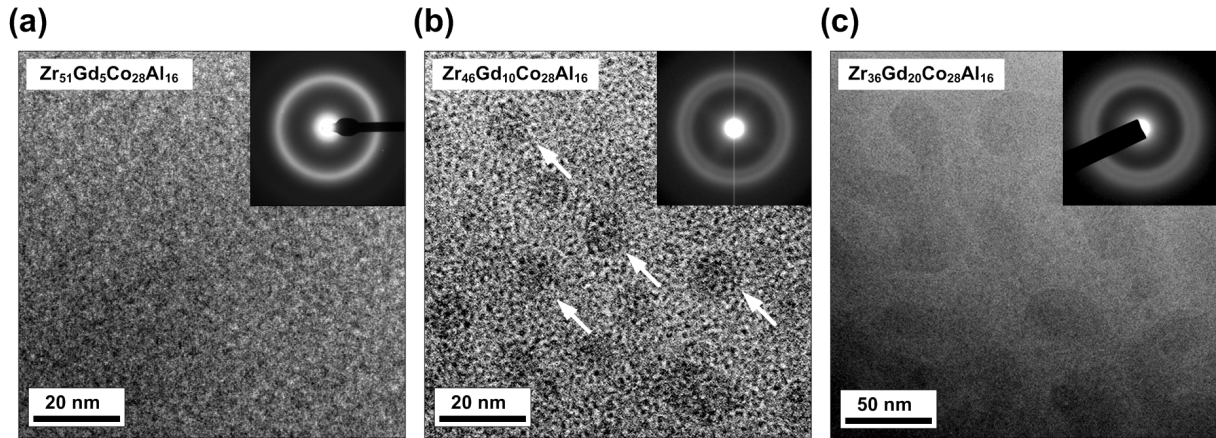


Figure 4.32: TEM bright field images and corresponding selected area electron diffraction (SAED) patterns of the (a) $\text{Zr}_{51}\text{Gd}_5\text{Co}_{28}\text{Al}_{16}$, (b) $\text{Zr}_{46}\text{Gd}_{10}\text{Co}_{28}\text{Al}_{16}$ and (c) $\text{Zr}_{36}\text{Gd}_{20}\text{Co}_{28}\text{Al}_{16}$ as-spun ribbons.

further coarsened by coalescence of the clusters and growth. The radial intensity profiles (shown in Fig. 4.33b) confirm that the regions with dark contrast are Gd-rich clusters. The TEM investigation proves that the Zr-Gd-Co-Al alloys with higher Gd contents $x \geq 10$ at.% undergo liquid-liquid phase separation into Zr- and Gd- rich glassy phases during quenching.

In order to confirm the glassy structure of the as-quenched ribbons, the XRD patterns are compared with the radial intensity profiles obtained from the SAED patterns of TEM investigation as shown in Fig. 4.33. The diffuse character of the XRD patterns for all ribbons represents their glassy structure. Decomposition into two glassy phases is proved by the broadened and asymmetric shape of the first diffuse maxima as marked by arrows in Fig. 4.33a. The intensities for second glassy phase become more pronounced as Gd content increased. The radial intensity profiles of SAED patterns (Fig. 4.33b) also clearly exhibit a splitting into two maxima for $x = 10$ and 20 at.%. The additional diffuse maxima at $q \approx 21.5 \text{ nm}^{-1}$ correspond to the formation of a Gd-rich glassy phase, and its increase in volume fraction with Gd content is also revealed in the intensity. For comparison, the XRD pattern of $\text{Gd}_{60}\text{Co}_{30}\text{Al}_{10}$ glassy ribbon is also given. A few additional peaks indicating the presence of some unknown crystalline phases are also observed from the XRD patterns for $x = 15$ and 20 . This is probably due to partial crystallization at the surface region during melt spinning method. The glassy nature of the $\text{Zr}_{56-x}\text{Gd}_x\text{Co}_{28}\text{Al}_{16}$ ribbons ($x = 0 - 20$ at.%) are also revealed from the thermal behavior with the occurrence of a glass transitions in the

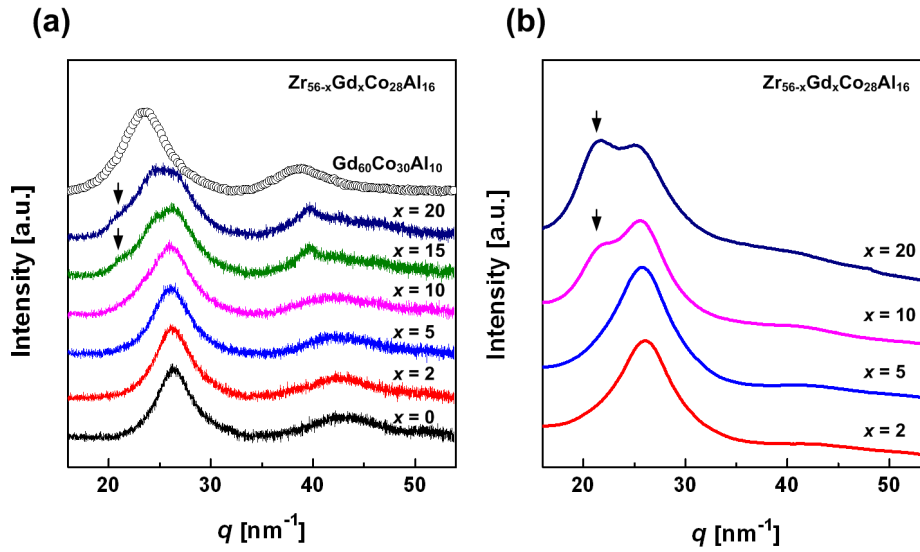


Figure 4.33: (a) XRD patterns obtained for the $Zr_{56-x}Gd_xCo_{28}Al_{16}$ ($0 \leq x \leq 20$) melt-spun ribbons. The XRD pattern for the $Gd_{60}Co_{30}Al_{10}$ glass is also shown (open circles) for comparison [10]. (b) Radial intensity profiles obtained from the TEM SAED patterns for $x = 2, 5, 10$ and 20 .

temperature interval $T_g = 710 - 760$ K and following crystallization events with a strong exothermic peak at $T_x = 775 - 820$ K.

Corresponding DSC curves upon continuous heating are presented in Fig. 4.34. As reported earlier [22], for all the samples two-step crystallization accompanied by two exothermic events corresponding to the formation of $ZrCoAl$ ($P6_3/mmc$), $ZrCo$ ($Pm-3m$) and Zr_6Al_2Co ($P-62m$) phases, is typical for the Zr-Co-Al glasses. In comparison to the $Zr_{56}Co_{28}Al_{16}$ glass, the glass transition temperature T_g and the crystallization temperature T_x shift to lower temperature range with small addition of Gd ($x \leq 5$ at.%) as indicated by arrows. The glass transition temperatures and corresponding supercooled liquid region become indistinguishable for the alloys with further increased Gd addition ($x = 10 - 20$ at.%). For $x = 15$ and 20 at.%, despite the features of phase separation determined from TEM and XRD results, no indications for neither a glass transition nor a crystallization related to the Gd-rich glassy phase were observed. According to the DSC curve for the $Gd_{60}Co_{30}Al_{10}$ [108] glass presented by dashed line in Fig. 4.34, a thermal event for Gd-rich glassy phase was expected to occur in the temperature range of $T = 600 - 650$ K. The absence of the thermal event for the Gd-rich second glassy phase is similar to the results in Ref [14] that with up to 15 at.% Gd addition in Zr-Gd-Cu-Al glasses, also no distinct DSC signal for a Gd-rich phase was observed.

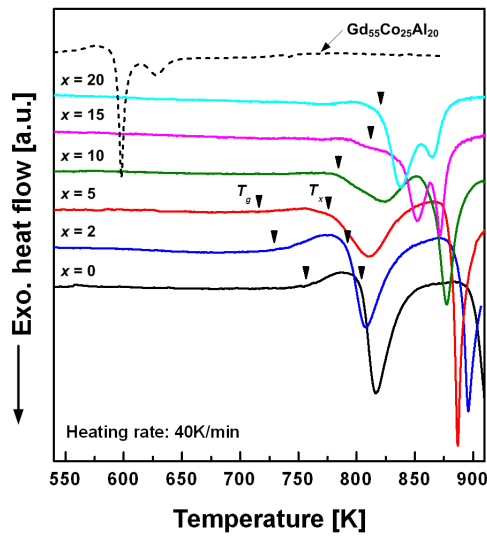


Figure 4.34: DSC scans of $Zr_{56-x}Gd_xCo_{28}Al_{16}$ ($0 \leq x \leq 20$) glasses at a heating rate of 40 K min^{-1} . Glass transition (endothermic events after T_g) and crystallization (exothermic peaks) events confirm the amorphous state of the samples. Arrows indicate T_g . The DSC curve of $Gd_{60}Co_{30}Al_{10}$ glass is also shown for comparison (dashed line) [108].

The XRD patterns of as-spun $Zr_{56-x}Gd_xCo_{28}Al_{16}$ glassy ribbons ($0 \leq x \leq 20$) obtained from small-angle X-ray scattering (SAXS) compare the different degrees of the heterogeneities as shown in Fig. 4.35. It should be noted first that the increase in SAXS intensity at very low scattering angle $q < 0.4 \text{ nm}^{-1}$ is not due to chemical heterogeneity but is probably caused by surface roughness of the as-spun ribbon samples. This has also been observed for other homogeneous metallic glasses [112]. A homogeneous glassy structure without any features for either phase separation or any heterogeneity is ascertained by the very low SAXS intensities for $x = 0$ and 2 at.% in as-quenched state. A slight increase in SAXS intensity and appearance of a rather broad maximum in the SAXS curve for $x = 5$ at.% point the presence of a chemical heterogeneity. In the SAXS curves for $x = 10$ and 15 at.% distinct interference maxima were observed with the position of the maxima at $q_{\text{max}} \approx 0.4 \text{ nm}^{-1}$ and $q_{\text{max}} \approx 0.23 \text{ nm}^{-1}$, respectively. Presence of such a distinct maximum in SAXS curve implies the presence of compositional fluctuations with a dominant correlation length. For the correlation length ζ values of about $\zeta = 16 \text{ nm}$ for $x = 10$ at.% and $\zeta = 27 \text{ nm}$ for $x = 15$ at.% are determined from the relationship $\zeta = 2\pi/q_{\text{max}}$ with the position of the maximum q_{max} . Determined values of the correlation length ζ are in good agreement with the inter-cluster distance determined from corresponding TEM microstructures (Fig. 4.32b). The increases in

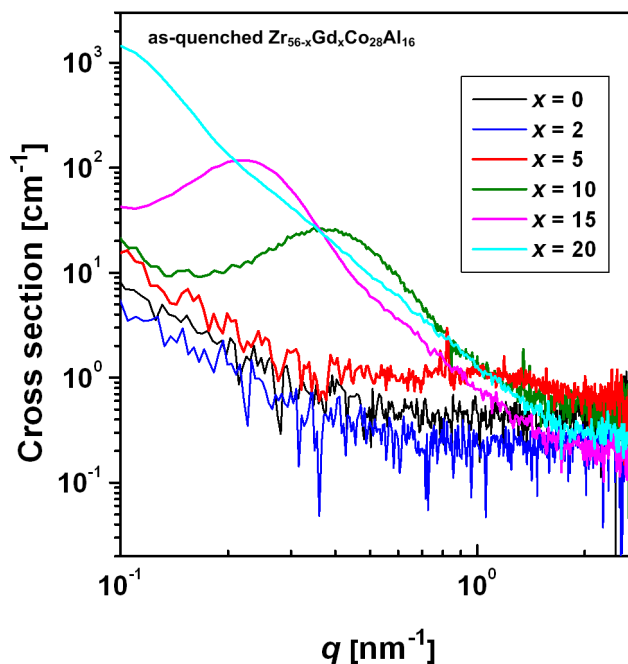


Figure 4.35: SAXS curves of as-quenched $\text{Zr}_{56-x}\text{Gd}_x\text{Co}_{28}\text{Al}_{16}$ glassy ribbons ($0 \leq x \leq 20$).

correlation length and SAXS intensity with Gd content could also be interpreted as being related to that the compositional fluctuation is enlarged in amplitude and width for higher Gd content. On the other hand, a monotonic SAXS curve without particular maximum observed from $x = 20$ at.%, represents a polydisperse character of the microstructure which is in accordance with TEM result (Fig. 4.32c). In order to clarify the heterogeneities as a result of the phase separation in microstructures for the alloys with small amount of Gd, alternatively the atom probe tomography (APT) was performed. The reconstructed 3-dimensional elemental maps of the $\text{Zr}_{51}\text{Gd}_5\text{Co}_{28}\text{Al}_{16}$ and $\text{Zr}_{46}\text{Gd}_{10}\text{Co}_{28}\text{Al}_{16}$ glasses in the as-quenched state are shown in Fig. 4.36. Chemical compositions of about $\text{Zr}_{51}\text{Gd}_5\text{Co}_{27}\text{Al}_{17}$ for $x = 5$ and $\text{Zr}_{46}\text{Gd}_{10}\text{Co}_{27}\text{Al}_{17}$ for $x = 10$, respectively, were derived from the counted total number of atoms from the APT data. These values are in good agreement with the nominal composition of the alloys. A random distribution of the Gd-rich clusters throughout the sample volume, with size of about 4 nm for $x = 5$ and 7 nm for $x = 10$, respectively, is clearly visible in Fig. 4.36. The spatial distribution of Gd-rich clusters is distinguished by dark-yellow iso-concentration surfaces for concentration of Gd: 9 at.% for $x = 5$ and 30 at.% for $x = 10$, respectively. These values were chosen from the half maximum of the Gd concentration profiles (Fig. 4.37). The used values are arbitrary to

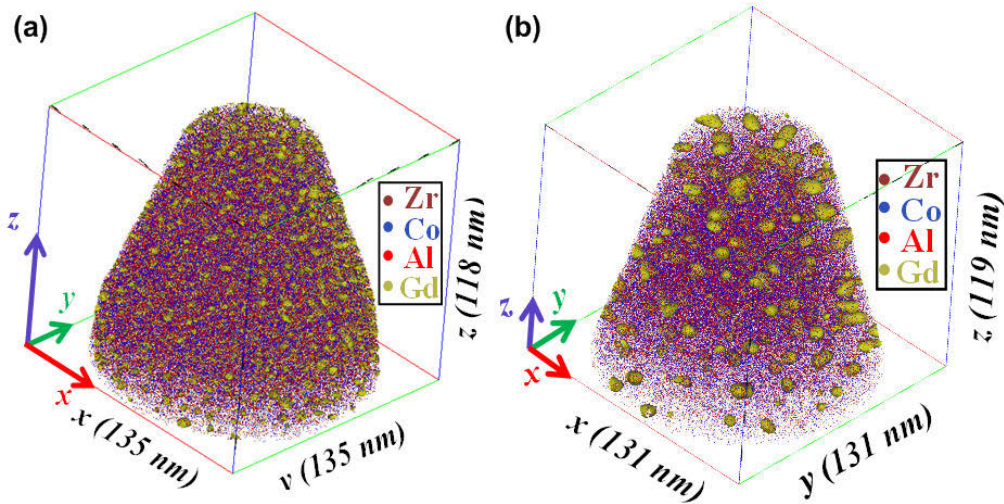


Figure 4.36: Spatial distribution of constituent elements as analyzed by APT. (a) $Zr_{51}Gd_5Co_{28}Al_{16}$ and (b) $Zr_{46}Gd_{10}Co_{28}Al_{16}$ glasses in the as-quenched state.

a certain extent due to the continuous variation of concentration between the Gd clusters and matrix. For the as-quenched $Zr_{51}Gd_5Co_{28}Al_{16}$ glass, the microstructure consisting of Gd-rich clusters derived from APT raises an inconsistency in microstructure compared to an almost homogeneous microstructure of the TEM image shown in Fig. 4.32a. This is obviously due to that the size of the heterogeneities is very small and the concentration fluctuations are too weak to be seen by TEM investigation. The corresponding concentration profiles through a path of matrix-cluster-matrix along a cylinder of 2 nm in diameter and about 8 nm in length are shown in Fig. 4.37. The interface between the cluster and the surrounding matrix exhibits a continuous element distribution. The concentration profiles clearly demonstrate that Gd enrichment at the middle of the profiles is accompanied by a simultaneous depletion of other three elements Zr, Co and Al. As compared in Fig. 4.37, the higher Gd content is, the larger the amplitude of compositional fluctuations and the size of Gd-enriched clusters are.

In order to characterize the microstructure of the whole volume of the samples in detail, the proximity method averaging interfacial properties over a predefined surface irrespective of its convexity [113] was applied. The proximity histograms of the as-quenched $Zr_{51}Gd_5Co_{28}Al_{16}$ and $Zr_{46}Gd_{10}Co_{28}Al_{16}$ glasses are shown in Fig. 4.38. The curves in the proximity histograms represent the average spatial concentration distribution for each constituent element of at least 50 clusters and their surroundings. The Gd concentration profiles in Fig. 4.38 show a deficiency of Gd at the interface between the cluster and the surrounding matrix. This indicates that the Gd-rich clusters are developed

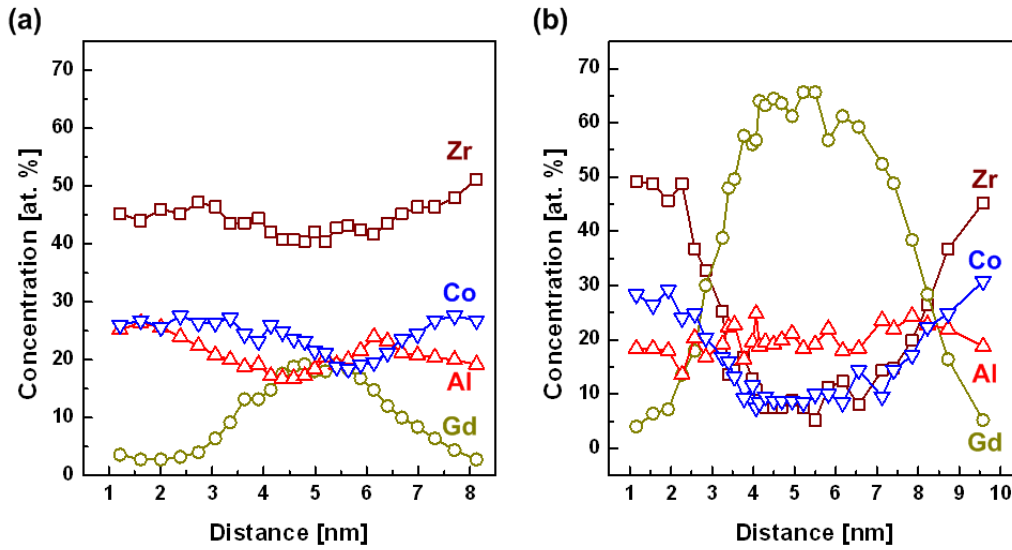


Figure 4.37: Concentration depth profiles of (a) $Zr_{51}Gd_5Co_{28}Al_{16}$ and (b) $Zr_{46}Gd_{10}Co_{28}Al_{16}$ glasses from selected cylinders of 2 nm diameter.

by an up-hill diffusion of Gd atoms from the surrounding into the clusters accompanied by depletion of the other constituent elements. These factors provide direct evidence for the spinodal character of the decomposition. A cluster size of about 3.9 nm for $x = 5$ and 6.9 nm for $x = 10$ is also estimated by taking the full width of half maximum value of the Gd concentration curve. The averaged chemical compositions of the Gd-rich clusters are measured to be $Zr_{46}Gd_{21}Co_{18}Al_{15}$ for $x = 5$ and $Zr_{17}Gd_{53}Co_{12}Al_{18}$ for $x = 10$, respectively. Table 4.10 summarizes the values of cluster size, number density and cluster composition as well as the composition of the surrounding matrix.

Table 4.10: Comparison of microstructural parameters calculated by proximity histograms. Inter-cluster distances are also estimated using values of cluster number densities.

$Zr_{51}Gd_5Co_{28}Al_{16}$	As-quenched				
	Size (nm)	Zr	Gd	Co	Al
Gd-Cluster	3.8	38.2	25.6	21.1	15.1
Matrix		50.4	5.4	26.7	17.5
Cluster density	0.0017 nm ⁻³				
Inter-cluster distance	8.4 ± 0.5 nm				
$Zr_{46}Gd_{10}Co_{28}Al_{16}$	As-quenched				
	Size (nm)	Zr	Gd	Co	Al
Gd-cluster	6.9	3.7	70.3	7.1	18.9
Matrix		48.5	6.2	28.5	16.8
Cluster density	0.0002 nm ⁻³				
Inter-cluster distance	17 ± 1 nm				

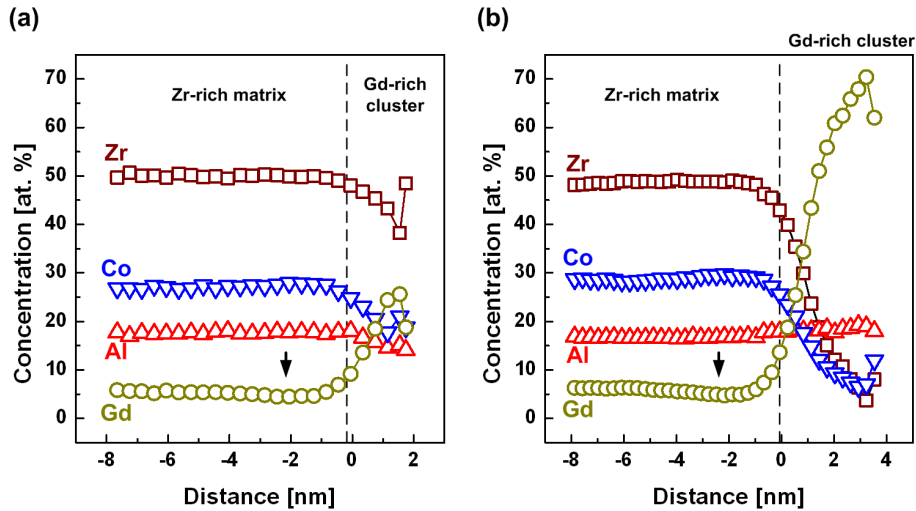


Figure 4.38: Proximity histograms for (a) $Zr_{51}Gd_5Co_{28}Al_{16}$ and (b) $Zr_{46}Gd_{10}Co_{28}Al_{16}$ glasses in the as-quenched state. A statistical average of the element compositions within the Gd-enriched clusters and their surrounding matrix is presented from the analysis of more than 50 clusters.

4.2.3.2 *In situ* SAXS/WAXS investigation

The SAXS curves of the $Zr_{56}Co_{28}Al_{16}$ glass obtained at different temperatures upon heating together with simultaneously recorded WAXS patterns (inset in the upper right corner) are shown in Fig. 4.39a. A homogeneous glassy structure in as-quenched state is revealed by a very low intensity of the SAXS curve as shown by a dashed line ($T = 300$ K). The very low intensity of SAXS curves remains unchanged up to a temperature of $T = 743$ K. The diffuse character of the corresponding WAXS patterns up to $T = 743$ K (inset) also reflects the preservation of the glassy structure. The additional SAXS intensity distributed over a broad q -range is observed at $T = 753$ K. We also observe a weak increase of the WAXS intensity which means the decomposition here is caused by nano-crystallization. The increase in intensity accompanied by a decrease in width can be termed as sharpen. The temperature dependence of the half width of diffuse maxima in WAXS patterns is shown in Fig. 4.39b. A growth of the nano-crystals is reflected by drastic decrease in the width at the

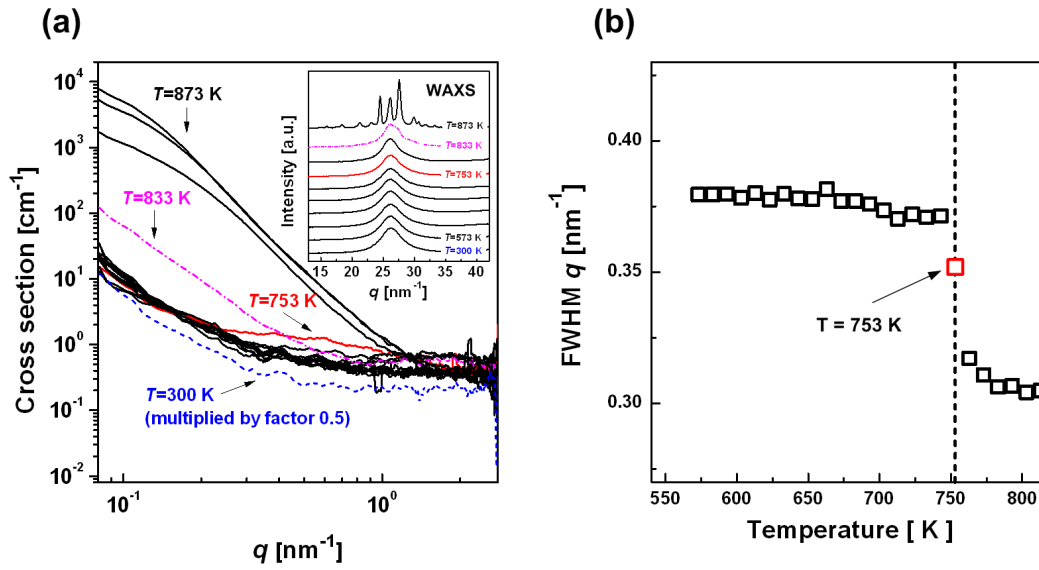


Figure 4.39: (a) *In situ* SAXS and WAXS (inset) at different temperatures for $Zr_{56}Co_{28}Al_{16}$ glass. (b) Temperature dependence of full width at half maximum for the corresponding WAXS patterns.

temperature range of $T = 753 - 763$ K. At $T = 833$ K the SAXS intensity of the $Zr_{56}Co_{28}Al_{16}$ glass distinctly increases (dash-dotted line) due to crystallization and growth. A typical thermal behavior of monolithic metallic glass can be derived from the SAXS/WAXS results for the $Zr_{56}Co_{28}Al_{16}$ glass which is in accordance with the DSC results. Note that the SAXS curves for room temperature ($T = 300$ K) in Fig. 4.39 and 4.40 are multiplied by factor of 0.5 for better visibility.

In order to compare the temperature dependence of structural evolution for alloys with different Gd addition, *in situ* SAXS and corresponding WAXS patterns for $Zr_{56-x}Gd_xCo_{28}Al_{16}$ ($x = 2, 5$ and 10) are shown in Fig. 4.40. For $x = 2$, a similar behavior to the $Zr_{56}Co_{28}Al_{16}$ glass was observed. The addition of 2 at.% Gd only affects the glass transition and crystallization temperature. For $x = 5$ (shown in Fig. 4.40b and e), a low SAXS intensity is also observed for the as-quenched ribbon and is retained up to $T = 673$ K. However, a completely different behavior of the SAXS is observed for higher temperatures. A weak interference maximum at $q \approx 0.8$ nm⁻¹ is observed at $T = 693$ K. As mentioned above, such an interference maximum is the result of the presence of compositional fluctuations with a dominant correlation length in the sample. A correlation length of $\zeta \approx 8$ nm is estimated from the relationship $\zeta = 2\pi/q_{max}$. The intensities of the

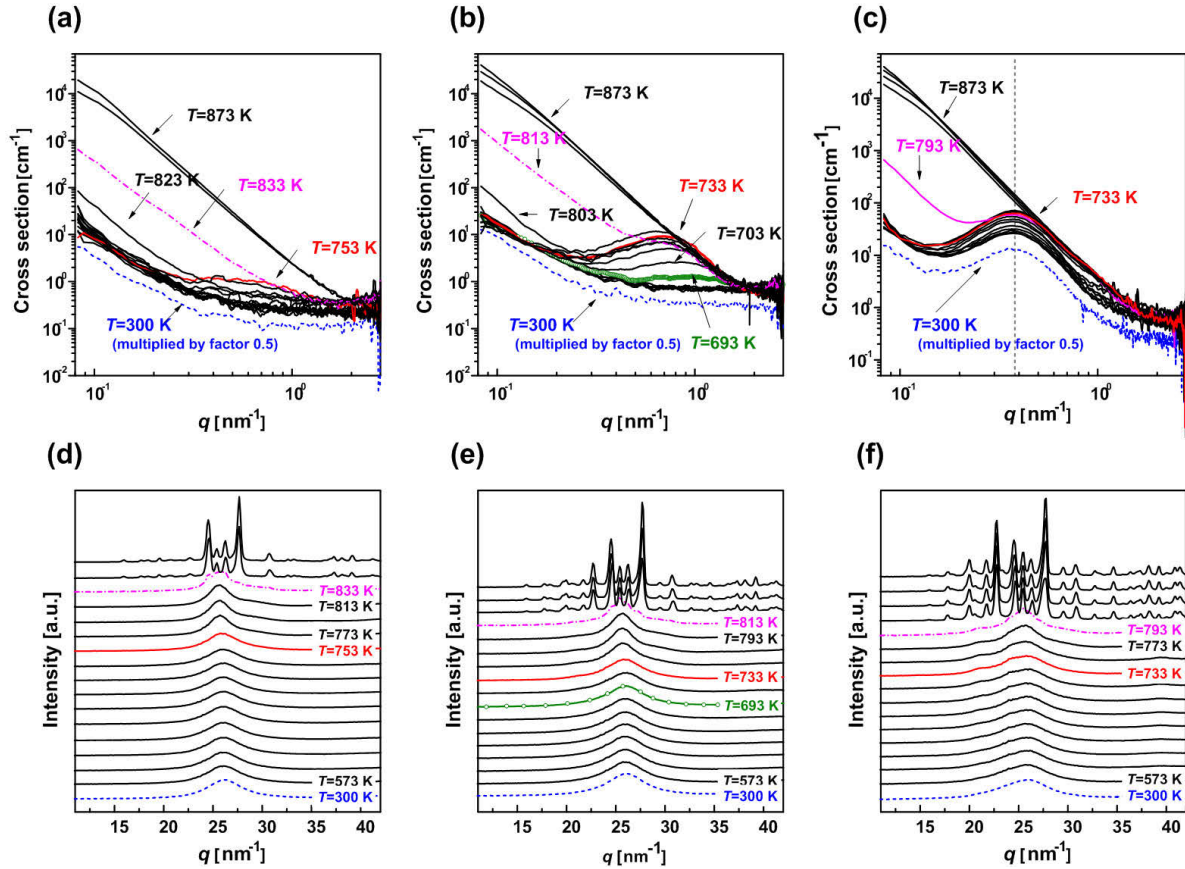


Figure 4.40: *In situ* SAXS (a-c) curves and corresponding WAXS (d-f) curves of $Zr_{56-x}Gd_xCo_{28}Al_{16}$ ($x = 2, 5$ and 10) glasses at room temperature (dashed curves) and elevated temperatures upon stepwise heating (10 K or 20 K steps) from $T = 573$ K up to $T = 873$ K. (a and d) $Zr_{54}Gd_2Co_{28}Al_{16}$ glass; (b and e) $Zr_{51}Gd_5Co_{28}Al_{16}$ glass; (c and f) $Zr_{46}Gd_{10}Co_{28}Al_{16}$ glass.

maxima increase and the position of the maxima slightly shift to lower scattering angle $q \approx 0.7 \text{ nm}^{-1}$ upon further heating to $T = 703$ K. Such behavior is the typical result of the early stage of a spinodal decomposition where the amplitude of compositional fluctuations increases with preserved cluster size in the first place [114]. The development of phase separation prior to crystallization is observed with further heating to $T = 793$ K. The preservation of the glassy structure up to a temperature of $T = 793$ K is also confirmed by diffuse maxima of corresponding WAXS patterns shown in Fig. 4.40e. When crystallization sets in at a temperature of $T = 803$ K the shape and the intensity of the SAXS curves change abruptly. The spinodal character of phase separation is more pronounced in the SAXS curves for $x = 10$. A strong interference maximum at $q \approx 0.4 \text{ nm}^{-1}$ can already be seen in the SAXS curve for the as-quenched ribbon (dashed line in Fig.

4.40c). This suggests that a phase separation was already took place by spinodal decomposition with a dominant correlation length of $\zeta \approx 16$ nm during quenching. This value is in good agreement with the inter-cluster distance estimated from TEM micrographs and the APT results. Upon heating to $T = 783$ K the intensity of the maximum increases whereas the position of the maxima q_{max} remains almost constant. The preserved glassy structure of the ribbon up to $T = 783$ K is also revealed by the diffuse character of corresponding WAXS patterns (Fig. 4.40f). A distinct asymmetric shape is also observed in the WAXS patterns likewise the room temperature XRD and the radial intensity profiles of the SAED patterns are shown. The presence of an additional Gd-rich glassy phase is reflected by additional diffuse maxima around $q \approx 22$ nm⁻¹.

4.3 Magnetic properties of phase separated metallic glasses

Recently, several Gd-based metallic glasses with favourable magnetocaloric effect (i.e. larger magnetic entropy change ΔS_M and larger temperature range of the ΔS_M) such as Gd-Ni ($\Delta S_M \approx 11 \text{ J kg}^{-1}\text{K}^{-1}$ at 130 K, 7 T) [115], Gd-Ni(Co)-Al ($\Delta S_M \approx 11 \text{ J kg}^{-1}\text{K}^{-1}$ at 80 - 100 K, 7 T) [116], Gd-Al-Co-Zr ($\Delta S_M \approx 9.4 \text{ J kg}^{-1}\text{K}^{-1}$ at 93 K, 5 T) [117] and Gd-Fe-Co-Al ($\Delta S_M \approx 5 \text{ J kg}^{-1}\text{K}^{-1}$ at 170 K, 5 T) [108] systems have been reported as promising candidates for magnetic refrigeration. In this section the investigations will be presented to study the influence of phase separation, The investigated alloys are i) a series of $\text{Gd}_{55-x}\text{Hf}_x\text{Co}_{25}\text{Al}_{20}$ ($x = 0, 10, 20, 27.5, 35, 45$ and 55 at.%) ribbons and ii) $\text{Gd}_{60-x}\text{Ti}_x\text{Co}_{30}\text{Al}_{10}$ ($x = 0$ and 30 at.%) ribbons. The structure formation and phase separation in these alloys are already introduced in previous chapters.

4.3.1 Magnetic properties of Gd-Hf-Co-Al alloys

The normalized temperature dependence of magnetization curves $M-T$ of the Gd-Hf-Co-Al glasses measured in a field of 100 Oe is shown in Fig. 4.41. The field dependence of magnetization loops $M-H$ measured at $T = 10$ K are also given in the inset. Magnetic ordering transition from paramagnetic to ferromagnetic is observed below $T = 110$ K for all Gd-containing glasses ($x \leq 45$ at.%), whereas the ternary $\text{Hf}_{55}\text{Co}_{25}\text{Al}_{20}$ glass ($x = 55$ at.%) remains paramagnetic in the whole temperature range of measurement. The Curie temperature T_{Curie} is determined as the temperatures where the absolute values of the first derivative dM/dT are maximum. With increase of Hf addition T_{Curie} slightly shifts to lower temperature range. The soft magnetic properties of the alloys were revealed by small coercivities ($H_c \leq 100$ Oe) in the $M-H$ loops. The values of saturation magnetization were determined as the magnetization where applied field is 9 T at $T = 10$ K as shown in Fig. 4.42a. All alloys begin to saturate at fields of approximately 2 T. The higher Gd content, the higher the value of saturation magnetization σ_s is. The values of T_{Curie} and σ_s are summarized together with the volume fractions of Gd-rich phase in Table 4.11. The values of σ_s in applied field of 9 T are plotted as a function of alloy composition in Fig. 4.42b. The error bars in x- and y-direction correspond to errors in sample mass and deviations of

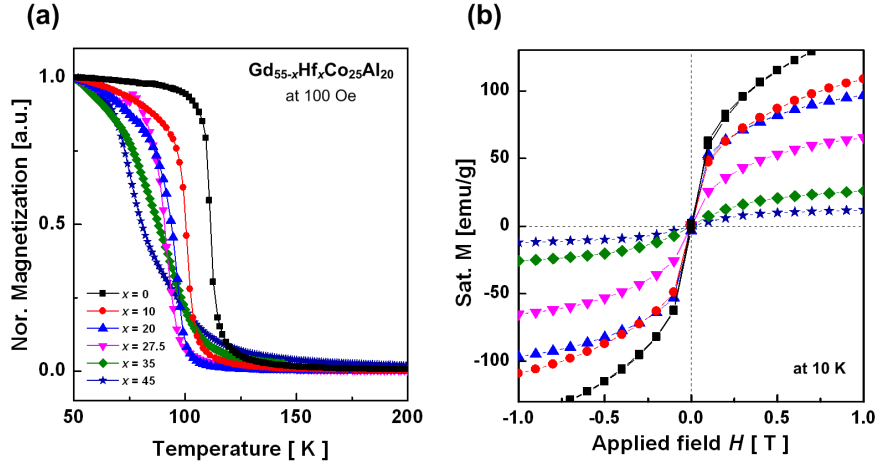


Figure 4.41: (a) Temperature dependence of the magnetization curves (M - T) of Gd_{55-x}Hf_xCo₂₅Al₂₀ ($x = 0, 10, 20, 35$ and 45 at.%) ribbons in an applied field of 100 Oe and (b) magnetic field dependence of magnetization (M - H) loops measured at 10 K.

chemical composition as verified by EDX measurements, respectively. Assuming that exclusively the Gd atoms contribute to the overall magnetization with $7 \mu_B$ per Gd atom [118,121], where μ_B is the Bohr magneton, the calculated hypothetical saturation magnetization for the alloy compositions are also given in Fig. 4.42b for comparison. As can be seen in Fig. 4.42b, the measured values of σ_S for all compositions coincides quite well with the calculated hypothetical total moment suggesting that the saturation magnetization indeed originates predominantly from the Gd atoms and that decomposition processes and consequent microstructure have only minor effects on the saturation magnetization.

Table 4.11: Volume fractions of the Gd-rich phases estimated from XRD data and image analysis with SEM micrographs (see Fig. 4.25 and Fig. 4.27). The values of Curie temperatures (T_{Curie}) and saturation magnetization (σ_S) are also given.

Alloy composition	Vol. % (XRD)	Vol. % (Micrograph)	T_{Curie} (K)	σ_S (emu/g) at 10K, 9T
Gd ₅₅ Co ₂₅ Al ₂₀	100	100	110.9	207
Gd ₄₅ Hf ₁₀ Co ₂₅ Al ₂₀	77 ± 4	82 ± 2	100.1	160
Gd ₃₅ Hf ₂₀ Co ₂₅ Al ₂₀	63 ± 3	66 ± 1	96.5	140
Gd _{27.5} Hf _{27.5} Co ₂₅ Al ₂₀	36 ± 2	45 ± 3	91.6	102
Gd ₂₀ Hf ₃₅ Co ₂₅ Al ₂₀	23 ± 3	31 ± 4	97.7	57
Gd ₁₀ Hf ₄₅ Co ₂₅ Al ₂₀	8 ± 2	15 ± 4	75.2	26
Hf ₅₅ Co ₂₅ Al ₂₀	0	0	-	0.04

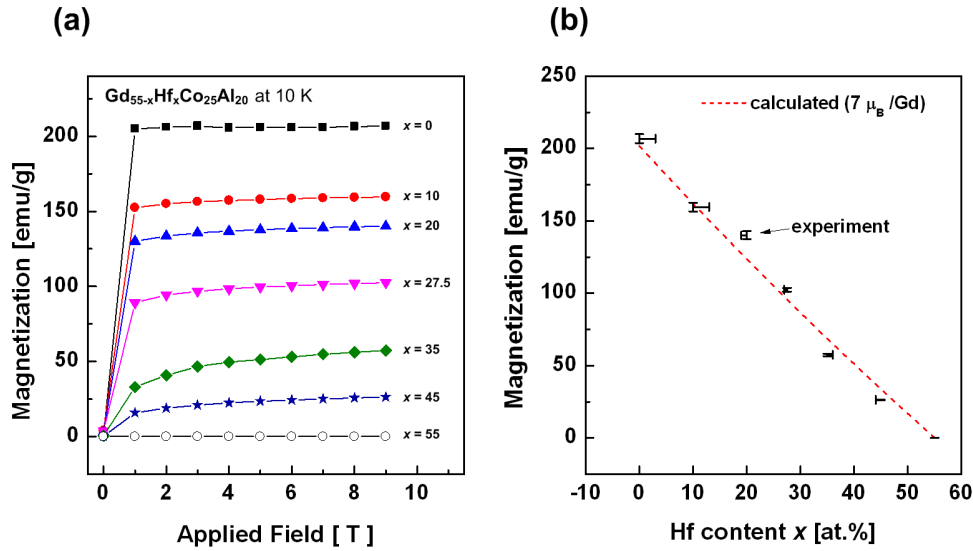


Figure 4.42: (a) Magnetic field dependence of magnetization curves ($M-H$) measured at $T = 10$ K. (b) Composition dependence of saturation magnetization (σ_s) obtained from experiments (scatters) and calculation (dashed line).

The magnetic moment of a Gd atom stemming from the inner $4f$ electrons is comparably large and is not affected by hybridization due to alloying in the first place [118,119,120]. Therefore the overall amount of Gd atoms within the sample (i.e. irrespective of the phase where they belong to) simply determines the saturation magnetization. However, in Gd-Co binary system, the Co atoms also possess a magnetic moment strongly depending on the Gd-Co ratio and couple anti-ferromagnetically with the Gd moments [121,122]. In the phase separated alloys, the Gd-Co ratio exists in both Gd-rich and Hf-rich phase separately and vary depending on the nominal Gd-Hf ratio. This could be responsible for the slight deviations in Fig. 4.42b. Nevertheless, properties in binary alloy systems can not simply be transferred to such multi-component systems and moreover, it is still not clear that what and how the partial crystallization contributes to this issue.

As compared in Table 4.12, as the Gd-Co ratio in the nominal composition decreases the Curie temperature T_{Curie} decreases (see Table 4.11) and the ratio in Gd-rich glassy phase increases. This is in agreement with the results for binary Gd-Co alloys that also show a decreasing T_{Curie} with increasing Gd-Co ratio. In addition, the composition of the Gd-rich glassy phase in $x = 45$ was determined to be $\text{Gd}_{65.6}\text{Hf}_{0.5}\text{Co}_{0.5}\text{Al}_{33.4}$ (i.e. it exhibits essentially a binary Gd-Al composition). The determined T_{Curie} for $x = 45$ fits very well with that of binary Gd-Al alloys of the similar composition [123].

Table 4.12: Chemical compositions of Gd-rich phase and Hf-rich phase for $x = 0, 10, 27.5, 45$ and 55 at.% determined by EDX analysis. Standard deviations are also given.

Alloy composition	Gd-rich phase		Hf-rich phase	
	Average composition (Std. Dev.)		Average composition (Std. Dev.)	
Gd ₅₅ Co ₂₅ Al ₂₀	Gd _{51.3} Co ₂₈ Al _{20.7}	(0.25)	-	
Gd ₄₅ Hf ₁₀ Co ₂₅ Al ₂₀	Gd _{55.1} Hf _{1.7} Co _{25.8} Al _{17.4}	(1.25)	Gd _{7.4} Hf _{41.8} Co _{42.2} Al _{8.6}	(2.30)
Gd _{27.5} Hf _{27.5} Co ₂₅ Al ₂₀	Gd _{57.9} Hf _{3.9} Co _{16.7} Al _{21.5}	(1.58)	Gd _{6.4} Hf _{46.8} Co _{35.8} Al ₁₁	(1.19)
Gd ₁₀ Hf ₄₅ Co ₂₅ Al ₂₀	Gd _{65.6} Hf _{0.5} Co _{0.5} Al _{33.4}	(0.53)	Gd _{2.8} Hf _{52.1} Co _{30.3} Al _{14.8}	(0.43)
Hf ₅₅ Co ₂₅ Al ₂₀	-		Hf _{49.9} Co _{25.3} Al _{24.8}	(0.66)

4.3.2 Magnetic properties of Gd-Ti-Co-Al alloys

The T_{Curie} of $\text{Gd}_{60-x}\text{Ti}_x\text{Co}_{30}\text{Al}_{10}$ ($x = 0$ and 30 at.%) ribbons determined from the temperature dependence of magnetization M - T curves shown in Fig. 4.43, are rather low compare to that of pure Gd ($T_{\text{Curie}} \approx 300$ K). The obtained values of T_{Curie} for the ribbons are summarized in Table 4.13. In order to determine the saturation magnetization σ_s , the ribbons were measured up to 5 T at 10 K. The M - H curves are shown in Fig. 4.44. The alloys exhibit a soft magnetic behavior with small coercivities ($H_c < 100$ Oe). The values of ordered magnetic moment μ_m per formula unit for the alloys are calculated from the σ_s . As summarized and compared in Table 4.13, the obtained values of μ_m are in good agreement with the calculated magnetic moment $\mu_m^{\text{calc}}(\text{Gd})$ under the assumption that only the Gd atoms would constantly contribute ($\mu_{\text{Gd}} = 7 \mu_B/\text{atom}$) to the saturation magnetization [118,120]. Despite the fact that the Co atoms principally can also possess magnetic moments [121], the result in this work, i.e. the measured magnetic moment per formula unit can solely be explained by only the magnetic moment of the Gd atoms reveals that the potential magnetic moments of the Co atoms are quenched due to alloying in the investigated multi-component alloys. Therefore the occurrence of liquid-liquid phase separation prior to solidification, and the consequent microstructures do not have

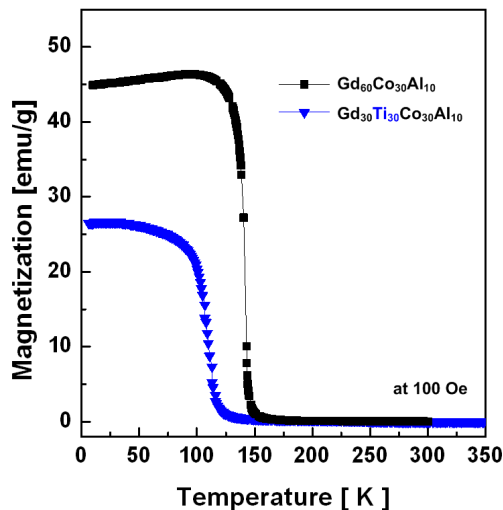


Figure 4.43: Temperature dependence of the magnetization curves M - T under an applied field of 100 Oe for $\text{Gd}_{60-x}\text{Ti}_x\text{Co}_{30}\text{Al}_{10}$ ($x = 0$ and 30 at.%) ribbons.

remarkable influences on that magnetic property.

Nevertheless, the Gd concentration and the phase morphology has still to be taken into account when analyzing the evolution of T_{Curie} due to that the Co or Al addition in Gd-Co and Gd-Al binary systems induces a significant decrease of T_{Curie} by a modified magnetic coupling mechanism [122,123]. Since the phases with low Gd contents do not play an important role in magnetization in the investigated temperature range, the magnetic transitions have to be ascribed exclusively to the Gd-rich phases which exhibit similar compositions to the $\text{Gd}_{60}\text{Co}_{30}\text{Al}_{10}$ glass. Further, the hypothetical effective magnetic moment $\mu_{\text{eff}}^{\text{calc}}(\text{Gd})$ was calculated. If only the Gd atoms with spin quantum number $S_{\text{Gd}} = 7/2$ and atomic fraction X_{Gd} would contribute (gyromagnetic factor $g = 2$):

$$\mu_{\text{eff}}^{\text{calc}}(\text{Gd}) = g \sqrt{x_{\text{Gd}} S_{\text{Gd}} (S_{\text{Gd}} + 1)} \mu_B, \quad (4.11)$$

the calculated values (see Table 4.13) are only slightly smaller than the experimentally determined effective magnetic moments, indicating the formation of only very few high spin units already present at higher temperature.

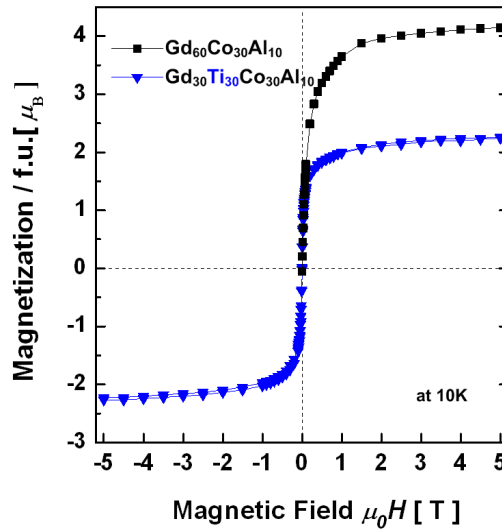


Figure 4.44: The field dependence of magnetization per formula unit $\mu_m(H)$ at 10 K for the $\text{Gd}_{60-x}\text{Ti}_x\text{Co}_{30}\text{Al}_{10}$ ($x = 0$ and 30 at.%) ribbons.

Chapter 5: Discussion of structure formation

This chapter discusses and summarizes the results obtained in the previous chapter. An attempt is made to explain the observations on the structure formation with a specific focus on the mechanisms for phase separation and corresponding microstructure developments.

The general behavior of the microstructural development upon liquid-liquid phase separation is described by the Cahn-Hilliard-Cook (CHC) theory [134]. We consider a binary phase diagram with a stable miscibility gap and a corresponding free energy curve at a certain temperature T_1 as shown in Fig 5.1. For case (i), an alloy with composition X_0 at a high temperature T_0 is stable as a single liquid phase and the composition is homogeneous and identical to its nominal composition. If the alloy is quenched to lower temperature T_1 , i.e. the alloy melt enters into the miscibility gap, the liquid will initially sustain the chemical homogeneity with the free energy G_0 on the G_{mix} curve in Fig. 5.1b where no nucleation barrier exists to overcome. Since any small compositional changes will result in reduction of the total free energy of the system. The unstable alloy will immediately exhibit compositional fluctuations with small amplitudes that develop A-rich and B-rich region. The interface between the two regions is not sharp but very diffuse as shown in Fig. 5.2a [24]. Then, the spontaneous and continuous growth of the fluctuations will be followed via *up-hill* diffusion until the equilibrium composition X_1 and X_2 are reached. The fluctuations increase exponentially with time, i.e. the decomposition process from the early to final stage progresses very rapidly [24]. This decomposition process can take place for any alloy compositions between two inflection points (solid circles in Fig. 5.1b) on the free energy curve where the free energy curve has a negative curvature. Therefore, the locus of the inflection points where $(d^2G/dX^2)T \equiv 0$, develops an inner region of the miscibility gap as distinguished by dashed line in Fig. 5.1a. This boundary of the unstable region is known as the *spinodal line* and the type of decomposition described above is referred to as *spinodal decomposition*. For case (ii), on the other hand, if an alloy with composition lying on outside of the spinodal line, X_0' for example, quenched from the high temperature T_0 , to lower temperature T_1 , the alloy is in a metastable state and any small compositional changes will result in an increase in the total free energy of the system,

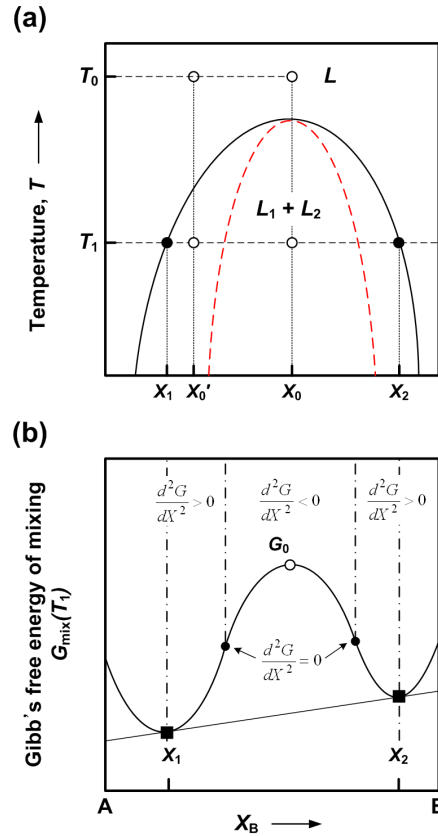


Figure 5.1: (a) Miscibility gap of a binary A - B alloy. The two liquid region L_1+L_2 is subdivided by spinodal curve (dashed in red colour). (b) Corresponding free energy curve at T_1 as a function of composition.

i.e. there is a nucleation barrier. The free energy for this case can only be lowered if decomposition process undergoes the formation of nuclei with a sufficiently large compositional difference with the matrix and subsequent growth. As illustrated in Fig. 5.2b, this decomposition process, therefore, takes place via normal *down-hill* diffusion with sharp phase interface and constant composition of the precipitates X_2 . This decomposition process is referred as a *nucleation and growth* mechanism. This type of phase separation can occur for any alloy compositions where the free energy curve has a positive curvature, i.e. $d^2G/dX^2 > 0$. And the locus of bitangent points where the free energies are minimum (solid squares in Fig. 5.1b), defines the boundary of the miscibility gap dividing regions of single liquid phase and two liquid phases. This outer boundary is known as a *binodal line* and the temperatures on the curve are the critical temperature of a miscibility gap T_c . At any temperature, the relative amounts of the two separated phases are determined by the lever rule with this binodal line. Thus, if an alloy system has a positive enthalpy of mixing $\Delta H_{\text{mix}} > 0$ and corresponding miscibility gap, phase separation can take place by either by

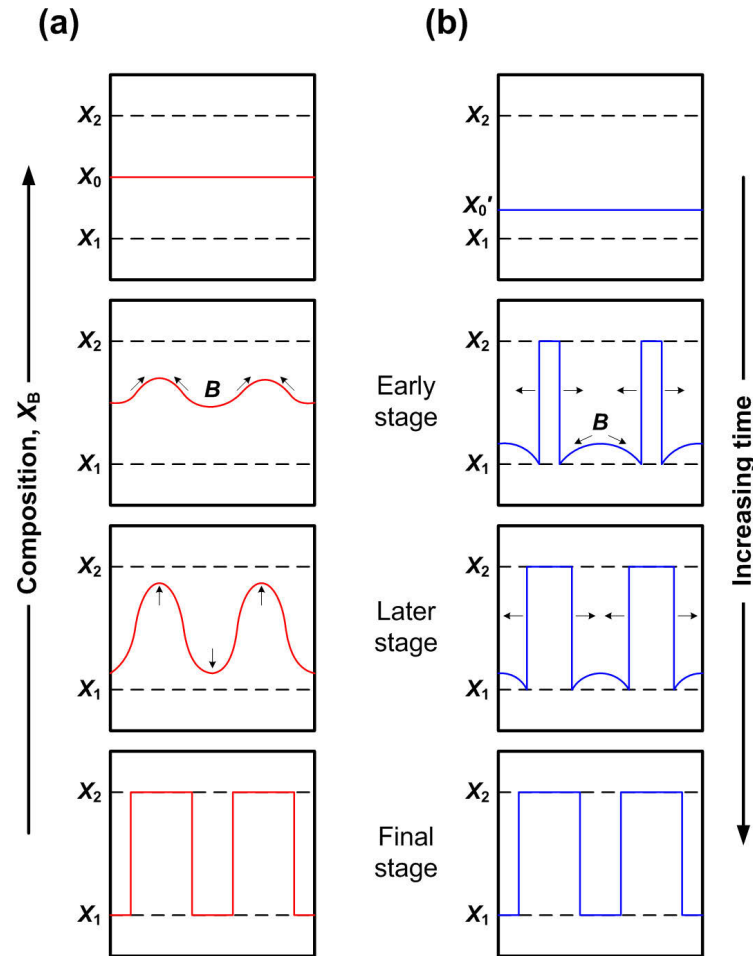


Figure 5.2: Schematic illustrations of composition profiles at increasing times in a binary alloy quenched into (a) the *spinodal* region and (b) *nucleation and growth* region of a miscibility gap [114].

a *nucleation and growth* mechanism or a *spinodal decomposition* mechanism depending on the alloy composition and undercooling condition as well. After reaching the final stage of decomposition as shown in Fig. 5.2, the resultant morphologies of decomposition are similar and allow no conclusion to be drawn with respect to the decomposition mechanisms [114]. By analogy, the miscibility gap plays important role not only on the occurrence of phase separation but also on the determination of material characteristics. The morphological development of phase separation has been the subject of important theoretical works [124,125,126,127,128] and experimental works in the field of oxide [2-3] and polymer glasses [4,5,129,130,131].

It is often assumed that the *nucleation and growth* leads to a morphology of well dispersed droplets (Fig. 5.3a), while the *spinodal decomposition* produces a so-called interconnected structure (also known as a network or worm-like structure, Fig. 5.3b).

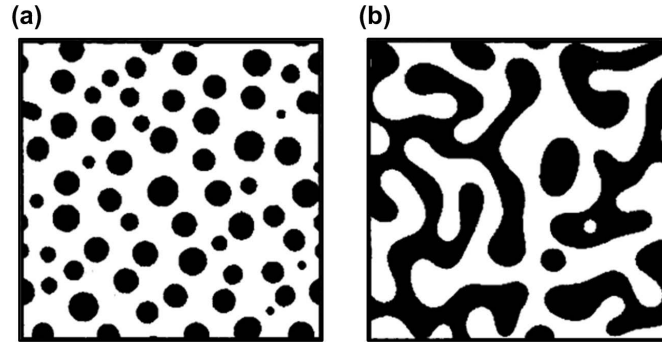


Figure 5.3: Schematic microstructure of a two-dimensional system undergoing phase separation. Different volume fraction Φ develops a morphology of (a) well dispersed droplets ($\Phi \approx 0.5$) and (b) interconnected structure ($\Phi \approx 0.5$). Images were obtained by numerical calculation with Cahn-Hilliard equation and adopted from Ref. [132].

However such identification is ambiguous and may be misleading. Also as experimentally demonstrated and discussed in this chapter, a critical volume fraction so-called percolation threshold exists where the interconnected structure appears firstly [132]. Furthermore, it is confirmed that the transition between both morphologies, interconnected structure and well-dispersed droplets, can also be observed as a function of temperature and time by computational simulation and experiments [114].

In general, the single roller melt spinning technique offers the highest cooling rate at the wheel side of a ribbon whereas a relatively low cooling rate is offered at the air side. Thus, there is a local cooling rate gradient depending on the distance from the copper wheel. The overview microstructure of the ribbon cross-section for $\text{Gd}_{27.5}\text{Hf}_{27.5}\text{Co}_{25}\text{Al}_{20}$ alloy which has approximately equal volume fractions of two glassy phases is shown in Fig 5.4 (left hand side). The local cooling rate dependence of microstructural evolution in a phase separating metallic glass can be clearly seen from top (wheel side) to bottom (free side). The details of different areas (indicated by dashed squares in the overview) are also presented with enlarged images at right hand side (Fig. 5.4a-d). A very fine interconnected structure with high connectivity is observed from wheel side of the cross-section (Fig. 5.4a) where the cooling is the fastest. As cooling rate decreases, the interconnected structure loses its connectivity (Fig. 5.4b), and the typical droplet-like structure is then developed (Fig. 5.4c). At this stage, a secondary phase separation already took place and the corresponding precipitates are visible. The coalescence of liquid droplets and coarsening can be seen by comparison of Fig. 5.4c and d. The cooling rate dependence of microstructure evolution can also be interpreted by the

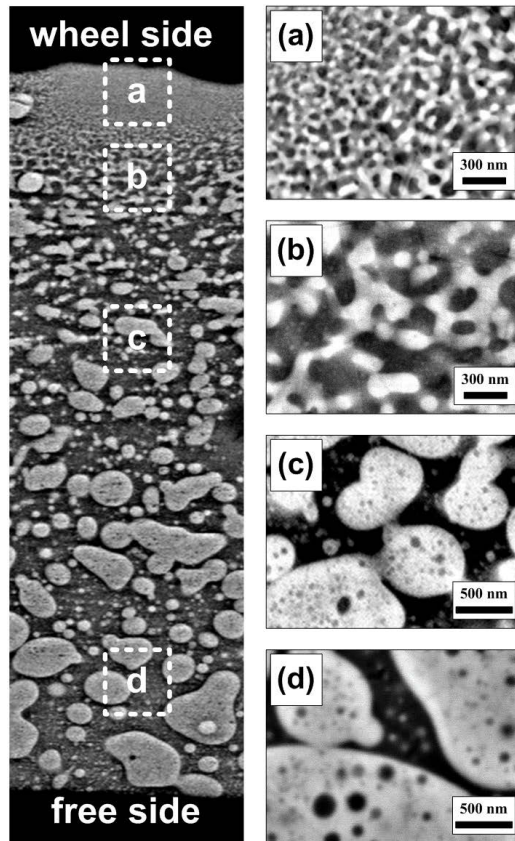


Figure 5.4: SEM micrograph with electron backscatter contrast obtained from the cross section of the $\text{Gd}_{27.5}\text{Hf}_{27.5}\text{Co}_{25}\text{Al}_{20}$ ribbon. Overview of cross section displayed at left hand side shows cooling rate dependence of microstructure evolution. Different areas (a) - (d) indicated by dashed squares in the overview are presented with magnified images at right hand side.

solidification time dependence of the solidification, i.e. a slow cooling rate represents a longer time for solidification and/or vitrification. In this aspect, a very short distance between the areas for Fig. 5.4a and 5.4b, implies that the transition between the interconnected structure and droplet structure accompanied with the loss of the connectivity occurs exponentially in time scale. This experimental observation on microstructure development as a function of local cooling rate (or time) is in good agreement with the results of the Lattice Boltzmann simulation describing a domain growth in a two-dimensional binary immiscible fluid with parameters such as a viscosity, diffusivity and time scale [110].

As mentioned above, the formation of an interconnected structure can be expected when the volume fractions of both phases are approximately equal. Based on the experimental results here, one can conclude that a fine interconnected structure can be

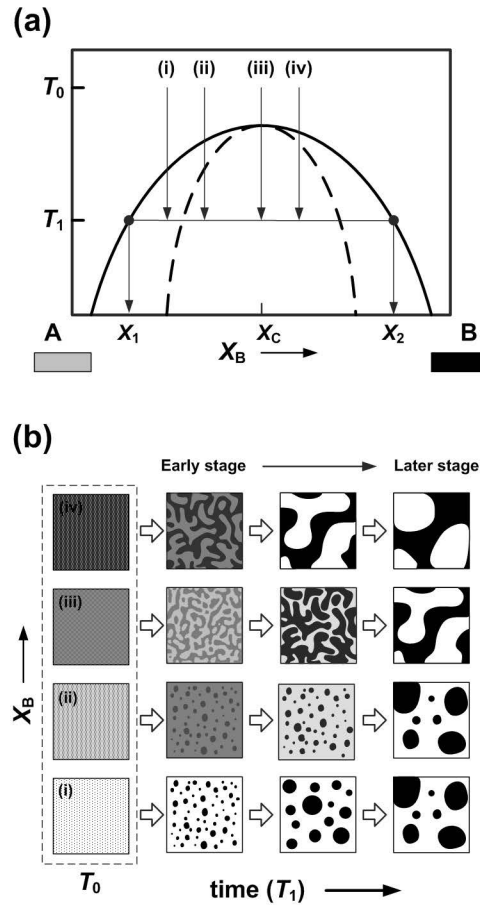


Figure 5.5: (a) Schematic of a miscibility gap in binary A - B system and (b) corresponding sequences of domain evolution during phase separation for different compositions.

formed at the very early stage of phase separation via spinodal decomposition. However, the structure would develop a typical droplet-like structure at the later stage via a conventional coarsening process [114]. Fig. 5.5 schematically illustrates a symmetric miscibility gap of a hypothetical alloy and the corresponding sequences of phase formation during isothermal heat treatment at T_1 as a function of time. Concerning the given compositions (i) to (iv) in a binary A - B system (Fig. 5.5a), if the melts at T_0 is quenched to T_1 and aged, domain evolutions of a phase separating system can be summarized as follows:

For the case of composition (i), when the alloy lies on the metastable region which is outside the spinodal and far away from the critical composition (which corresponds to the maximum on the free energy of mixing curve, i.e., the composition where T_c is maximum), a phase separation takes place via nucleation and growth mode. Since the B atoms are minor in volume for the composition X_i , the B -rich nuclei (shown in black) will

be formed with a very different composition from the A -rich matrix and the consequential sharp interface between the nuclei and the matrix (the compositional differences in Fig. 5.5b are shown by light and shade). In the following intermediate and later stages, a further growth of the nuclei will be occurred via the down-hill diffusion and the coalescence of neighboring clusters until the stable compositions X_1 for the matrix and X_2 for the droplets are reached. Morphology of well dispersed droplets, therefore, will be obtained at the final stage of this phase separation process. Phase separation by the spinodal decomposition mechanism can be described in three successive sequences depending on the composition. For the composition X_{ii} , if the alloy lies on inside spinodal but still away from the critical composition X_C , spinodal decomposition initiates with the formation of very small B -rich clusters within the A -rich matrix. From the morphological aspect, it is similar to the case for the composition X_i . However, in the early stage, the compositional difference is very small and the interface between two phases is diffuse. As described above (see Fig. 5.2a), this compositional fluctuation then exponentially enhances in amplitudes by the *up-hill* diffusion until the composition X_1 and X_2 are reached. Then the clusters will also be coarsened by the growth and the coalescence of neighboring clusters. Hence, at the final stage, morphology of well dispersed droplets may again be obtained [133]. For a symmetric composition X_{iii} where the volume fractions of A -rich and B -rich phases are identical to each other ($\Phi = 0.5$), spinodal decomposition develops the interconnected structure (bicontinuous morphology) in the early stage. In the following intermediate stage, the amplitude and the wavelength of the compositional fluctuation increase with time until the composition X_1 and X_2 are reached. In the later stage, the breakup of the interconnected structure into fragments (interconnected - droplets transition) occurs, and further coarsening and coalescence of separated domains will be followed. For the off-critical composition X_{iv} , in the early stage, the interconnected structure is developed in a similar manner as in the composition X_{iii} . However, the breakup of the interconnected structure occurs much earlier as the composition deviates from the critical composition X_C . The coarsening and coalescence of the domains then develop the morphology of the final product. It should, in addition, be mentioned that there is another feature of morphology in phase separation under the condition of continuous cooling of a melt. As shown in Fig. 5.6, if an alloy with a composition X_0 is quenched from high temperature T_0 into the miscibility gap, the primary phase separation occurs at a certain temperature T_1 and develops a corresponding morphology (see the schematic for the corresponding resultant structure in

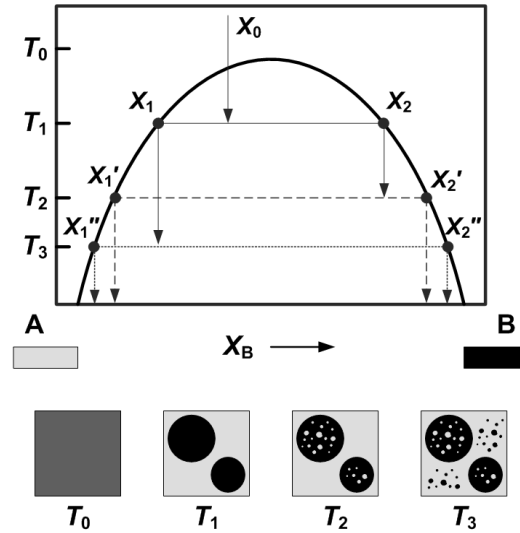


Figure 5.6: Schematic of a miscibility gap and the sequence of domain evolution in a binary A - B system undergoing phase separation and corresponding secondary phase separation during continuous cooling.

Fig. 5.5). With further cooling to a temperature low enough, due to the supersaturation, newly formed phases with composition X_1 and X_2 (they are still in the miscibility gap!) locally undergo phase separation again at the certain temperatures T_2 and T_3 , and develop into relatively small precipitates within the primary phases. This local phase separation is referred as a secondary phase separation (also known as a secondary precipitation). After all, the final morphology of the phase separated alloy strongly depends on the depth of quenching, composition and moment of freezing.

Spinodal mechanism of decomposition in Zr-Gd-Co-Al glass

The *in situ* SAXS curves and corresponding WAXS curves for the $Zr_{51}Gd_5Co_{28}Al_{16}$ ($x_{Gd} = 5$) ribbon obtained from isothermal annealing at two different temperatures $T_{iso} = 693$ K and $T_{iso} = 723$ K as a function of time are shown in Fig. 5.7. The interference maxima intensify whereas the positions of the maxima $q_{max}^{@693\text{ K}} \approx 0.85 \text{ nm}^{-1}$ and $q_{max}^{@723\text{ K}} \approx 0.75 \text{ nm}^{-1}$ remain nearly constant within given time. The diffuse character of corresponding WAXS patterns prove that the phase separation takes place within the glassy state well below crystallization. The time dependence of the SAXS intensities at the position of the maxima is shown in Fig. 5.7c. The semi-logarithmic plot shows that the intensity exponentially increases in the earliest stage of annealing. Later on the increase of

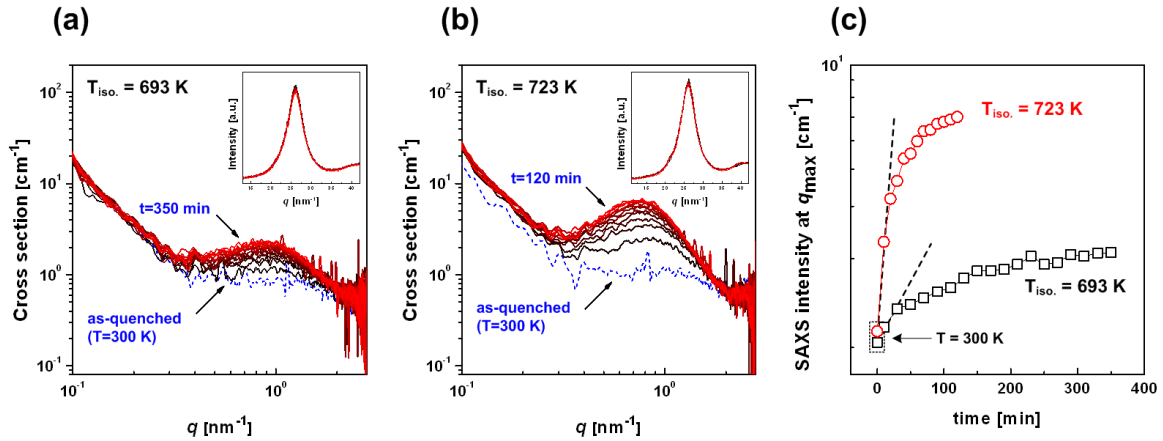


Figure 5.7: *In situ* isothermal SAXS/WAXS curves of $Zr_{51}Gd_5Co_{28}Al_{16}$ glass at (a) $T_{iso} = 693$ K for 350 min; (b) $T_{iso} = 723$ K for 120 min. (c) SAXS Intensities at the position of first maxima as a function of time.

the intensity diminishes and reaches a stationary state. Since both SAXS curves are obtained from the same thermally activated process of decomposition, they can be transformed into each other by a scaling factor. As expected, the decomposition process develops much faster at the higher temperature. The structure development of spinodal decomposition can usually be described by the Cahn-Hilliard theory [134]. Two liquids of an immiscible system spontaneously separate and form domains with growth of coherent composition fluctuations in the initial stage during a spinodal decomposition. As it is predicted by the linear Cahn-Hilliard theory the intensities of the first maximum increase exponentially during the early stage of annealing (see Fig. 5.7c). Afterwards, the growth of the amplitude exhibits a deceleration effect at the later stages of annealing in accordance with Tsakalacos' approximation, which may explain the deviation from the exponential increase of the SAXS intensity [135]. In addition, the observation that the position of the maxima remains constant during isothermal annealing, also suggest a spinodal mechanism of the phase separation.

Nano-crystallization is also a kind of phase separation, however fundamentally different from liquid-liquid phase separation. In general, it is difficult to distinguish which mechanism is present at the early stage, if only a limited set of structural data is available. Despite the difficulty in interpretation, the distinction between these two processes can be seen by comparing the time dependence of the half width of corresponding WAXS patterns under isothermal annealing as shown in Fig. 5.8. The width for the $Zr_{51}Gd_5Co_{28}Al_{16}$ ($x_{Gd} = 5$) remains almost constant upon annealing due to the spinodal character in which increases

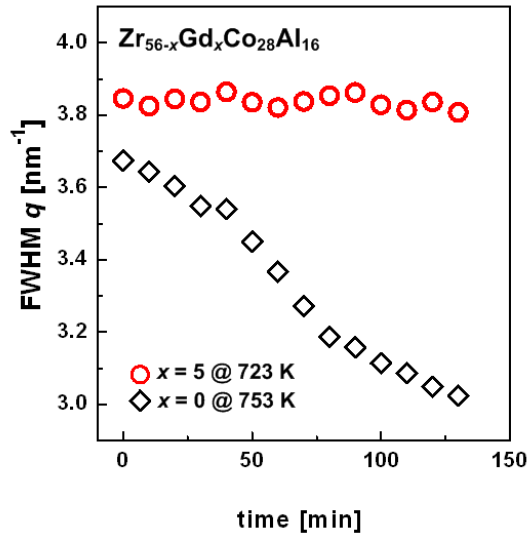


Figure 5.8: The values of full width at half maximum (FWHM) of WAXS patterns depending on the isothermal annealing time for $x_{\text{Gd}} = 0$ and $x_{\text{Gd}} = 5$.

in only the amplitude of the compositional fluctuation is observed, whereas the width for the $\text{Zr}_{56}\text{Co}_{28}\text{Al}_{16}$ ($x_{\text{Gd}} = 0$) exhibits a continuous decrease representing a growth of nano-crystallites.

The spinodal character for the glasses with relatively higher Gd content ($x_{\text{Gd}} = 5$ and $x_{\text{Gd}} = 10$) can also be derived from the microstructure after the isothermal annealing. The proximity diagrams for $x_{\text{Gd}} = 5$ and 10 annealed at $T_{\text{iso}} = 723$ K and $T_{\text{iso}} = 773$ K for 10 minutes are shown in Fig. 5.9. The values of Gd-rich cluster composition, size and density as well as the composition of the surrounding matrix were also calculated and are summarized in Table 5.1 for comparison. For $x_{\text{Gd}} = 5$, it is clearly seen that the amplitude of the compositional fluctuation for the Gd significantly increases after the annealing treatment, whereas the average cluster size and the number density remain almost constant (see Table 5.1). This supports the view that the phase separation for $x_{\text{Gd}} = 5$ undergoes a spinodal decomposition clearly distinguished from the concentration profiles for a nucleation and growth mechanism [114]. On the other hand, no distinct change in the amplitude (see Fig. 5.9b) but only slight changes in cluster composition and size of the clusters were observed from the proximity diagram for $x_{\text{Gd}} = 10$. As addressed above, this is also due to that the as-quenched glass with $x_{\text{Gd}} = 10$ is already in the developed stage of spinodal decomposition. Annealing the glass therefore leads to only slight subsequent growth of the domains.

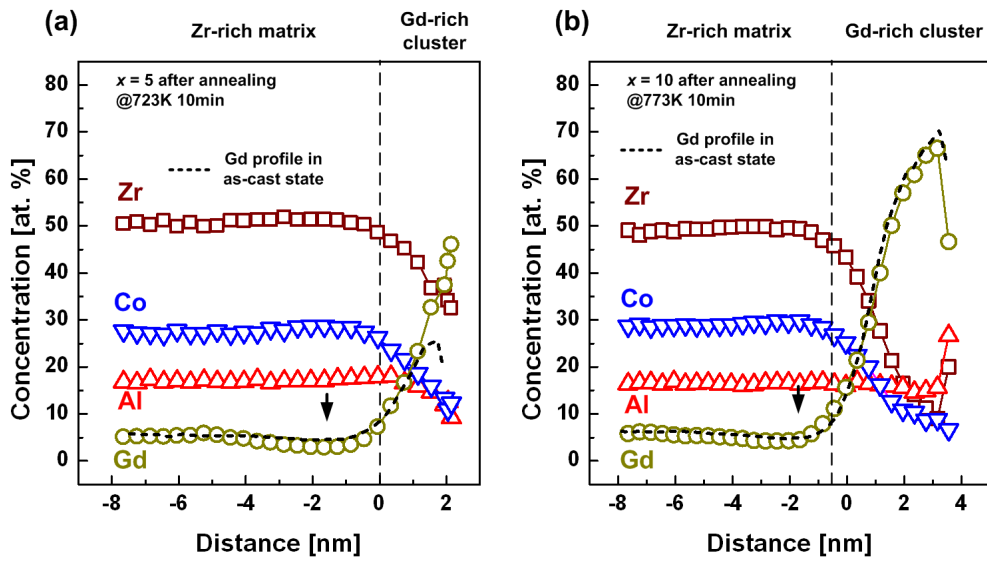


Figure 5.9: Proximity histograms for annealed (a) $Zr_{51}Gd_5Co_{28}Al_{16}$ and (b) $Zr_{46}Gd_{10}Co_{28}Al_{16}$ glasses. Corresponding concentration profiles of Gd in as-quenched state are also shown as a dashed line for comparison.

Table 5.1: Comparison of microstructural parameters calculated by proximity histograms. Inter-cluster distances are also estimated using values of cluster number densities.

$Zr_{51}Gd_5Co_{28}Al_{16}$	As-quenched					10 min @ 723 K				
	Size (nm)	Zr	Gd	Co	Al	Size (nm)	Zr	Gd	Co	Al
Gd-Cluster	3.8	38.2	25.6	21.1	15.1	3.9	32.5	46.0	12.3	9.2
Matrix		50.4	5.4	26.7	17.5		50.2	5.3	27.1	17.4
Cluster density	0.0017 nm ⁻³					0.0018 nm ⁻³				
Inter-cluster distance	8.4 ± 0.5 nm					8.2 ± 0.5 nm				
$Zr_{46}Gd_{10}Co_{28}Al_{16}$	As-quenched					10 min @ 723 K				
	Size (nm)	Zr	Gd	Co	Al	Size (nm)	Zr	Gd	Co	Al
Gd-cluster	6.9	3.7	70.3	7.1	18.9	7.1	9.0	66.5	8.8	15.7
Matrix		48.5	6.2	28.5	16.8		49.1	5.8	28.8	16.3
Cluster density	0.0002 nm ⁻³					0.0003 nm ⁻³				
Inter-cluster distance	17 ± 1 nm					15 ± 1 nm				

Based on the experimental results in this section, a schematic drawing of the pseudo-binary section of the quaternary Zr-Gd-Co-Al phase diagram with miscibility gap (colored region) is presented in Fig. 5.10. The results suggest that the critical temperature of liquid-liquid phase separation T_c , i.e. the boundary of the miscibility gap, strongly depends on the composition of the alloys. The homogeneous glassy structure for $x_{Gd} = 2$

and its thermal behavior, which is analogous to $x = 0$, implies that the T_c is far below the glass transition temperature T_g and the composition of the glass is out of the miscibility gap. The earliest stage of spinodal decomposition is characterized for $x_{\text{Gd}} = 5$ by the experimental results above. For $x_{\text{Gd}} = 5$, the T_c slightly above T_g is concluded. Analogously, further developed stages of decomposition obtained from $x \geq 10$ concluded larger temperature intervals between T_c and T_g (i.e. T_c is much higher than T_g).

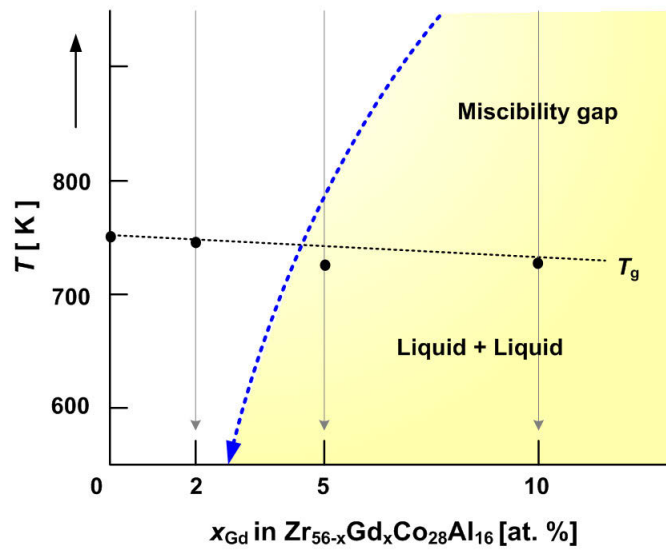


Figure 5.10: Schematic drawing of the binary section of the $\text{Zr}_{56-x}\text{Gd}_x\text{Co}_{28}\text{Al}_{16}$ phase diagram.

Chapter 6: Summary and outlook

Summary

The main objective of this thesis was to investigate the liquid-liquid phase separation phenomena in Gd-based (and Gd-containing) alloys. In particular the aim of the phase separation study encompassed understanding of phase equilibria in binary (Gd-Zr and Gd-Ti) and ternary (Gd-Ti-Co) alloy systems with a miscibility gap on one hand, and the synthesis of new phase separated metallic glasses in Gd-containing multi component systems and characterization of their structure formation on the other hand. The following main points can be derived from the present investigations:

1. For the Gd-Zr system a finite range of coexistence of *bcc*-Gd and *bcc*-Zr was derived which has been unknown so far from previous assessments. A flattening of the liquidus, which indicates the existence of a metastable miscibility gap was also observed. In addition, for the Gd-Ti system an extended range of coexistence of *bcc*-Ti and Gd-rich liquid phase and a monotectic reaction at $T = 1840$ K was detected which has been unknown from previous assessments. For both the alloy systems the experimental observations and corresponding data led to improved Gd-Zr and Gd-Ti phase diagrams. Based on the experimental results, new thermodynamic descriptions could be developed.
2. For the ternary Gd-Ti-Co system, the first experimental and thermodynamic assessment particularly focusing on the liquid-liquid miscibility gap has been carried out in this work. For the $\text{Gd}_{35}\text{Ti}_{35}\text{Co}_{30}$ alloy, the coexistence of two liquid phases in the high temperature range $1690 \text{ K} < T < 1760 \text{ K}$ was experimentally proven by *in situ* X-ray diffraction. Investigation of the microstructures and chemical compositions clearly showed evidence for the occurrence of a liquid-liquid phase separation in wide composition range. Both the experimental results and the thermodynamic approximation by *CALPHAD* calculation suggest that the stable miscibility gap of the binary Gd-Ti system extends into the ternary Gd-Ti-Co system for up to about 35 at.% Co.

3. Rapidly quenched Gd-Hf(or Ti)-Co-Al alloy system undergoes liquid-liquid phase separation in wide composition range. These quaternary alloys decompose into two Gd-rich and Hf-rich (or Ti-rich) liquid phases with different morphologies. Depending on the GFA of each separated liquid phase, either glass-glass or glass-crystalline composites can be obtained. The results reaffirm that the prerequisites: a strong positive enthalpy of mixing between the constituent elements and a good GFA for each decomposed liquid phase must be fulfilled for synthesis of a new glass-glass composite. Different types of microstructures, such as an interconnected structure or a droplet structure can be tailored by composition and quenching conditions.

4. Phase separated metallic glasses can also be prepared in the Zr-Gd-Co-Al system by rapid quenching of the melt. The structure formation as a function of the Gd content is essentially determined by the composition dependence of the miscibility gap of the meta stable undercooled melt. Early stages of spinodal decomposition were obtained because the critical temperature T_c of liquid-liquid phase separation is close to the glass transition temperature T_g , i.e. T_c is just above the T_g . Direct evidence of the phase separation was proven by APT, which revealed Gd-enriched clusters of about 4-7 nm in size for the $Zr_{51}Gd_5Co_{28}Al_{16}$ and $Zr_{46}Gd_{10}Co_{28}Al_{16}$ glasses. Simultaneous measurements of *in situ* SAXS and WAXS at elevated temperature or in an isothermal condition proved further structural development by spinodal decomposition prior to crystallization as a function of temperature and time. An almost homogeneous glassy state is obtained on the other hand if T_c is below the T_g .

5. The magnetic properties of the phase separated Gd-Hf(or Ti)-Co-Al alloys have been analyzed. The values of ordered magnetic moment determined from the saturation magnetization are in accordance with the calculated values obtained under the assumption that only the Gd atoms contribute to the saturation magnetization. This agreement led to a conclusion that the occurrence of liquid-liquid phase separation does not play an important role concerning the saturation magnetization. However, the magnetic ordering in the investigated temperature range is ascribed exclusively to the phase with high Gd content, i.e. Gd-rich glassy phase. Therefore phase separation phenomena still have to be taken into account in order to explain the evolution of the Curie temperature T_{Curie} .

Outlook

In terms of outlook, especially from the perspective of engineering aspects, the phase separation phenomena should be emphasized and be further studied as an effective strategy to controllably tune the microstructure of metallic glasses and alloys. Developing phase-separated metallic glasses with hierarchical microstructure is of potential interest in terms of the following aspects:

1. As demonstrated in this thesis, nanometer-scaled chemical or structural heterogeneities in the glassy matrix are characterized if an alloy composition is at the edge of the miscibility gap or the miscibility gap is metastable. Such a microstructural heterogeneity in nanometer length scale can enhance the plasticity and may even result in superplasticity of metallic glass. Therefore, attempts should be made to develop spatially heterogeneous metallic glasses based on phase separation to investigate the origin of either the enhanced plasticity or brittleness.
2. In general, two glassy phases of the phase-separated metallic glass are different in chemical composition and corresponding chemical reactivity. Therefore, the selective electrochemical dissolution can lead to synthesis of unique structures such as nano-porous metallic glasses and nano-powder. Especially the nano-porous metallic glass is promising as novel functional materials such as hydrogen storage media for fuel cells or membranes for filtration. However, there are only few such studies reported so far.
3. Although the magnetic properties of phase-separated metallic glasses in this work were characterized only in general view. It has been proved that magnetic glassy particles can be homogeneously distributed in glassy (or crystalline) matrix. One can also consider synthesis of hybrid type of magnetic materials by phase separation phenomena.

In addition, the assessment of phase diagrams can be substantially benefited by using *in situ* X-ray diffraction and containerless sample processing especially for alloy systems with high liquidus temperature, and/or reactive melts, as concluded through this thesis. Therefore, attempts should be made to experimentally reassess the phase diagrams of binary immiscible systems from a fundamental point of view.

Chapter 7: Appendix

The thermodynamic assessments of the binary Gd-Zr and Gd-Ti system presented in Chapter 4 were done by Dr. Mattern in IFW-Dresden and Dr. O. Fabrichnaya in Institut für Werkstoffwissenschaft at TU-Freiberg using the *CALPHAD* method [136]. The Gibbs free energy of each element is defined with respect to its stable magnetically disordered state at $T = 298.15$ K and $P = 10^5$ Pa (stable element reference). In the SGTE-Pure database 4.4 [137], the Gibbs free energy is represented as a power series in terms of the temperature in the form:

$${}^0G(T) = A + B \cdot T + C \cdot T \cdot \ln(T) + D \cdot T^2 + E \cdot T^3 + \frac{F}{T} + \sum_n G_n \cdot T^n, \quad (8.1)$$

where A to F and G_n are coefficients and n represents a set of integers. The reference states for pure gadolinium, zirconium and titanium are *hcp*-Gd, *hcp*-Zr and *hcp*-Ti, respectively.

The liquid and the disordered solid solutions, *bcc* and *hcp* are described using a substitutional solution model with the Gibbs free energy being defined as:

$$G^\varphi = \sum_{i=1}^2 x_i G_i^{\text{ref}} + G^{\text{id}} + G^{\text{excess}}; \quad G^{\text{id}} = RT \sum_{i=1}^2 x_i \ln(x_i);$$

$$G^{\text{excess}} = \sum_{i=1}^2 \sum_{j>i}^2 x_i x_j \sum_{v=0}^n {}^v L_{i,j} (x_i - x_j)^v, \quad (8.2)$$

where G_i^{ref} is the reference Gibbs free energy of the pure element i , i.e., Gd or Zr or Ti in the corresponding phase φ , G^{id} is the ideal mixing contribution, G^{excess} is the excess energy, x_i and x_j are the mole fractions of the constituents i , and j , respectively. ${}^v L_{i,j}$ is the binary interaction parameter of components i and j of an order v . R is the gas constant, and T is the absolute temperature. Magnetic contributions to the Gibbs free energy of *hcp*-Gd phase were taken into account according to the treatment proposed by Hillert and Jarl [138]. For a phase with the magnetic moment β (Bohr's magneton per mole of atoms) and the

magnetic ordering (Curie or Neel) temperature T_{Curie} , the magnetic contribution to its Gibbs free energy is expressed as [139]:

$$G^{\text{mag}} = RT \ln(\beta + 1) f(T / T_{\text{Curie}}), \quad (8.3)$$

where $f(T/T_{\text{Curie}})$ represents a polynomial function. For *bcc*-Zr, *bcc*-Ti, *bcc*-Gd, *hcp*-Ti and *hcp*-Zr, the magnetic moment β was fixed as value equal to zero. The thermodynamic model parameters for the binary systems Gd-Zr and Gd-Ti were assessed using the least-squares optimization module *PARROT* of *Thermo-Calc* software [140].

The final thermodynamic parameters for Gd-Zr and Gd-Ti systems used in this work are given in Table 7.1 and Table 7.2, respectively. The phase diagram calculations were performed using the *PANDAT* software [141]. The computed Gd-Zr and Gd-Ti phase diagrams using the set of thermodynamic parameters above is shown in Fig. 4.6 and Fig. 4.15 along with the present experimental results. The calculated temperatures and phase compositions for invariant equilibria are also given in Table 4.1 and Table 4.4.

Table 7.1: Summary of thermodynamic parameters describing the *Gd-Zr* system ($298.15 < T < 2150$ K) referred to the stable element reference H^{SER} ($T = 298.15$ K, $P = 100$ kPa). Values are given in SI units (J, mol, and K), except β (μ_{B} per mole of atoms).

Parameter	Ref.
$G_{\text{Gd}}^{\text{hcp}}, G_{\text{Gd}}^{\text{bcc}}, G_{\text{Gd}}^{\text{liquid}}, G_{\text{Zr}}^{\text{hcp}}, G_{\text{Zr}}^{\text{bcc}}, G_{\text{Zr}}^{\text{hcp}}$	[137]
Liquid	
${}^0L_{\text{Gd,Zr}}^{\text{liq}} = -6605 + 18.951 \cdot T$	[142]
${}^1L_{\text{Gd,Zr}}^{\text{liq}} = +22971 - 11.905 \cdot T$	[142]
Hcp	
${}^0L_{\text{Gd,Zr}}^{\text{hcp}} = +14717 + 18.309 \cdot T$	[142]
${}^1L_{\text{Gd,Zr}}^{\text{hcp}} = -378$	[142]
Bcc	
${}^0L_{\text{Gd,Zr}}^{\text{bcc}} = +52843 - 9.383 \cdot T$	[142]
${}^1L_{\text{Gd,Zr}}^{\text{bcc}} = +22983 - 16.792 \cdot T$	[142]
Magnetic parameter $T_{\text{curie}}^{\text{Gd}} = 293.4$, $\beta_{\text{Gd}} = 3$	[137]

Table 7.2: Summary of thermodynamic parameters describing the *Gd-Ti* system.

Parameter	Ref.
$G_{Gd}^{hcp}, G_{Gd}^{bcc}, G_{Gd}^{liquid}, G_{Ti}^{hcp}, G_{Ti}^{bcc}, G_{Ti}^{hcp}, G_{Ti}^{liquid}$	[137]
Liquid	
${}^0L_{Gd,Ti}^{liq} = 93481 - 30.90272 \cdot T$	[143]
${}^1L_{Gd,Ti}^{liq} = -8955$	[143]
hcp	
${}^0L_{Gd,Ti}^{hcp} = +44248.7 + 19.9839 \cdot T$	[143]
${}^1L_{Gd,Ti}^{hcp} = 2176.21$	[143]
bcc	
${}^0L_{Gd,Ti}^{bcc} = +39476.4 + 15.687 \cdot T$	[143]
${}^1L_{Gd,Ti}^{bcc} = +2152.38$	[143]
Magnetic parameter $T_{curie}^{Gd} = 293.4$, $\beta_{Gd} = 3$	[137]

Acknowledgement

Herewith I acknowledge my gratitude to all of them who helped me a lot during my Ph.D. work. With the support of many people, this work could be successfully accomplished.

First and foremost I would like to express my deep sense of gratitude to Prof. Jürgen Eckert for providing the opportunity to do PhD in Leibniz Institute for Solid State and Materials Research (IFW-Dresden), in association with Faculty of Mechanical Science and Engineering at the Technical University of Dresden. I equally express my sincere gratitude to my research supervisor Dr. Norbert Mattern who gave me amazing support and supervision and for offering me to work for my PhD in his Structural Research department with the financial support by the Deutsche Forschungsgemeinschaft (DFG). I would like to express my special thanks to his immense patience and forbearance on me. As the list of the people appears to be endless, I express my sincere thanks to each and everyone, who helped me either directly or indirectly with the realization of this PhD thesis:

Thanks to all the former and current members of the structural research department (Abt.32) at the IFW-Dresden, especially to Dr. A. Teresiak, B. Opitz, Dr. B. Schwarz, Dr. M. Stoica, Dr. I. Kaban, Dr. G. Wang and Dr. O. Shuleshova for their valuable support and discussions. I would not forget to thank to Dr. U. Kühn, Dr. H. Wendrock, Dr. T. Gemming and Dr. J. Thomas for letting me work with freedom in the IFW-Dresden. I also equally give my thanks to S. Donath, M. Frey, B. Bartusch, D. Lohse, A. Voß and J. Werner for their technical support and advices.

Thanks to my office colleagues Arne and Matthias for the homely atmosphere and equilibrium state of our office. (Also for the co-management of IFW-AQUARIUM)

I wish to express my sincere thanks to all my friends in Dresden, at first to the fellow 2 Musketeers of the 3, Dr. Saisharan Aswartham and Dr. Sandeep Gorantla, thanks a lot for your support guys. Special thanks to Christoph and Dominik for huge amount of right and wrong information about the life in Germany. My sincere thanks for the support,

encouragement, help and for the unforgettable time for the past 4 years to Simon, Konrad, Yue, Gang, Piter, Miroslava, Julia, Valentin, Kaikai, Kumar Babu, Hooyar, Raghu, Prashanth, Mohsen, Benjamin...

I also want to thank to people from outside of the IFW-Dresden for their great support and advices:

- Dr. U. Vainio and Dr. J. Bednarčik for their support and advices during the synchrotron experiments in DESY, Hamburg.
- Dr. D. Holland-Moritz and his team in DLR for a great collaboration.
- Special thanks to Prof. Do-Hyang Kim, for his constant support and for being as the second referee of this thesis.

I must thank my best school friends, Minchul and Byounghoon for being alive.

Last but not least, I would like to give my special thanks to my father and sister as well as my family-in-law for their constant encouragement. I would like to thank Eunmi, my great love. This thesis is dedicated to her with my perpetual love, “You are the one who completes me”.

Junhee Han

Dresden Nov. 2013

Bibliography

- [1] K. Binder, Theory of first-order phase transitions, *Reports on Progress in Physics* **50**, 783 (1987).
- [2] E. M. Levin, and S. Block, Structural interpretation of immiscibility in oxide systems: I, Analysis and calculation of immiscibility, *Journal of the American Ceramic Society* **40**, 95 (1957).
- [3] S. Block and E. M. Levin. Structural interpretation of immiscibility in oxide systems: II, Coordination principles applied to immiscibility, *Journal of the American Ceramic Society* **40**, 113 (1957).
- [4] K. Nakanishi and N. Soga, Phase separation in gelling silica-organic polymer solution: Systems containing poly (sodium styrenesulfonate), *Journal of the American Ceramic Society* **74**, 2518 (1991).
- [5] T. Nishi, T. T. Wang and T. K. Kwei, Thermally induced phase separation behavior of compatible polymer mixtures, *Macromolecules* **8**, 227 (1974).
- [6] A. A. Kündig, M. Ohnuma, D. H. Ping, T. Ohkubo and K. Hono, In situ formed two-phase metallic glass with surface fractal microstructure, *Acta Materialia* **52**, 2441 (2004).
- [7] B. J. Park, H. J. Chang, W. T. Kim and D. H. Kim, In situ formation of two amorphous phases by liquid phase separation in Y-Ti-Al-Co alloy, *Applied Physics Letters* **85**, 6353 (2004).
- [8] N. Mattern, U. Kühn, A. Gebert, T. Gemming, M. Zinkevich, H. Wendrock and L. Schultz, Microstructure and thermal behavior of two-phase amorphous Ni-Nb-Y alloy, *Scripta Materialia* **53**, 271 (2005).
- [9] F. R. de Boer, R. Boom, W. C. M. Mattens, A. R. Miedema and A. K. Niessen, *Cohesion in Metals: Cohesion and Structure*, (North-Holland, Amsterdam, 1988).

-
- [10] A. Takeuchi and A. Inoue, Classification of bulk metallic glasses by atomic Size difference, heat of mixing and period of constituent elements and its application to characterization of the main alloying element, *Materials Transactions* **46**, 2817 (2005).
- [11] J. C. Oh, T. Ohkubo, Y. C. Kim, E. Fleury and K. Hono, Phase separation in Cu₄₃Zr₄₃Al₇Ag₇ bulk metallic glass, *Scripta Materialia* **53**, 165 (2005).
- [12] E. S. Park and D. H. Kim, Phase separation and enhancement of plasticity in Cu-Zr-Al-Y bulk metallic glasses, *Acta Materialia* **54**, 2597 (2006).
- [13] E. S. Park, E. Y. Jeong, J. K. Lee, J. C. Bae, A. R. Kwon, A. Gebert, L. Schultz, H. J. Chang and D. H. Kim, In situ formation of two glassy phases in the Nd-Zr-Al-Co alloy system, *Scripta Materialia* **56**, 197 (2007).
- [14] E. S. Park, J. S. Kyeong and D. H. Kim, Phase separation and improved plasticity by modulated heterogeneity in Cu-(Zr, Hf)-(Gd, Y)-Al metallic glasses, *Scripta Materialia* **57**, 49 (2007).
- [15] N. Mattern, T. Gemming, G. Goerigk and J. Eckert, Phase separation in amorphous Ni-Nb-Y alloys, *Scripta Materialia* **57**, 29 (2007).
- [16] N. Mattern, U. Kühn, A. Gebert, A. Schöps, T. Gemming and L. Schultz, Phase separation in liquid and amorphous Ni-Nb-Y alloys, *Materials Science and Engineering A* **449**, 207 (2007).
- [17] H. J. Chang, E. S. Park, W. Yook and D. H. Kim, Network structure composite in phase separating Gd₃₀Zr₂₅Al₂₅(Co/Cu)₂₀ metallic glassy alloys, *Intermetallics* **18**, 1846 (2010).
- [18] H. J. Chang, W. Yook, E. S. Park, J. S. Kyeong and D. H. Kim, Synthesis of metallic glass composites using phase separation phenomena, *Acta Materialia* **58**, 2483 (2010).
- [19] N. Mattern, U. Vainio, B. Schwarz, J.M. Park, D.H. Kim and J. Eckert, Phase separation in Ni₇₀Nb_{30-x}Y_x glasses, *Intermetallics* **18**, 1842 (2010).

-
- [20] D. Chen, A. Takeuchi and A. Inoue, Gd-Co-Al and Gd-Ni-Al bulk metallic glasses with high glass forming ability and good mechanical properties, *Materials Science and Engineering: A* **457**, 226 (2007).
- [21] T. Wada, F. Qin, X. Wang, M. Yoshimura, N. Sugiyama, R. Ito, N. Matsushita and A. Inoue, Formation and bioactivation of Zr-Al-Co bulk metallic glasses, *Journal of Materials Research* **24**, 2941 (2009).
- [22] T. Wada, T. Zhang, A. Inoue, Formation, thermal stability and mechanical properties in Zr-Al-Co bulk glassy alloys, *Materials Transactions* **43**, 2843 (2002).
- [23] T. B. Massalski, *Binary Alloy Phase Diagrams* (ASM International, Materials Park, 1990).
- [24] D. A. Porter and K. E. Easterling, *Phase Transformation in Metals and Alloys* (2nd ed. Chapman & Hall, London, 1992).
- [25] D. R. Gaskell, *Introduction to the Thermodynamics of Materials* (Taylor & Francis, London, 2003).
- [26] Britannica, Encyclopedia, Encyclopedia Britannica Online (<http://www.britannica.com>, 2012).
- [27] S. R. Elliott, *Physics of Amorphous Materials* (Longman, New York, 1990).
- [28] R. Zallen, *The Physics of Amorphous Solids* (Wiley-VCH, Weinheim, 1998).
- [29] E. Le Bourhis, *Glass: Mechanics and Technology* (Wiley-VCH Weinheim, 2007).
- [30] P. G. Debenedetti and F. H. Stillinger, Supercooled liquids and the glass transition, *Nature* **410**, 259 (2001).
- [31] M. D. Ediger, C. A. Angell and S. R. Nagel, Supercooled liquids and glasses, *The Journal of Physical Chemistry* **100**, 13200 (1996).
- [32] M. H. Cohen and D. Turnbull, Composition requirements for glass formation in metallic and ionic systems, *Nature* **189**, 131 (1961).
- [33] A. Inoue and C. Suryanarayana, *Bulk Metallic Glasses* (Taylor & Francis, London, 2011).

-
- [34] P. Duwez, Non-crystalline structure in solidified gold-silicon alloys, *Nature* **187**, 869 (1960).
- [35] H. W. Kui, A. L. Greer and D. Turnbull, Formation of bulk metallic glass by fluxing, *Applied Physics Letters* **45**, 615 (1984).
- [36] A. Inoue, T. Nakamura, N. Nishiyama and T. Masumoto, Mg-Cu-Y Bulk amorphous alloys with high tensile strength produced by a high-pressure die casting method, *Materials Transactions* **33**, 937 (1992).
- [37] A. Inoue and J. S. Gook, Fe-based ferromagnetic glassy alloys with wide supercooled liquid region, *Materials Transactions* **36**, 1180 (1995).
- [38] A. Inoue, T. Zhang, H. Koshiha, A. Makino, New bulk amorphous Fe-(Co,Ni)-M-B (M = Zr, Hf, Nb, Ta, Mo, W) alloys with good soft magnetic properties, *Journal of Applied Physics* **83**, 6326 (1998).
- [39] A. Inoue, Synthesis and properties of Ti-based bulk amorphous alloys with a large supercooled liquid region, *Materials Science Forum* **312-314**, 307 (1999).
- [40] B. L. Shen, H. Koshiha, T. Mizushima and A. Inoue, Bulk amorphous Fe-Ga-P-B-C alloys with a large supercooled liquid region, *Materials Transactions* **41**, 873 (2000).
- [41] T. Zhang, K. Kurosaka and A. Inoue, Thermal and mechanical properties of Cu-based Cu-Zr-Ti-Y bulk glassy alloys, *Materials Transactions* **42**, 2042 (2001).
- [42] A. Inoue, T. Zhang, K. Kurosaka and W. Zhang, High-strength Cu-based bulk glassy alloys in Cu-Zr-Ti-Be system, *Materials Transactions* **42**, 1800 (2001).
- [43] D. Xu, B. Lohwongwatana, G. Duan, W. L. Johnson and C. Garland, Bulk metallic glass formation in binary Cu-rich alloy series $\text{Cu}_{100-x}\text{Zr}_x$ ($x = 34, 36, 38.2, 40$ at.%) and mechanical properties of bulk $\text{Cu}_{64}\text{Zr}_{36}$ glass, *Acta Materialia* **52**, 2621 (2004).
- [44] V. Ponnambalam, S. J. Poon, G. J. Joseph, Fe-based bulk metallic glasses with diameter thickness larger than one centimeter, *Journal of Materials Research* **19**, 1320 (2004).

-
- [45] J. C. Dyre, Source of non-Arrhenius average relaxation time in glass-forming liquids, *Journal of Non-Crystalline Solids* **235-237**, 142 (1998).
- [46] G. H. Fredrickson, Recent developments in dynamical theories of the liquid-glass transition, *Annual Review of Physical Chemistry* **39**, 149 (1988).
- [47] T. R. Anantharaman, *Metallic Glasses: Production, Properties and Applications* (Trans Tech Publications, Aedermannsdorf, 1984).
- [48] T. R. Anantharaman and C. Suryanarayana, *Rapidly Solidified Metals - Technological Overview* (Trans Tech Publications, Aedermannsdorf, 1987).
- [49] D. M. Herlach, Non-equilibrium solidification of undercooled metallic melts, *Materials Science and Engineering: R: Reports* **12**, 177 (1994).
- [50] D. M. Herlach and B. Feuerbacher, Non-equilibrium solidification of undercooled metallic melts, *Advances in Space Research* **11**, 255 (1991).
- [51] D. Turnbull, M. Cohen and H. Morrel, Free-volume model of the amorphous phase: glass transition, *The Journal of Chemical Physics* **34**, 120 (1961).
- [52] D. Turnbull, Under what conditions can a glass be formed?, *Contemporary Physics* **10**, 473 (1969).
- [53] S. Mader, A. S. Nowick and H. Widmer, Metastable evaporated thin films of Cu-Ag and Co-Au alloys — I. occurrence and morphology of phases, *Acta Metallurgica* **15**, 203 (1967).
- [54] A. W. Simpson and P. H. Hodgkinson, Bubble raft model for an amorphous alloy, *Nature* **237**, 320 (1972).
- [55] A. Inoue, T. Zhang and T. Masumoto, Glass-forming ability of alloys, *Journal of Non-Crystalline Solids* **156-158**, Part 2, 473 (1993).
- [56] A. Inoue, High strength bulk amorphous alloys with low critical cooling rates, *Materials Transactions* **36**, 866 (1995).

- [57] T. Wada, D. V. Louzguine and A. Inoue, Preparation of Zr-based metallic glass nanowires and nanoparticles by selective etching, *Scripta Materialia* **57**, 901 (2007).
- [58] B. J. Park, Phase separation in metallic glasses, *PhD thesis*, Yonsei University Seoul, (2008).
- [59] J. He, H. Li, Haiquan, B. Yang, J. Zhao, H. Zhang and Z. Hu, *Journal of Alloys and compounds* **489**, 535 (2010).
- [60] B. D. Cullity, *Elements of X-ray diffraction* (2nd Ed.), (Addison-Wesley, Massachusetts, 1978).
- [61] S. Klein, D. Holland-Moritz and D. M. Herlach, Crystal nucleation in undercooled liquid zirconium, *Physical Review B* **80**, 212202 (2009).
- [62] O. Shuleshova, D. Holland-Moritz, W. Löser, V. Wolfgang, H. Andrea, H. Helena, U. Hecht, V. T. Witusiewicz, D. M. Herlach and B. Büchner, In situ observations of solidification processes in γ -TiAl alloys by synchrotron radiation, *Acta Materialia* **58**, 2408 (2010).
- [63] S. Klein, Nucleation in undercooled melts of pure zirconium and zirconium based alloys, *PhD thesis*, Ruhr University Bochum, (2010).
- [64] A. P. Hammersley, S. O. Svensson, M. Hanfland, A. N. Fitch and D. Hausermann, Two-dimensional detector software: From real detector to idealised image or two-theta scan, *High Pressure Research* **14**, 235 (1996).
- [65] Field Ion Microscopy (FIM) Group, (University of Oxford, <http://www.ox.ac.uk>, 2013).
- [66] N. Mattern, A. Shariq, B. Schwarz, U. Vainio and J. Eckert, Structural and magnetic nanoclusters in $\text{Cu}_{50}\text{Zr}_{50-x}\text{Gd}_x$ ($x = 5$ at.%) metallic glasses, *Acta Materialia* **60**, 1946 (2012).
- [67] R. H. Richman and W. P. McNaughton, Permanent-magnet materials: Research directions and opportunities, *Journal of Electronic Materials* **26**, 415 (1997).

- [68] N. Mattern, M. Zinkevich, A. Handstein, W. Gruner, S. Roth and O. Gutfleisch, Influence of Zr addition on phase formation and magnetic properties of the Fe₁₇Gd₂ phase, *Journal of Alloys and Compounds* **358**, 1 (2003).
- [69] M. Zinkevich, N. Mattern, I. Bächer and S. Puerta, Formation, crystal structure and magnetic properties of (1:12) compounds in the Fe-Gd-Mo-Zr system, *Journal of Alloys and Compounds* **336**, 320 (2002).
- [70] K. Prabahar, D. M. Raj Kumar, M. Manivel Raja and V. Chandrasekaran, Phase analysis and magnetocaloric properties of Zr substituted Gd-Si-Ge alloys, *Journal of Magnetism and Magnetic Materials* **323**, 1755 (2011).
- [71] H. M. Fu, D. Qiu, M. X. Zhang, H. Wang, P. M. Kelly and J. A. Taylor, The development of a new grain refiner for magnesium alloys using the edge-to-edge model, *Journal of Alloys and Compounds* **456**, 390 (2008).
- [72] M. I. Copeland, C. E. Armantrout and H. Kato, *U.S. Bureau of Mines Report of Investigation* **5850** (1961).
- [73] M. I. Copeland and H. Kato, Physics and Material Problems of Reactor Control Rods, *International Atomic Energy Agency*, Vienna, 295 (1964).
- [74] M. Zinkevich, N. Mattern and H. J. Seifert, Thermodynamic assessment of Gd-Zr and Gd-Mo systems, *Journal of Phase Equilibria and Diffusion* **22**, 43 (2001).
- [75] S. Schmitz, H-G. Lindenkreuz, N. Mattern, W. Löser and B. Büchner, Liquid phase separation in Gd-Ti and Gd-Zr melts, *Intermetallics* **18**, 1941 (2010).
- [76] K. F. Kelton, A. K. Gangopadhyay, G. W. Lee, L. Hannet, R. W. Hyers, S. Krishnan, M. B. Robinson, J. Rogers and T. J. Rathz, X-ray and electrostatic levitation undercooling studies in Ti-Zr-Ni quasicrystal forming alloys, *Journal of Non-Crystalline Solids* **312-314**, 305 (2002).
- [77] O. Shuleshova, D. Holland-Moritz, A. Voss and W. Löser, In situ observations of solidification in Ti-Al-Ta alloys by synchrotron radiation, *Intermetallics* **19**, 688 (2011).
- [78] P. Ehrenfest, *Proceedings of the Koninklijke Nederlandse Akademie van Wetenschappen Amsterdam* **17**, 1184 (1915).

- [79] K. H. J. Buschow, Short-range order and thermal stability in amorphous alloys, *Journal of Physics F: Metal Physics* **14**, 593 (1984).
- [80] N. Mattern, A. Schöps, U. Kühn, J. Acker, O. Khvostikova and J. Eckert, Structural behavior of $\text{Cu}_x\text{Zr}_{100-x}$ metallic glass ($x = 35-70$), *Journal of Non-Crystalline Solids* **354**, 1054 (2008).
- [81] T. Schenk, D. Holland-Moritz, V. Simonet, R. Bellissent and D. M. Herlach, Icosahedral short-range order in deeply undercooled metallic melts, *Physical Review Letters* **89**, 75507 (2002).
- [82] V. N. German, A. A. Bakanova, L. A. Tarasova and Y. N. Sumilov, *Sov. Physics Solid State* **12**, 490 (1971).
- [83] R. B. Russell, Coefficients of thermal expansion for zirconium, *Transactions of the Metallurgical Society of AIME* **200**, 1045 (1954).
- [84] T. Kordel, D. Holland-Moritz, F. Yang, J. Peters, T. Unruh, T. Hansen and A. Meyer, Neutron scattering experiments on liquid droplets using electrostatic levitation, *Physical Review B* **83**, 104205 (2011).
- [85] K. Yamada, Y. Okubo, S. Kamado and Y. Kojima, Precipitate Microstructures of High Strength Mg-Gd-Y-Zn-Zr Alloys, *Advanced Materials Research* **11-12**, 417 (2006).
- [86] F. H. Spedding, J. J. Hanak and A. H. Daane, High temperature allotropy and thermal expansion of the rare-earth metals, *Journal of the Less Common Metals* **3**, 110 (1961).
- [87] A. E. Miller and A. H. Daane, *Transactions of the Metallurgical Society of AIME* **230**, 568 (1964).
- [88] J. G. Croeni and S. C. Rhoads, Titanium-Gadolinium phase diagram (Gd-Ti), *United States Bureau of Mines Invest.* **5796**, 1 (1961).
- [89] E. M. Savitskii and G. C. Burchanov, *Russian Journal of Inorganic Chemistry* **7**, 358 (1962).

- [90] J. L. Murray, The Gd-Ti (Gadolinium-Titanium) system, *Phase Diagrams of Binary Titanium Alloys* (ASM International, Metals Park, 1987).
- [91] H. Okamoto, Gd-Ti (Gadolinium-Titanium), *Journal of Phase Equilibria and Diffusion* **33**, 422 (2012).
- [92] N. Sobczak, R. Nowak, W. Radziwill, J. Budzioch and A. Glenz, Experimental complex for investigations of high temperature capillarity phenomena, *Materials Science and Engineering: A* **495**, 43 (2008).
- [93] Y. Q. Cheng, E. Ma, Atomic-level structure and structure-property relationship in metallic glasses, *Progress in Materials Science* **56**, 379 (2011).
- [94] D. Holland-Moritz, O. Heinen, R. Bellissent and T. Schenk, Short-range order of stable and undercooled liquid titanium, *Materials Science and Engineering: A* **449-451**, 42 (2007).
- [95] J. Spreadborough and J. W. Christian, The measurement of the lattice expansions and Debye temperatures of titanium and silver by X-ray methods, *Proceedings of the Physical Society* **74**, 609 (1959).
- [96] V. K. Sinha, S. F. Cheng, W. E. Wallace and S. G. Sankar, Magnetic behavior of heavy rare earth RTiFe_{11-x}Co_x alloys, *Journal of Magnetism and Magnetic Materials* **81**, 227 (1989).
- [97] D. V. Louzguine, T. Wada, H. Kato, J. Perepezko and A. Inoue, In situ phase separation and flow behavior in the glass transition region, *Intermetallics* **18**, 1235 (2010).
- [98] P. Duwez and J. L. Taylor, The structure of intermediate phases in alloys of titanium with iron, cobalt, and nickel, *Transactions of the Metallurgical Society of AIME* **188**, 1173 (1950).
- [99] H. Okamoto, Co-Gd (Cobalt-Gadolinium), *Journal of Phase Equilibria* **13**, 673 (1992).
- [100] G. R. Purdy and J. G. Parr, The Composition Range of Ti₂Co, *Transactions of the Metallurgical Society of AIME* **218**, 225 (1961).

-
- [101] I. Kaban and W. Hoyer, Characteristics of liquid-liquid immiscibility in Al-Bi-Cu, Al-Bi-Si, and Al-Bi-Sn monotectic alloys: Differential scanning calorimetry, interfacial tension, and density difference measurements, *Physical Review B* **77**, 125426 (2008).
- [102] H. E. Stanley, *Introduction to Phase Transitions and Critical Point Phenomena* (Oxford University Press, Oxford, 1987).
- [103] C. Domb, *The Critical Point: a Historical Introduction to the Modern Theory of Critical Phenomena* (Taylor and Francis, London, 1996).
- [104] O. A. W. Strydom and L. Alberts, The structure of Gd₃Co, *Journal of the Less Common Metals* **22**, 511 (1970).
- [105] G. Cacciamani, R. Ferro, I. Ansara and N. Dupin, Thermodynamic modelling of the Co-Ti system, *Intermetallics* **8**, 213 (2000).
- [106] Z. K. Liu, W. Zhang and B. Sundman, Thermodynamic assessment of the Co-Fe-Gd systems, *Journal of Alloys and Compounds* **226**, 33 (1995).
- [107] D. V. Louzguine, H. Kato, H. S. Kim and A. Inoue, Formation of 2-5 nm size pre-precipitates of cF96 phase in a Hf-Co-Al glassy alloy, *Journal of Alloy and Compound* **359**, 198 (2003).
- [108] B. Schwarz, B. Podmilsak, N. Mattern and J. Eckert, Magnetocaloric effect in Gd-based Gd₆₀Fe_xCo_{30-x}Al₁₀ metallic glasses, *Journal of Magnetism and Magnetic Materials* **322**, 2298 (2010).
- [109] J. C. Russ and R. T. Dehoff, *Practical Stereology* (Plenum Press, New York, 2000).
- [110] A. J. Wagner and J. M. Yeomans, Breakdown of scale invariance in the coarsening of phase-separating binary fluids, *Physical Review Letters* **80**, 1429 (1998).
- [111] Y. Xue and H. M. Wang, Microstructure and properties of Ti-Co-Si ternary intermetallic alloys, *Journal of Alloy and Compound* **464**, 138 (2008).
- [112] N. Mattern, G. Goerigk, U. Vainio, M.K. Miller, T. Gemming and J. Eckert, Spinodal decomposition of Ni-Nb-Y metallic glasses, *Acta Materialia* **57**, 903 (2009).

- [113] O. C. Hellman, J. A. Vandenbroucke, J. Rüsing, D. Isheim and D. N. Seidman, Identification of 2D boundaries from 3D atom probe data, and spatial correlation of atomic distributions with interfaces, *Material Research Society Symposium Proceedings* **578**, 395 (1999).
- [114] G. Kostorz, *Phase Transformation in Materials* (Wiley-VHC, Weinheim, 2001).
- [115] M. Foldeaki, R. Chahine, B. R. Gopal, T. K. Bose, X. Y. Liu and J. A. Barclay, Effect of sample preparation on the magnetic and magnetocaloric properties of amorphous Gd₇₀Ni₃₀, *Journal of Applied Physics* **83**, 2727 (1998).
- [116] J. Du, Q. Zheng, Y. B. Li, Q. Zhang, D. Li and Z. D. Zhang, Large magnetocaloric effect and enhanced magnetic refrigeration in ternary Gd-based bulk metallic glasses, *Journal of Applied Physics* **103**, 23918 (2007).
- [117] Q. Luo, D. Q. Zhao, M. X. Pan and W. H. Wang, Magnetocaloric effect in Gd-based bulk metallic glasses, *Applied Physics Letters* **89**, 81914 (2006).
- [118] P. Hansen, *Handbook of Magnetic Materials*, Vol. 6 (K. H. J. Buschow ed., North Holland, North Holland, 1991).
- [119] P. L. Dunn and S. J. Poon, Magnetic interactions in d band amorphous metallic alloys, *Journal of Physics F: Metal Physics* **12**, 273 (1982).
- [120] E. Burzo, Paramagnetic Behavior of Some Rare-Earth Cobalt Compounds, *Physical Review B* **6**, 2882 (1972).
- [121] C. L. Zhang, D. H. Wang, Z. D. Han, H. C. Xuan, B. X. Gu and Y. W. Du, Large magnetic entropy changes in Gd-Co amorphous ribbons, *Journal of Applied Physics* **105**, 13912 (2009).
- [122] K. Fukamichi, M. Kikuchi, T. Masumoto and M. Matsuura, Magnetic properties and invar effects of amorphous Gd-Co ribbons, *Physics Letters* **73A**, 436 (1979).
- [123] T. R. McGuire, T. Mizoguchi, R. J. Gambino and S. Kirkpatrick, Magnetic phase diagram of the Gd-Al and Gd-Cu amorphous systems, *Journal of Applied Physics* **49**, 1689 (1978).

-
- [124] J. W. Cahn, Phase separation by spinodal decomposition in isotropic systems, *Journal of Chemical Physics* **42**, 93 (1965).
- [125] J. S. Langer, Theory of spinodal decomposition in alloys, *Annals of Physics* **65**, 53 (1971).
- [126] J. S. Langer and A. J. Schwartz, Kinetics of nucleation in near-critical fluids, *Physical Review A* **21**, 948 (1980).
- [127] P. Haasen, The early stages of the decomposition of alloys, *Metallurgical Transactions A* **16**, 1173 (1985).
- [128] H. Nishimori and O. Akira, Pattern formation in phase-separating alloys with cubic symmetry, *Physical Review B* **42**, 980 (1990).
- [129] C. A. Angell, Formation of glasses from liquids and biopolymers, *Science* **267**, 1924 (1995).
- [130] P. van de Witte, P. J. Dijkstra, J. W. A. van den Berg and J. Feijen, Phase separation processes in polymer solutions in relation to membrane formation, *Journal of Membrane Science* **117**, 1 (1996).
- [131] P. van de Witte, P. J. Dijkstra, J. W. A. van den Berg and J. Feijen, Metastable liquid-liquid and solid-liquid phase boundaries in polymer-solvent-nonsolvent systems, *Journal of Polymer Science Part B: Polymer Physics* **35**, 763 (1996).
- [132] T. M. Rogers and R. C. Desai, Numerical study of late-stage coarsening for off-critical quenches in the Cahn-Hilliard equation of phase separation, *Physical Review B* **39**, 11956 (1989).
- [133] H. Tanaka, Viscoelastic phase separation, *Journal of Physics: Condensed Matter* **12**, R207 (2000).
- [134] J. W. Cahn, and J. E. Hilliard, Free energy of a nonuniform system. I. Interfacial free energy, *The Journal of Chemical Physics* **28**, 258 (1958).
- [135] T. Tsakalakos and M. P. Dugan, Nonlinear diffusion in spinodal decomposition: a numerical solution, *Journal of Materials Science* **20**, 1301 (1985).

-
- [136] L. Kaufman and H. Bernstein, Computer calculation of phase diagrams: with special reference to refractory metals, (Academic Press, New York, 1970).
- [137] *SGTE Unary Database* version 4.4, (<http://www.sgte.org>)
- [138] M. Hillert and M. Jarl, A model for alloying in ferromagnetic metals, *CALPHAD: Computer Coupling of Phase Diagrams and Thermochemistry* **2**, 227(1978).
- [139] J. O. Andersson, T. Helander, L. Höglund, P. Shi and B. Sundman, Thermo-Calc & DICTRA, computational tools for materials science, *CALPHAD: Computer Coupling of Phase Diagrams and Thermochemistry* **26**, 273 (2002).
- [140] *Thermocalc* Software (<http://www.thermocalc.com>)
- [141] *PANDAT*: A multi-component phase diagram calculation software (Computherm LLC, <http://www.computherm.com>).
- [142] N. Mattern, J. H. Han, M. Zinkevich, O. Shuleshova, I. Kaban, D. Holland-Moritz, J. Gegner, F. Yang, J. Bednarčik, W. Löser and J. Eckert, Experimental and thermodynamic assessment of the Gd–Zr system, *CALPHAD: Computer Coupling of Phase Diagrams and Thermochemistry* **39**, 27 (2012).
- [143] N. Mattern, J.H. Han, O. Fabrichnaya, M. Zinkevich, W. Löser, J. Werner, R. Nowak, I.Kaban, O. Shuleshova, D. Holland-Moritz, J. Bednarčik, N. Sobczak, J. Eckert, Experimental and thermodynamic assessment of the Gd-Ti system, *CALPHAD: Computer Coupling of Phase Diagrams and Thermochemistry* **42**, 19 (2013).

Publications

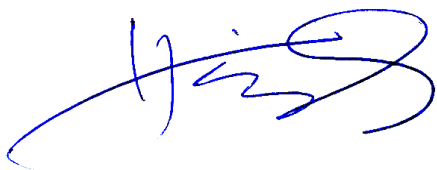
Within the framework of this dissertation the following publications have been published and are foreseen.

- [PUB 1] J. H. Han, N. Mattern, D. H. Kim and J. Eckert, Phase separation and microstructure evolution of rapidly quenched Gd-Hf-Co-Al alloys, *Journal of Alloys and Compound* **509**, S42 (2011).
- [PUB 2] N. Mattern, U. Vainio, J. M. Park, J. H. Han, A. Shariq, D. H. Kim and J. Eckert, Phase separation in $\text{Cu}_{46}\text{Zr}_{47-x}\text{Al}_7\text{Gd}_x$ metallic glasses, *Journal of Alloys and Compound* **509**, S23 (2011).
- [PUB 3] J. H. Han, N. Mattern, B. Schwarz, S. Gorantla, T. Gemming and J. Eckert, Microstructure and magnetic properties of Gd-Hf-Co-Al phase separated metallic glasses, *Intermetallics* **20**, 115 (2012).
- [PUB 4] J. H. Han, N. Mattern, B. Schwarz, D. H. Kim and J. Eckert, Phase separation and magnetic properties in Gd-(Hf,Ti,Y)-Co-Al metallic glasses, *Scripta Materialia* **67**, 149 (2012).
- [PUB 5] N. Mattern, J. H. Han, M. Zinkevich, O. Shuleshova, I. Kaban, D. Holland-Moritz, J. Gegner, F. Yang, J. Bednarčík, W. Löser and J. Eckert, Experimental and thermodynamic assessment of the Gd-Zr system, *CALPHAD: Computer Coupling of Phase Diagrams and Thermochemistry* **39**, 27 (2012).
- [PUB 6] J. M. Park, J. H. Han, N. Mattern, D. H. Kim and J. Eckert, Designing Zr-Cu-Co-Al bulk metallic glasses with phase separation mediated plasticity, *Metallurgical and Materials Transactions A* **43**, 2598 (2012)

-
- [PUB 7] I. Kaban, R. Nowak, O. Shuleshova, B. Korpala, G. Bruzda, A. Siewiorek, J. H. Han, N. Sobczak, N. Mattern and J. Eckert, Sessile drop study of Gd-Ti monotectic alloys on ceramic substrates: phase transformations, wetting, and reactivity, *Journal of Materials Science* **47**, 8381 (2012)
- [PUB 8] J. H. Han, N. Mattern, I. Kaban, D. Holland-Moritz, J. Bednarčik, R. Nowak, N. Sobczak, D. H. Kim and J. Eckert, Phase separation in ternary Co-Gd-Ti liquids, *Journal of Physics: Condensed Matter* **25**, 245104 (2013)
- [PUB 9] N. Mattern, J. H. Han, O. Fabrichnaya, M. Zinkevich, W. Löser, J. Werner, R. Nowak, I. Kaban, O. Shuleshova, D. Holland-Moritz, J. Bednarčik, N. Sobczak and J. Eckert, Experimental and thermodynamic assessment of the Gd-Ti system, *CALPHAD: Computer Coupling of Phase Diagrams and Thermochemistry* **42**, 19 (2013).
- [PUB 10] J. H. Han, N. Mattern, U. Vainio, A. Shariq, S. W. Sohn, D. H. Kim and J. Eckert, Phase separation in $Zr_{56-x}Gd_xCo_{28}Al_{16}$ metallic glasses ($0 \leq x \leq 20$), *Acta Materialia*, (Accepted, Nov. 2013)

Erklärung

Hiermit versichere ich, dass ich die vorliegende Arbeit ohne die unzulässige Hilfe Dritter und ohne Benutzung anderer als der angegebenen Hilfsmittel angefertigt habe; die aus fremden Quellen direkt oder indirekt übernommenen Gedanken sind als solche kenntlich gemacht. Bei der Auswahl und Auswertung des Materials sowie bei der Herstellung des Manuskripts habe ich Unterstützungsleistungen von folgenden Personen erhalten: Prof. Dr. J. Eckert und Dr. N. Mattern. Weitere Personen waren an der geistigen Herstellung der vorliegenden Arbeit nicht beteiligt. Insbesondere habe ich nicht die Hilfe eines kommerziellen Promotionsberaters in Anspruch genommen. Dritte haben von mir keine geldwerten Leistungen für Arbeiten erhalten, die in Zusammenhang mit dem Inhalt der vorgelegten Dissertation stehen. Die Arbeit wurde bisher weder im Inland noch im Ausland in gleicher oder ähnlicher Form einer anderen Prüfungsbehörde vorgelegt und ist auch noch nicht veröffentlicht worden. Die Promotionsordnung der Fakultät Maschinenwesen der TU Dresden wird anerkannt.



.....

Junhee Han

Dresden, den 21.04.2014